THE ADSORPTION OF *BIDENS PILOSA* DYE MOLECULES ONTO TiO_2 NANOPARTICLE SURFACES FOR OPTIMIZATION OF LIGHT HARVESTING EFFICIENCY IN DYE SENSITIZED SOLAR CELL: AN EXPERIMENTAL AND THEORETICAL STUDY

BY

RANDELA RONEL RONELLA (18022836)

DISSERTATION SUBMITTED IN FULFILMENT FOR THE REQUIERENT OF THE MASTER (**MSc) OF SCIENCE DEGREE IN PHYSICS**

FACULTY OF SCIENCE, ENGINEERING AND AGRICULTURE

AT THE

UNIVERSITY OF VENDA

SUPERVISOR: DR N.E MALUTA (UNIVEN)

CO-SUPERVISOR: DR L.M MATHOMU (UNIVEN)

CO-SUPERVISOR: PROF R.R MAPHANGA (CSIR)

YEAR: 2023

DECLARATION

I, **Randela Ronel Ronella**, declare that this research report submitted to the University of Venda titled "**The Adsorption of *Bidens Pilosa* Dye Molecules onto TiO_2 Nanoparticles Surfaces for Optimization of Light Harvesting Efficiency in Dye sensitized solar cell: An Experimental and Theoretical study**" for the MSc degree in physics is my original work and has not been submitted for any degree at this or any other institution. This report does not contain other persons' writing unless specifically acknowledged and referenced accordingly.

Signed (student): _____ at University of Venda on Friday day of 8th 2023

DEDICATIONS

I would like to dedicate this dissertation to my family for their moral support throughout my studies. Above all, I would love to dedicate this to almighty God for His daily support and protection.

ACKNOWLEDGEMENTS

I would like to extend gratitude to my supervisor DR N.E Maluta and Co-Supervisors DR L.M Mathomu and Prof R.R Maphanga and fellow colleagues Mr T.M Mlotshwa and Mr T.S Ranwaha for helping me throughout this research. I would also want to extend my gratitude to the University of Venda's Department of Physics for the opportunity to proceed with my M.Sc. studies. Lastly, I would like to acknowledge the National Institute for Theoretical and Computational Sciences (NITheCS) for financial support.

ABSTRACT

The availability and high demand for electrical energy is a key global concern, as a result, Dye sensitized solar cells (DSSCs) have attracted a lot of attention in recent years due to their ease of preparation, low toxicity, and environmental friendliness. The current study describes the green synthesis of TiO_2 nanoparticles as well as their characterization using ultraviolet-visible, Fourier transformed infrared spectroscopy and X-ray diffraction. Furthermore, the study used Density Functional Theory to describe the optical characteristics of produced nanoparticles. The UV-Vis results showed that the dye extracted using solvents such as water, methanol, and ethanol had a common absorbance at 665 nm among the solvents used ethanol had the highest absorption. The molecules responsible for a broader range of absorbance are known to be pheophytin and porphyrin, which are found in chlorophyll extracted from the *B. pilosa* plant. FTIR analysis of the prepared TiO_2 revealed the absorbed functional groups of the synthesized *B. pilosa* extracts and confirmed the formation of TiO_2 NPs with a vibrational band at 497 cm^{1}. The TiO_2 NPs were heterogeneous in shape under TEM and SEM but spherical under SEM, indicating the formation of paste during agglomeration. XRD analysis confirmed that the polymorph formed is anatase with the highest peak of (101) surface, which was used to computationally adsorb the dye molecule. Pheophytin and porphyrin characteristics were optimized using DFT. For both experimentally and computationally, the UV-vis absorbance was found to be between 420 nm and 665 nm with a higher light harvesting efficiency. pheophytin and porphyrin exhibited energy gaps of 2.1 eV and 2.8 eV respectively. This study demonstrates that the dye molecule synthesized from *B. pilosa* is an efficient sensitizer for DSSCs. The adsorption results substantiate the spontaneous electron injection and subsequent efficient regeneration of oxidized dye molecules and the strong binding ability of porphyrin dye molecules to the TiO_2 surface. The results of this study will be useful for the development of highly efficient organic dyes for DSSCs.

Keywords: *B. pilosa*, Density Functional Theory, Dye Sensitized Solar Cells, Green Synthesis, Pheophytin, Porphyrin, Light Harvesting Efficiency.

LIST OF ABREVIATIONS

DSSC	=	Dye Synthesized Solar cell
PV	=	Photovoltaic cell
NPs	=	Nanoparticles
TiO_2	=	Titanium Dioxide
$LUMO$	=	Lowest Unoccupied Molecular Orbital
$HOMO$	=	Highest Occupied Molecular Orbital
LHE	=	Light Harvesting Efficiency
DFT	=	Density Function Theory
GGA	=	Generalized Gradient Approximation
$TDDFT$	=	Time Dependent Density Functional Theory
$IPCE$	=	Incident Photon to Convert Efficiency
$CASTEP$	=	Cambridge Serial Total Energy Package
ICT	=	Intermolecular Charge Transfer
LDA	=	Local Density Approximation
DOS	=	Density of States
CB	=	Conduction Band
CBE	=	Conduction Band Energy
Ef	=	Fermi Level
Eg	=	Energy gap
UV	=	Ultraviolet
VBE	=	Valence Band Energy
VAMP	=	Vulnerability Assessment Management Program

LIST OF FIGURES

LIST OF TABLES

Table of Contents

CHAPTER 1

1.1. Introduction

Electrical energy availability and distribution are major problems in both developed and developing countries. The world's energy demand is anticipated to rise continuously, resulting in a global energy crisis [1]. The existing energy supply in emerging countries mostly comes from fossil fuel sources such as coal, which is harmful to the environment and contributing to climate change due to the creation and emission of excessive carbon dioxide [2]. Climate change and the use of nonrenewable resources are seen as the most significant matters affecting humanity. Rising global temperatures are caused by the rapid depletion of fossil fuels and rising greenhouse gas emissions. The need for rapid access to clean and renewable energy supplies is long overdue. As a result, one of the possibilities for replacing the fossil fuel energy supply is to adopt renewable energy technologies.

South Africa (RSA) has one major electricity supplier, the Electricity Supplier Commission (Eskom). Almost 80% of Eskom's power is generated from coal, a non-renewable energy source that is depleting daily [2]. It is widely acknowledged that fossil fuels will be depleted in the near future and renewable energy technologies are being considered as an alternative solution to the energy crisis [2]. To mitigate energy supply challenges, Eskom has been forced to implement staggered energy use (load shedding). This has slowed economic progress in RSA and neighbouring nations that rely on Eskom's grid for energy [3].

A radical change should be put in place to use renewable energy thereby reducing the environmental pollution caused by use of fossil fuel. Renewable energy is energy obtained from natural resources that are replenished at a rate greater than their consumption. Sunshine and wind, for instance, are examples of supplies that are continually supplied. Renewable energy sources are abundant and ubiquitous [2]. There are many forms of renewable energy technologies; most of these depend on the sun in one way or another. And these energy technologies can be classified as solar energy, wind power, hydroelectric energy, and biomass [1, 2]. Renewable energy technologies offer a solution to the world's energy concerns since they are clean, non-polluting, and not harmful to humans or the environment.

Photovoltaic cells are used to harness solar energy and cover the conversion of light into electricity using photovoltaic semiconducting materials [4-7]. Photovoltaic installations can be ground-mounted or housetop-mounted. The mount is used as a sun tracker to follow the sun through the sky. Once installed, its operation produces no contamination or nursery gas outflows, it appears to have basic versatility in terms of management requirements, and silicon has extensive accessibility within the earth's exterior [4, 5]. However, photovoltaic technologies have a significant disadvantage in that their power generation works best under direct sunshine. There are four generations of photovoltaic systems: first, second, third, and fourth.

1.2. Generation of the photovoltaics

First-generation PV uses crystalline silicon. This is a leading and effective technology. Crystalline silicon modules have the most life cycle analysis studies [8]. First, photovoltaics is used because they have a standard Shockley-Queisser effectiveness of 14.0%, which is the maximum solar energy conversion efficiency for a material [9]. They are expensive because their fabrication or manufacturing process requires many steps. Thin-film solar cells are second-generation. CdTe, a second-generation PV technology, is one of the fastest-growing thin-film solar cells. The thin film device is subject to the same performance limits as the Shockley-Queisser efficiency limit. Thin film PV technology reduces manufacturing material and energy use, lowering device costs. CdTe holds 5.4% of the global market, up from 4.7% in 2008 [10].

Power conversion efficiency is 21% [8-10]. Third-generation PVs have no Shockley-Queisser limit and combine first- and second-generation benefits. Methyl ammonium lead halide perovskites form an organic-inorganic hybrid solar cell that is promising. Perovskite PV cells have advanced rapidly and become one of the most appealing PV research areas [9-10]. Another promising technology is dye sensitized solar cells [7]. As a result, there is a motivation to investigate or study DSSCs. The fourth generation of PV technology was introduced with the purpose of improving the optoelectronic properties of low-cost thin film PVs by combining the low cost and flexibility of polymer thin films with the stability of novel inorganic nanostructures. These device topologies keep the low cost of a solution processable PV structure while adding inorganic components to improve energy harvesting cross-sections, charge dissociations, and charge transport in PV cells [11].

1.3. Dye synthesized solar cells.

The dye sensitised solar cells (DSSCs) are devices that convert solar energy into electrical energy through light sensitization on a semiconductor with a low energy band [12,13]. DSSCs provide a long-term future for solar cells because they are environmentally friendly and have minimal production costs [12], they can be easily manufactured. Their affordable production costs have attracted a lot of interest in recent studies. They also include a counter electrode, an electrolyte comprising iodide and tri-iodide ions, and a nano-crystalline porous semiconductor electrode sensitized by a dye [14].

The dye acts as a sensitizer in DSSCs and is essential in the absorption and conversion of incident light rays into electricity [15]. Because of its ease of manufacture and mass-production screen-printing technology, DSSCs are inexpensive. Previously, ruthenium dye was used; however, dyes based on ruthenium complexes are expensive due to the scarcity of ruthenium metal and the chemical methods involved in their synthesis. The problem with ruthenium dye has prompted researchers to investigate organic metal-free dyes, which are primarily natural colors and are easily manufactured [13,16-20].

The first development of dye sensitized solar cells was the use of the ruthenium polypyridinic complex as a sensitizer to the wide-band crevice semiconductor, and it has since been the most proficient dye used [16-18]. The disadvantage of using ruthenium complex is that it is expensive and contains heavy metals that are detrimental to the environment [17-19]. Natural dyes can be found in fruits, leaves, and the entire plant, and they are low cost, non-toxic, and completely biodegradable. Natural dyes have a significant role in capturing sunlight and converting it into electrical energy [12, 15].

Some plants, fruits, flowers, and leaves have distinct colours and contain pigments that can be extracted and used as a sensitizer. Green plants contain a lot of chlorophyll, which helps absorb photons from the sun. Plants include a variety of colors, including chlorophyl, anthocyanin, betalain, and carotene. The anthocyanin pigment found in plants contributes to the color of natural products and plants (red, purple), and they retain light or photons with wavelengths ranging from 520 to 550 nm [20-23]. The natural dyes have the extra benefit of extending photon absorption into the near infrared portion of the spectrum.

In addition, the ideal DSSC sensitizer should absorb all light below a wavelength of 800 nm [23]. DSSCs can operate in low-light settings caused by cloudy skies and, in some cases, indirect sunlight. It has been proposed that DSSCs can also be used indoors, where they can work by absorbing photon energy emitted by various indoor lighting fixtures [24]. Another advantage is that DSSCs have higher efficiency at higher temperatures, which regular solar cells do not have. DSSCs can radiate internal heat to external environments far more efficiently than regular solar cells. Because they are often constructed with a thin layer of conductive plastic on the front layer, these DSSCs operate at lower internal temperatures [24].

However, the main disadvantage is that the liquid electrolyte used in DSSCs is temperature sensitive. That is at low temperatures, the electrolyte can freeze, rendering the solar cell useless. Because the liquid electrolyte swells at high temperatures, sealing of solar cells becomes a big issue. The use of a liquid electrolyte introduces other issues, such as possible instability and temperature limitations [24]. TiO_2 carries the electron photo-generated by light absorption and dye regeneration acts as a structure for the adsorbed dye molecule. since TiO_2 is less expensive and can be synthesised simply, numerous attempts have been taken to enhance its transportation of electrons to improve solar energy conversion in DSSC.

1.4. Working principle of DSSC

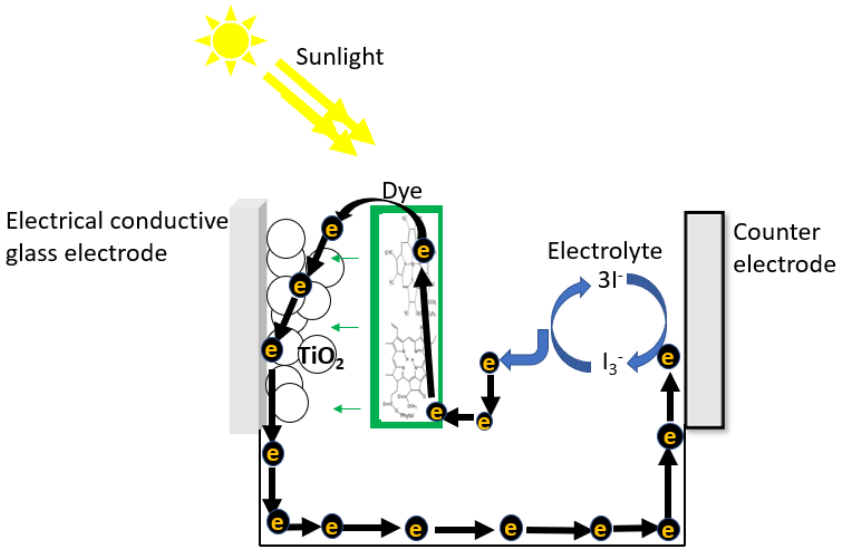

Figure 1. The working principle of dye synthesized solar cell [25].

Figure 1 illustrates the mechanism of light absorption and transport in DSSCs. The sunlight travels through the transparent electrode into the dye layer and is absorbed by the dye, which exits and injects electrons into the titanium dioxide. The electrons then travel towards the transparent electrode, where they are captured and used to power a load. After passing via the external circuit, the electrons are reintroduced into the cell via a metal electrode flowing into the electrolyte. The electrolyte then returns the electrons to the dye molecules, regenerating an electron flow and producing a current. However, because the dye molecules are small, a thick layer of dye molecules is required to capture a reasonable amount of the harnessed incoming light [26].

1.5. Natural dye

Natural dyes are growing more popular, and they are eco-friendly when used to construct DSSCs. These dyes are non-poisonous, can be disposed of efficiently in an easier way, are less expensive, and are more environmentally friendly than synthetic metal complex dyes [24]. As a result, natural dyes as light-harvesting elements in DSSCs can assist to more sustainable energy production in the future. Natural dyes are fully available in plants, can be extracted directly from plants with no pollution or lethal synthesis, and the separation and purification procedure are quite simple, thus they are being investigated as an alternative photosensitizer for DSSCs [24, 27-28]. This can be accomplished by using several forms of natural dye sensitization to absorb sunlight throughout all energy band ranges.

Natural pigments such as chlorophyll, anthocyanin, betalain, and carotene have been studied as photosensitizers for solar cell applications [15,24,27-30]. However, the main disadvantages of this form of solar cell are its low efficiencies and limited lifespan so far, with maximum efficiencies of about 1.5 – 2.09% and average efficiencies of about 0.4% [21,31]. Increased efficiency and stability would make natural pigment-sensitized solar cells an appealing alternative technology for portable or disposable electronic applications. One of the reasons for natural dyes' low efficiency is their low absorption coefficient and narrow absorption bands when compared to commonly used ruthenium-based dyes and cyanine or hemi-cyanine dyes [16,32-33]. Natural dye is important in absorbing sunlight and converting solar energy into electrical energy [24,27]. Some fruits, plants, flowers, and leaves, have a variety of colors and contain many pigments that can be used as sensitizers.

1.6. Chlorophyll as the main natural dye

Chlorophyll is a green pigment found in most green plants, as well as cyanobacteria and algae. Chlorophyll helps in the absorption of photons from sunlight; it can absorb light from red, blue, and violet wavelengths; it can also obtain its color by reflecting the green wavelength, resulting in the visible region having strong absorption peaks at 420 nm and 660 nm that can be used as a natural sensitizer in the visible light region [15,]. The most logical source of porphyrin that can be used as a sensitizer in DSSC is chlorophyll; it is also the greatest choice for DSSC modification [34]. These dyes are made by simply derivatizing natural chlorophyll molecules. Porphyrin or pheophytin molecules are two chlorophyll derivatives that are frequently used for this purpose [34-38].

1.6.1. Absorption of porphyrin

Porphyrin compounds are naturally occurring and defined by the porphyrin ring structures found in chlorophyll [36,37]. Porphyrin molecules are employed in various applications including chemical and biological sensors, as well as DSSC, semiconductors, and organic light-emitting diodes [24,36-37]. Porphyrin sensitizers have sparked considerable interest in solar cells because they are inexpensive, stable, easy to produce and modify, less poisonous [36,37] have rigid geometry, the ability to coordinate metals, and efficient electron transport [24,38]. They also have a high molar absorption coefficient [27,36] and a high light-harvesting ability. Porphyrins' chemical and physical mechanisms are responsible for electron transport, oxygen binding, photochemical reactions, and photosynthesis [38,39]. The porphyrin compounds' absorption peaks occur within the main emission spectrum of solar radiation, photons can be effectively captured and converted to various forms of energy such as heat and electricity. Porphyrin absorption spectra comprise two distinct bands: 380-500 nm (blue region) and 500-650 nm (red region). Porphyrin wavelength shifts and absorbance alterations are affected by solvent, pH, temperature, and central metal ions [18-19,36,40-41].

1.6.2. Absorption of pheophytin

A pheophytin is chlorophyll with no central magnesium ion. It plays a vital role in the conversion of light energy to chemical energy. The distinction between chlorophyll and pheophytin is that chlorophyll is a green pigment, but pheophytin is a chlorophyll without the core magnesium atom [35,42]. Unlike porphyrin, pheophytin absorbs in the visible and near-infrared regions. The absorption of pheophytin shifts to a longer wavelength, which

is the difference between the two molecules. The absorption spectra of pheophytin extends from 400 to 850 nm, with the highest absorption band at (666-669 nm) [35,42].

In the past decades, the first report on photosensitization of nano porous TiO_2 by chlorophyll derivatives was reported by Kay and Grätzel [7,12,18]. Over the years, considerable efforts have been put forward towards using chlorophylls as sensitizer in DSSCs. Many reports have shown that chlorophylls, which function as an effective photosensitizer in photosynthesis of green plants have the potential to be an environmentally friendly dye source [15,30,39,43]. Chlorophylls are metal complexes of magnesium ion, with high symmetry, consisting of a tetrapyrrolic macrocycle, encompass several pigments with common structural elements [35,43] The chlorophylls (Chl-**a** and Chl-**b**) are usually accompanied by their major derivatives, chlorophyllides (chlid **a** and chlid **b**) and pheophytins (Pheo **a** and Pheo **b**).

The carboxylic acid groups in the photosensitizer established an electronic coupling with the conduction band of TiO_2 which is helpful for anchoring the dye molecules and an effective electron injection to the conduction band of TiO_2. Thus, the carboxylic acid groups in the dye molecule are essential for dye-sensitized solar cell [35]. Chl-**a**, Chl-**b** and pheophytins are not strongly bound to the TiO_2 surface due to the weak interaction of the phytol ester group and keto carbonyl groups with the hydrophilic titania surface [36,37]. But Chlorophyll c1 (Chl-c1) and Chlorophyll c2 (Chl-c2) have the terminal carboxylic acid group, which is connected through a conjugated double bond of the porphyrin macrocycle. Hence, Chlc1 and Chl-c2 are strongly bound on the TiO_2 surface which ensures efficient electron injection into the TiO_2 conduction band and to prevent gradual leaching by the electrolyte [44,45].

1.7.3. *Bidens pilosa* contains chlorophyll. Porphyrin and pheophytin

B. pilosa is a plant that can be found in every country on the planet. It grows best in full sun and relatively dry soil [46]. Because *B. pilosa* is a plant that produces green chlorophyll pigmentation, it can be employed as a dye sensitizer. Figure 2 shows an image of the *B. pilosa* plant.

Figure 2. An aerial view of a green *B. pilosa* plant [46]

In DSSCs, natural pigment can be used as a dye sensitizer, the plant pigments are electronic structures with the ability to convert the energy that is transmitted or reflected by the plant tissue from the sun, this is called plant pigmentation, and each pigment is represented by the absorbed wavelength and color that can be seen by humans [27].

Natural pigments that can be used as dye sensitizers include carotenoids, flavonoids, chlorophyll, and anthocyanin that can be obtained from plants [28,30]. Chlorophyll is widely studied as a sensitizer in DSSCs, they absorb light in the visible region of the spectrum because they have a porphyrin that consists of a conjugated pyrroles system and is composed of substituents on the sides. Thus, chlorophyll contains a lot of non-bonding electrons and pairs of π-bonding electrons so that if radiated visible light, electrons in chlorophyll will be easily excited. Moreover, other properties such as HOMO-LUMO level energy with small bandgap energy, high molar absorption coefficient, good chemical and thermal stability make it a perfect sensitizer [19,34].

1.7. Titanium dioxide: An effective semiconductor

Titanium dioxide (TiO_2) is an effective semiconductor, a porous layer of titanium dioxide nanoparticles has a wide band gap which is suitable for useful energy. It is affordable, widely available, biocompatible, thermally stable, and nontoxic. In a DSSC, the particle size of TiO_2 anatase ranges 10–25 nm with a thin film thickness of 5–15μm [13,23]. TiO_2 exits in three forms: rutile, anatase and brookite. Although rutile is more stable, crystalline anatase is favored as it is chemically more active in DSSCs [13]. However, the delay of the dye sensitized solar cells design is the large band gap Of TiO_2, which is about 3.2 eV for Anatase 3.0 eV, for Rutile and 3.3 eV for Brookite which limits the practical applications in DSSCs because it only absorbs in the ultra-violet region of the solar spectrum [44,45]. This results in obtaining the low efficiency of these types of solar cells.

Substantially there is a need of improving the efficiency due to low-cost advantages of DSSCs and TiO_2 absorbs light in the ultraviolet region but can be photosensitized by the adsorption of organic and inorganic dye molecules to absorb the light in visible and near infrared regions.

1.9. Band gap of TiO_2

Band gap is the energy gap between the valence and the conduction band edges of the semiconductor. A band gap represents the minimum energy that is required to excite an electron up to a state in the conduction band where it can participate in conduction [28]. The measurement of the band gap of material is important in semiconductors, nanomaterials, and solar industries. The band gap is important as it determines the region of the solar spectrum that a solar cell absorbs [48,49]. The band gap of a material can be determined from its UV absorption spectrum [24].

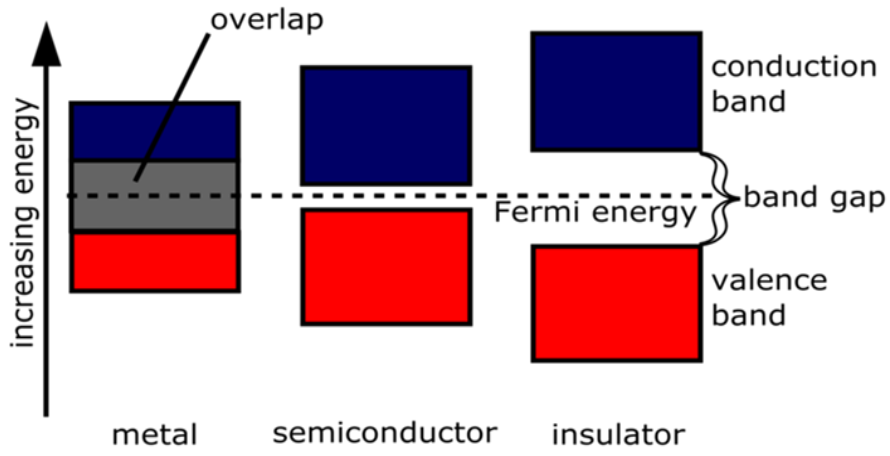

Figure 3. Band structure of different materials [48].

Figure 3 illustrates the difference in band gap size between insulators, conductors, and semiconductors. The magnitude of the band gap determines the properties of the materials. The electrons in the valence band are separated by a significantly bigger gap within the band gap of insulators; this means that there is a high, forbidden band gap energy preventing electrons from the valence band from leaping up into the conduction band and participating in conduction [48]. The valence band and the conduction band overlap between conductors. The overlap allows valence electrons to flow into the conduction band and participate in conduction; but, because it is not a complete overlap, only a fraction of the valence electrons will move through the material, which is insufficient to make conductors conductive [48-49].

However, the focus of this research is on semiconductors, which has a small enough gap to be bridged by solar excitation in the case of photovoltaic cells. The gap is essentially a size between a conductor and an insulator [50], a finite number of electrons can reach the conduction band and conduct modest amounts of electricity in this scenario [48]. Because of the electron-hole left behind, the excitation of the electron enables additional conduction processes to proceed. An electron from a nearby atom can occupy this area, causing a chain reaction of holes and electron movement that results in the creation of a current [48]. A modest amount of doping material can significantly boost this material's conductivity [48,49].

This study focused on the experimental and theoretical analyses of natural dyes extracted from *B. pilosa* leaves (blackjack) using three solvents: distilled water, methanol, and ethanol. Using a spectrophotometer, the extracts were generated using TiO_2 nanoparticles, and the solution was used to identify the wavelength of each solution with different solvents and where the solution of *B. pilosa* is more active. The adsorption of TiO_2 nanoparticle surfaces with dye molecules was studied using density functional theory (DFT) to optimize light harvesting efficiency, photo conversion efficiency, and photocurrent densities in DSSCs.

1.10. Aims and objectives.

1.10.1. Aims

- This work aimed to optimize the adsorption of the natural dye (*B. pilosa*) molecules on surface of TiO_2 nanoparticles.
- Experimentally the study aimed to extract natural *B. pilosa* leaves to synthesize TiO_2.

1.10.2 objectives based on the experimental and computational studies are:

1.10.2.1. Experimental studies

- To synthesize and characterise titanium dioxide using *B. pilosa* extracts.

1.10.2.2 Computational studies

- To determine the electronic and optical properties of the dyes adsorbed on TiO_2 nanoparticles surfaces.

1.11. Significance of the study

A genuine understanding of the interaction between natural dye molecules and TiO_2 surfaces is essential for DSSC enhancement. The use of natural dye and TiO_2 surfaces

will improve innovation in terms of environmentally friendly and low-cost materials and components. Investigation towards the interactions between the dye molecule and the TiO_2 surfaces, as well as the related electronic and optical properties, is important for improving the efficiency of dye sensitized solar cells and expanding their market availability.

1.12. Problem statements

The main limitation of TiO_2 is its wide band gap (E_g= 3.0 eV) which makes it absorb photons only on the ultraviolet region of the solar spectrum and this is a major problem in DSSCs. Since the wide band gap semiconductors are used in DSSCs, they limit the absorption of the photon in visible and near infrared regions and hence the experience of limited efficiency of these solar cells. This leads to the limitation of the practical applications in DSSCs because it only absorbs ultra-violet regions of the solar spectrum. Hence there is a need to extend the absorption spectra to the near infrared region [13], which will lead to improvement of the efficiency of DSSCs [13,23-24].

1.13. Hypothesis

The use of *B. pilosa* dye molecules could improve the photon absorption from visible to near infrared, improve the injection of electron to the TiO_2 nanoparticle and could also improve the efficiency of the solar cells.

CHAPTER 2

2. Literature review

2.1. Extraction of natural dyes

Natural dye extraction from plants containing pigments such as chlorophyll, anthocyanin, betalain and beta-carotene has been effectively used to manufacture DSSC. When compared to dyes such as anthocyanin and beta-carotene, chlorophyll's dye nature has the highest level of efficiency. The low cost of production and environmental friendliness of DSSC, and specifically Natural Dye Sensitized Solar Cell (NDSSC), are the key driving forces for interest. Currently DSSC has the capacity to transform solar photons into electrical energy using clean energy through natural dyes which is one of the techniques used to increase the stability of energy usage [52].

The natural dyes have demonstrated wide-ranging solar spectral absorption in the visible region (400-700 nm) [52]. Yuanzuo Li *et al* investigate three natural dyes which were extracted and studied as potential sensitizers for dye sensitized solar cells (Forsythia suspensa, Herba Violae, and Corn leaf). The UV-vis absorption spectra revealed that three natural dyes were primarily composed of the molecule pheophytin a. The absorption spectra of three dyes were discovered to encompass the two absorption bands from 400 nm to 700 nm, with the greatest absorption band (666-669 nm) corresponding to the red absorption band (666nm) of pheophytin a. [42,52-53]

In 2014, Vinoth S *et al.* reported their work on natural dyes derived from three types of grasses; Hierochloe Odorata (HO), Torulinium Odoratum (TO), and Dactyloctenium Aegyptium (DA) were utilised as light harvesters DSSCs using a simple extraction technique for the extraction of the dye from the grasses. Among the three grasses, the DSSC constructed with the dye derived from Hierochloe Odorata (HO) had the highest conversion efficiency, around 0.46%, while the cells made with TO and DA dyes had conversion efficiencies of 0.32% and 0.24%, respectively. All three dyes revealed two strong absorption peaks in the range of 400 nm and 600 nm, as well as two extremely tiny bands at around 540 nm and 606 nm [42].

The FT-IR spectra of natural dyes extracted from HO, TO, and DA revealed the majority of the chlorophyll derivatives' distinctive peaks [42,54]. Chlorophylls and derivatives contain distinct infrared bands that correspond to the C=O, C=C, C-H, and N-H groups. All three extracted dye, the distinctive C=O corresponded to the ketone in the

cyclopentanone ring of pheophytin, which was detected at 1725 cm $^{-1}$. Similarly, the C=C vibrations of pheophytin were detected at around 1618 cm $^{-1}$.

In 2015, Syafinar R *et al.* investigated chlorophyll pigments as a natural-based dye for dye-sensitized solar cells, extracting chlorophyll from spinach using ethanol and distilled water for use as a sensitizer in DSSC. The influence of solvents was examined by evaluating the dyes' absorption spectrum and band gap. According to the UV-Vis absorption spectrum, chlorophyll extracted with distilled water has a wider portion of the visible light spectrum in the range of 400 to 720 nm than chlorophyll extracted with ethanol, which runs from 450 to 700. The lowest dye band gap was also presented by the extracted chlorophyll with distilled water at 1.83 eV, and the band gap of dye was also presented by the extracted chlorophyll with ethanol at 1.88 eV. [15]

2.2. **Enhancing the stability and efficiency of natural dye**

To enhance the performance of the DSSC in the visible and near-infrared region, light/photons absorption from organic dyes must achieve their maximum values. Several studies on natural dyes have been conducted. It has been established that chlorophyll is the most prominent natural pigment capable of absorbing photons in both visible and near-infrared regions of the solar spectrum. Using chlorophyll-based natural dyes, Zainal A *et al.* developed a method to improve the stability and performance of DSCCs by Changing the crude chlorophyll to chlorophyll central group enhancing the stability of natural pigments.

The crude chlorophyll isolated from the papaya leaf extract was first transformed to Mg-chlorophyll and subsequently to Fe-chlorophyll. Using papaya leaves, crude chlorophyll, Mg-chlorophyll, and Fe-chlorophyll were successfully synthesized. Before being utilized as a dye in DSSC solar cells, the compounds were subjected to a UV-Vis absorbance test [55]. The results of the UV-Vis test demonstrated a wavelength shift from crude chlorophyll to Mg-chlorophyll and from Mg-chlorophyll to Fe-chlorophyll. They also discovered that the N719 dye sensitizer was able to obtain a solar cell DSSC efficiency as high as 0.87%. In comparison to papaya extract dyes, the central atom of the chlorophyll in Mg^{2+} was modified to $Fe^{2+,}$ which increased effectiveness by more than 2.5 and stability

by two times. In addition, when compared to other natural dyes, DSSC with Fe-chlorophyll dye produced the maximum efficiency [55].

In 2016 Cerda B *et al.* investigated natural dyes as sensitizers to improve the efficiency of dye sensitized solar cells. Their main goal was to create a photo electrode with different dyes to improve the efficiency of these solar cells [56]. Fresh maqui, black myrtle, spinach, and a dye mixture of spinach and spinach-maqui-myrtle were used to manufacture the dyes. The dyes were extracted using maceration (soaking) for one day in a methanol solvent. They discovered that maqui absorbs well at 546nm. Black myrtle absorbs similarly to maqui, with good absorption at 542 nm. At 433 nm and 437 nm, maqui, spinach-maqui, and black myrtle have the same absorption. They concluded that spinach-black myrtle absorbs well in the 400-650 nm range [56].

In 2017 Ramanarayanan R *et al.* reported their work on natural dyes derived from red amaranth leaves as light-harvesting pigments for dye-sensitized solar cells. Red amaranth was identified as a source of two natural dyes that could be used as low-cost sensitizers for broad band gap semiconductors in dye sensitized solar cells [57]. The two colors were identified as Chlorophyll and Betalain based on their absorption spectra. In their work, they studied the photo electrochemical properties of dye sensitized solar cells using natural pigments containing Chlorophyll and Betalain. According to their findings, the Chlorophyll dye has an energy conversion efficiency of 0.53%. The energy conversion efficiency of the Betalain dye was 0.23% [57].

2.3. Adsorption of dye onto TiO_2

The dye adsorption process is regarded as a crucial phase that must be executed with attention to obtain high cell efficiencies. This is because the amount of dye adsorbed by TiO_2 determines the incident photon-to-current efficiency (IPCE) and the related current density of the cells. Adsorption works by capturing incident atoms or molecules on the surface. Adsorbent is the substance onto which adsorption occurs [58].

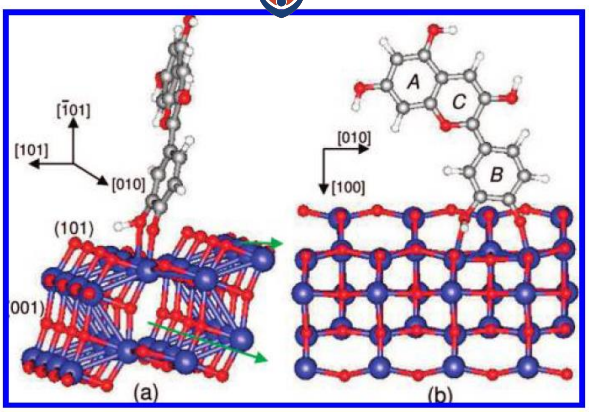

Figure 4. Unit cell for a TiO_2 nanowire sensitized by the cyanidin dye: (a) side view; (b) top view [59]

Meng S *et al*. published their findings on natural dyes absorbed in TiO_2 to improve light absorption and ultrafast electron injection. As illustrated in Figure 4, they investigated the electronic coupling and charge injection processes in natural dye sensitized TiO_2 nanowire solar cells using cyanidin as a model molecule. When comparing traditional DSSCs, they investigated the dye adsorption with TiO_2 nanowire, demonstrating that deprotonation of the dye causes the HOMO to be inside the bandgap and the LUMO to be remarkably close to the TiO_2 CBM. The oxygen vacancy enhanced the dye adsorption and considerably increased visible light absorption. This was due to the dye molecules' existence [59]. Furthermore, real-time TDDFT simulations demonstrated that the excited electrons were injected into the TiO_2 conduction band at a time scale of 50 *fs,* and this should be beneficial to improving the transportation of electrons from valence band to conduction band and improving the absorption of the dye molecule on DSSCs [59].

In 2017 Mang Niu *et al.* used density functional theory to investigate the structural and electrical properties of dye-sensitized solar cells (DSSCs) constructed of I-doped anatase TiO_2(101) surface sensitized with NKX-2554 dye. The calculated results suggested that the cyanoacrylic acid anchoring group of NKX-2554 has a high affinity for the TiO_2(101) surface. Dissociative and bidentate bridging was shown to be the most favorable adsorption arrangement. In contrast, I-dopant integration can reduce the band gap of a TiO_2 photoanode and improve the NKX-2554 dye, which can improve anatase TiO_2's visible-light absorption and facilitate electron injection from the dye molecule to the TiO_2 substrate. As a result, I-doping has the potential to significantly enhance DSSC incident photon-to-current conversion efficiency (IPCE) [60].

2.4. Enhancement of Dye Adsorption on TiO_2 Surface for Dye-sensitized Solar Cells

To improve the power conversion efficiency of a dye-sensitized solar cell (DSSC), the surface of the TiO_2 photoelectrode should be modified using techniques such as doping or adsorption of the dye molecule. Jang I *et al*. reported their work on hydroxyl group which was chemically adsorbed on the surface of TiO_2 film using a surface modification procedure including NH_4OH (Ammonium Hydroxide) solution, due to the stronger chemical interactions between the increased number of hydroxyl groups and the carboxyl anchoring groups [61]. They discovered that the dye increased as the number of hydroxyl groups were added, a greater amount of N719 dye was attached to the TiO_2 surface. The amount of dye adsorbed on hydroxylated TiO_2 electrode increased the efficiency by up to 32.61 %, resulting in increasing the power conversion efficiency of DSSCs and this indicated that when a dye molecule is adsorbed onto TiO_2 the absorption and efficiency increases in a DSSCs [61].

2.5. Effects of solvents adsorption of dye in DSSCs

To gain insight into understanding the effect of the solvents on the adsorption geometries and electronic properties of dye sensitized TiO_2 interfaces. Mosconi E *et al*. performed first-principles calculations on organic dyes molecules and co-adsorbed them on the (101) surface of anatase TiO_2 using solvents (water and acetonitrile) [62], they discovered that the adsorbed solvent caused the dye to deprotonate because of the system's changing acid/base characteristics. In the presence of co-adsorbed solvent molecules, analysis of the electronic structure for the dye sensitized TiO_2 structures revealed an increase in the TiO_2 conduction band from 0.2 to 0.5 eV (0.5 to 0.8 eV) in water, and for acetonitrile the increase of 0.6 to 1.0 eV was observed. As a result, the dyes' presence modified the increase of the TiO_2 conduction band. Thus, the presence of acetonitrile solvent contributed to increasing the TiO_2 CB, which should enhance the efficiency of the DSSCs in terms of open circuit voltage [62].

Adedokun O *et al*. investigated the effect of several solvents for natural dye extraction and adequate sensitization of the same extracted dye on mesoporous TiO_2 for dye sensitized solar Cell applications. They extractracted natural dyes from Punica granatum (pomegranate) peels, Citrus reticulata (tangerine) peels, and Parquetina nigrescens

(African parquentina) leaf, different extraction solvents, including distilled water, ethanol, acetone, methanol, acetonitrile, dimethyl sulfoxide (DMSO), chloroform, n-hexane, ethyl acetate were used [63].

The non-polar solvents performed less in the extraction of betacyanin dye from Punica granatum peels than the polar solvents, such as distilled water, methanol, and ethanol. The broader range of absorbance between 350 nm and 600 nm was demonstrated by all the extracts [63]. However, for polar solvents including water, ethanol, and methanol, the absorbance spectra of P. granatum extracts displayed a large peak at about 500 nm - 560 nm, which is caused by the presence of red violet betacyanines dye, and this is because betalains have significant absorption in the 400 nm – 600 nm region. Thus, the effects of solvents play a vital role in enhancing the absorbance and efficiency of a dye in a DSSCS [63].

In 2018 Jin X *et al*. worked on the development of three porphyrin dyes with various acceptors, including carboxylic acid, cyanoacrylic acid, and 2-cyano-N-hydroxyacrylamide, using Density Functional Theory and Time-Dependent Density Functional Theory [64]. When compared to the best sensitizer (YD2-o-C8) thus far, these dyes have small highest occupied orbital to lowest unoccupied orbital (HOMO-LUMO) band gaps and large absorptions with great oscillator strength at porphyrin Q bands. Furthermore, in terms of electronic coupling with TiO_2, the designed Dye1 was comparable to YD2-o-C8, whereas improved Dye2 and Dye3 were superior to YD2-o-C8, implying that Dye2 and Dye3 will be much faster for electron injection in dye-sensitized solar cell systems due to their long-term stable and efficient anchor groups. All these properties show that their dyes, notably Dye2 and Dye3, have increased absorption performance and faster electron injection. Furthermore, their findings suggested that 2-cyano-N-hydroxyacrylamide could be a promising acceptor [64].

In 2020 Ananthi *et. al.* reported two efficient dye-sensitized solar cells (DSSCs) which were prepared using natural dyes extracted from Acalypha Godseffia and Epipremnum Aureum plant leaves. In their work, they reported the use of two natural dyes for developing dye sensitized solar cells. The two dyes are eco-friendly and have proven to be efficient ones. The electrical characteristics of the DSSCs using these dyes as sensitizers reveal that they could be the further possibility of enhancing currently recorded efficiencies [63]. Among these two, the dye extracted from *Acalypha Godseffia* appears to

have superior power conversion efficiency 4.372% than the dye extracted from *Epipremnum Aureum* that resulted in the efficiency of 3.362%. Hence, these two dyes show the potential scope for further development of efficient DSSCs [65].

In 2021 Rahmatika R *et al* reported on theoretical studies of pheophytin compound modified with Cu, Ni, and Zn atoms as a sensitizer for dye solar cell compound the study aimed to determine the parameters of bond length, spectra, molecular density, HOMO-LUMO energy, LHE, and ΔG injection of pheophytin α and β complexes using the central atoms of Cu, Ni, and Zn, and formulate the effect of adding central atoms of Cu, Ni and Zn on the characteristics α and β pheophytin photoelectric and determined the best modification capable of producing the best characteristics for pheophytin as a dye compound on the DSSC based on parameters of bond length, spectra, molecular density, energy HOMO-LUMO, LHE, and ΔG injection [66].

Based on the parameters used when viewed from the length of the central atomic bond with the best ligand are Ni Pheophytin α; the best HOMO-LUMO energy was obtained by Pheophytin α with a LUMO energy value of -2.6349 eV and HOMO energy value of -4.7282 eV. The best spectra were obtained by Zn Pheophytin β with absorption at wavelengths of 386.77 nm and 536.15 nm; the best light absorption efficiency (LHE) was from Zn Pheophytin β; Based on the above parameters the best modification for DSSC was observed to be Zn Pheophytin β> Zn Pheophytin α> Pheophytin β>Pheophytin α> Cu Pheophytin β> Ni Pheophytin α> Ni Pheophytin β> Cu Pheophytin α. The theoretical modification used is DFT/B3LYP, the accuracy of the method used amounted to 89.27% and 96.09% of LHE [66].

In 2021 Yadav V *et al.* reported their work on fabrication of eco-friendly, low-cost dye sensitized solar cells using harda fruit-based natural dye using a using a facile and low-cost aqueous extraction technique and synthesis. The harda fruit-based natural dye and direct dye (fabric dye) were investigated for application in the DSSCs. The dye and a fabric dye were characterised to test their potential for the DSSC applications. The structure modification and interaction of dye molecule with TiO_2 was confirmed by the Raman, FTIR, and absorption spectroscopy studies. XRD revealed that the crystalline quality of TiO_2 is better in natural dyes as compared to the direct dyes. FESEM analysis showed that the natural\TiO_2/dye structure has a larger grain size [67].

The DSSCs based on the natural dye and fabric dye were successfully demonstrated with

3.52% and 0.80% efficiency, respectively. Therefore, natural dye based DSSC yielded the best photovoltaic performance with a power conversion efficiency of 3.52%. These findings can be helpful in the development of emerging cost-effective environmentally sustainable natural dye based DSSCs [67].

In this work, chlorophyll was extracted from *B. pilosa* leaves, the extracts were used to synthesize TiO_2 nanoparticles solution. The solutions were used to determine the wavelength of each with different solvents (distilled water, methanol, ethanol) and determined where the solution will be more active using a spectrophotometer. Furthermore, DFT was used to calculate DSSC light harvesting efficiency, photo conversion, and photocurrent densities by studying the dye adsorption on TiO_2 nanoparticle surfaces.

CHAPTER 3

3. Experimental method

3.1. Materials

Titanium (IV) oxide, ethanol, methanol, distilled water, *Bidens pilosa* leaves, hotplate stirrer, stirrer bar, thermometer, 0.22µm syringe filter, sieve, mortar, pestle, household blender, thermometer, Erlenmeyer flask, 250 ml beaker, 100 ml Measuring cylinder were used.

3.2. Preparation of *B. pilosa* plant extracts

The plant was collected from the University of Venda at the site of agriculture field, the plant was cleaned using distilled water several times and was left to dry in the laboratory on top of the bench for five days under room temperature until all the moisture contents of the roots were removed. The dried leaves were grinded into fine powder using pestle, mortar, household blender and a small sieve. The extraction process was performed by mixing 5g of powder of leaves with 50mL methanol into 50mL conical tubes, similarly, was

done for distilled water and ethanol [68,69]. The mixtures were placed in a rotary machine for 24 hours. After 24hrs the centrifugation process was performed to separate the liquids from the solid liquid mixture at a speed of 5000 rpm for 15 minutes, finally the solid residues were filtered using a 0.22µm syringe filter to acquire a pure natural dye solution, the extracts were characterised using a UV-Vis spectrophotometer.

3.3. Preparation of TiO_2 nanoparticles

TiO_2 NPs was prepared by dissolving 5 mM of titanium (iv) oxide into 225 ml of distilled water and was under magnetic stirring for 4 hours, 25 ml of extracts was slowly added and placed on a shaking incubator machine for 24 hours under room temperature. The color of the resulting solutions changed from milky white to green after adding the extracts, then changed from green to brown after 24 hours. The color change is mainly due to the reduction of the metal ions (Ti^{4+}) which indicates the formation of TiO_2 NPs [69-71]. The watch glasses were used to dry the solutions in an Ecotherm oven at a temperature of 180^{o}C. The synthesized nanoparticles were characterized using a spectrophotometer and the dried samples were characterized using SEM, TEM, EDS, FTIR and XRD

3.3.1. Characterisations

UV-visible absorption spectra of *Bidens pilosa* were measured to determine the maximum wavelength of absorption. The absorption spectra of the extracts obtained from *B. pilosa* leaves were recorded using a UV–Vis spectrophotometer Spectra Max M3 spectroscopy. Similarly, was done for synthesized TiO_2 nanoparticles using *B. Pilosa*. UV-Vis spectrophotometers employ a light source to illuminate a sample with light ranging from UV to visible wavelengths. The sensors then measure how much light the sample absorbs, transmits, or reflects at each wavelength [72].

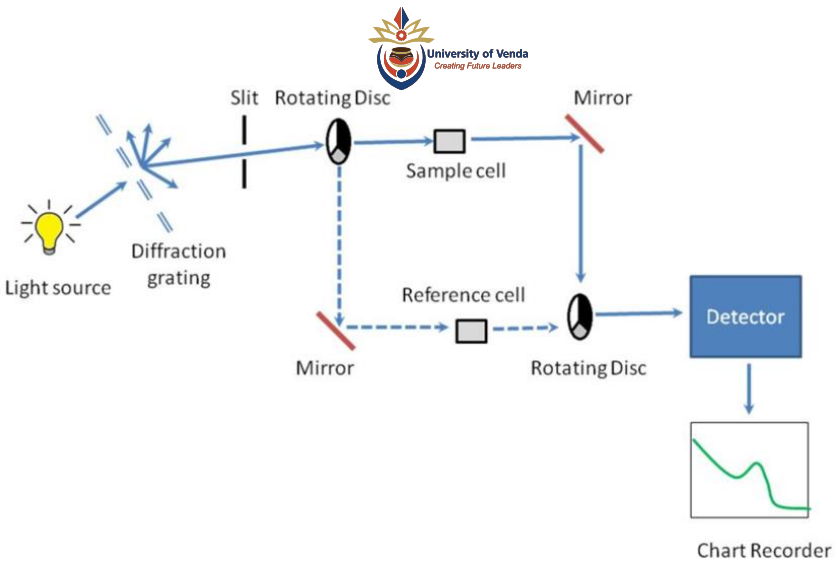

Figure 5 schematic diagram of UV-Vis [72]

3.3.2. Fourier transform infrared spectroscopy (FTIR).

Fourier transforms infrared spectroscopy (FTIR): FTIR is a good analytical tool to illustrate the binding properties of synthesized nanoparticles. FTIR analysis of *B. pilosa* synthesized TiO_2 nanoparticles was performed. The FTIR analysis was taken on ALPHA.P FTIR (Bruker) spectrometer powdered. Before analyzing the samples, the background was run first to obtain the spectrum trail with a 4 cm^{-1} resolution and using a minimum of 24 scans. The spectra were recorded within the wavelength range of 400 to 4000 cm^{-1} and operated in transmittance mode. Infrared light from the light source travels along the optical path through a Michelson interferometer in FTIR analysis. The phase difference varies over time because of the moving mirror's reciprocating movements altering the optical path difference with the fixed mirror. In the Michelson interferometer, the light beams are recombined to create interference light. An interferogram is used to record the interference light's intensity, with the horizontal axis representing the optical path difference [73].

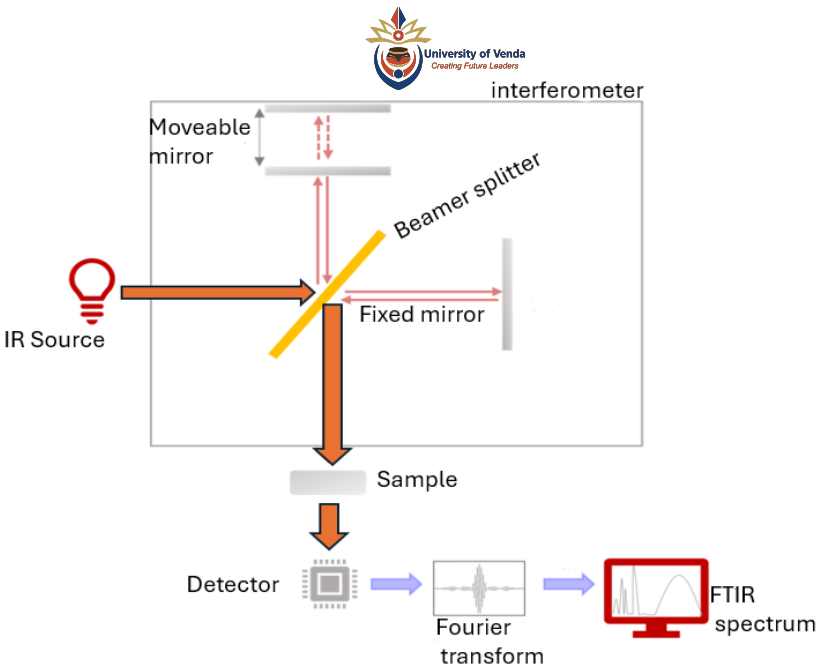

Figure 6 Schematic diagram of FTIR [73]

3.3.3. Transmission electron microscopy (TEM)

Morphology, particle size distribution and crystallinity were conducted. The samples were dissolved in 5 µL of ethanol, then sonicated and each solution was deposited on the carbon coated copper grid. A JEOL JEM-2100 electron microscope operated at an accelerating voltage of 200 kV recorded the TEM images. TEM provides information on elements and compounds structures [74].

3.3.4. Scanning electron microscopy (SEM)

Scanning electron microscopy (SEM): The scanning electron microscopy is an analytical technique which is used to determine the morphology and the size of plant synthesized nanoparticles. SEM and EDX were used to analyze the morphology and composition of the synthesized nanomaterials, respectively. A JEOL- JSM 7500F Scanning Electron Microscope instrument equipped with a field emission gun was used to analyze morphology. SEM gives a detailed 3D and topographical image and the versatile information garnered from different detectors [74].

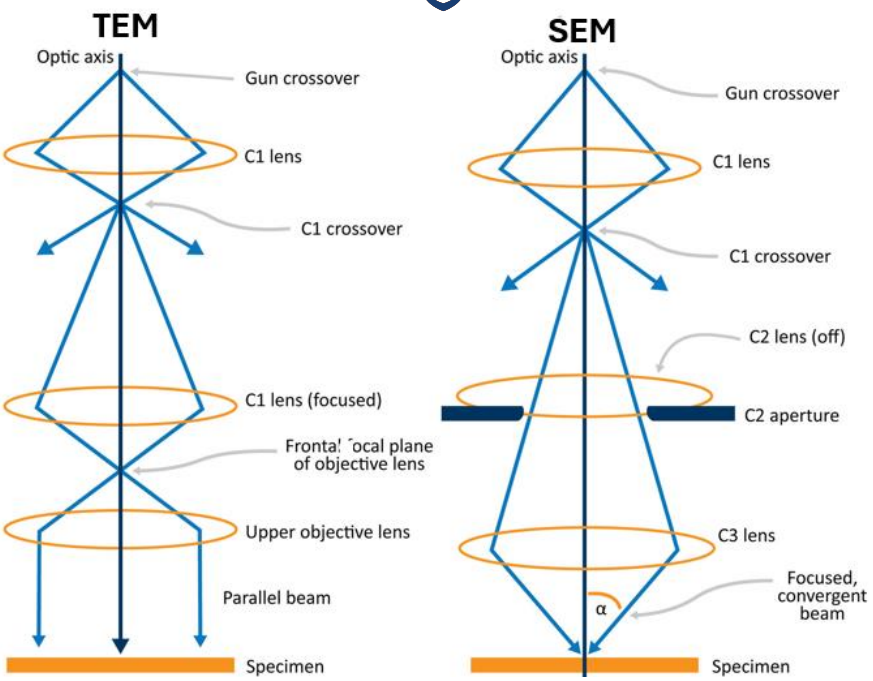

Figure 7 schematic diagram of TEM and SEM [74]

3.3.5. X-Ray Diffraction

The phase information and crystallinity of synthesized nanoparticles was determined by X-ray diffraction study. X-ray diffraction of synthesized nanoparticles was taken using X-ray diffractometer (PANalyticalX'Pert PRO, Netherlands). The operating parameters used were Cu Kα radiation source as X-ray (ƛ=1.5405 Å) at room temperature. The voltage was 40 kV and current were 50 mA respectively. XRD finds the geometry or shape of a molecule using X-rays. XRD techniques are based on the elastic scattering of X-rays from structures that have long range order [75].

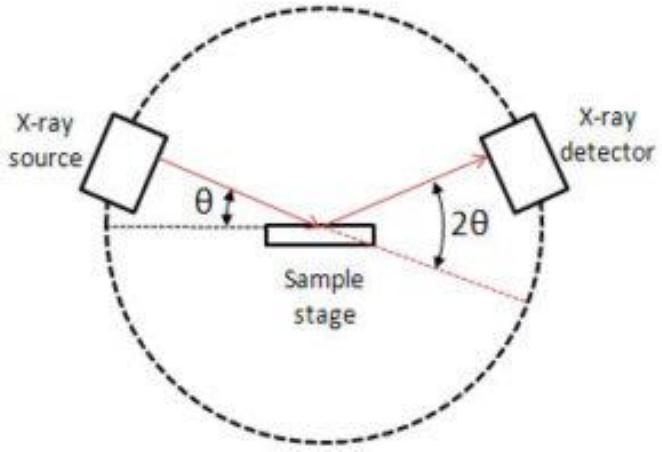

Figure 8 Schematic diagram of XRD [75]

3.4. THEORETICAL METHOD

3.4.1. Theoretical methodology

The plane wave pseudopotential technique is used to solve a set of one-electron Schrodinger (Kohn-Sham) equations [76,77]. In a plane wave basis set defined by periodic boundary conditions and Bloch's theorem, the wave functions are enlarged. Ab-initio pseudopotentials are used to define the electron-ion potential in both norm-conserving and ultra-soft formulations. The structural computations and analysis of the structures were performed using the Cambridge Serial Total Energy Package (CASTEP), which uses density functional theory with a plane wave basis set. Total energies, electronic structure, geometry, molecular dynamics, transition states, phonons, electric field response, exchange correlation, and other physical properties of materials can be calculated using CASTEP [78].

3.4.2. Density functional theory

Density functional theory (DFT) is a computational quantum mechanical modeling tool used in physics, chemistry, and material science to analyse the electronic structure of many body system atoms, molecules, and the condensed phase.

The features of a many-electron system can be derived using this theory by employing functionals, which are functions of another function, in this case the spatially dependent electron density; thus, the name density functional theory comes from the usage of functionals of the electron. The original density functional theory has been generalised to deal with a wide range of situations, including spin polarized systems, multicomponent systems like nuclei and electron hole droplets, free energy at finite temperatures, superconductors with electronic pairing mechanics, relativistic electrons, time-dependent phenomena and excited states, bosons, and so on [79].

3.4.3. First principle calculations

In quantum physics, a wave function describes the quantum state of a group of particles in an isolated system. Solving the Schrödinger equation [80] yields the ground state for a set of atoms.

$$H\Psi = E\Psi \quad \text{..} \quad (1)$$

The Born-Oppenheimer approximation is utilised, which suggests that the dynamics of atomic nuclei and electrons can be separated.

$$m_{nuclei} \gg m_e \quad \text{..... (2)}$$

where m_{nuclei} denotes the mass of the nuclei and m_e denotes the mass of the electron. The nuclei are heavy and slow, but the electron is light and quick. Nuclear and electron dynamics are decoupled into two wave functions.

$$\Psi\{(r_i),(R_I)\} = \Psi_N\{R_I\} * \Psi_e\{r_i\} \quad \text{..... (3)}$$

For many particle problems in solid state, the Schrödinger equation is solved for electrons in the form.

$$H\Psi(r_1, r_2, r_3, \ldots, r_N) = E\Psi(r_1, r_2, r_3, \ldots, r_N) \quad \text{..... (4)}$$

The electron Hamiltonian consists of three important terms which include electrons.

$$H = -\frac{\hbar^2}{2m_e}\sum_i^{N_e} {\nabla_i}^2 + \sum_i^{N_e} V_{ext}(r_i) + \sum_{i=1}^{N_e}\sum_{j>1} U(r_i, r_j) \quad \text{..... (5)}$$

where the first term of equation 5 represents the kinetic energy term, the second term is the potential energy term indicating the electrons interacting with the nuclei and the third term is the electron-electron repulsion term. V_{ext} is the external potential. The term functional means a function of a function, i.e., operation on a function gives another function [78].

$$F[f] = \int_{-1}^{1} f(x)dx \quad \text{..... (6)}$$

Equation (6) is an example of a functional. For the density functional theory, it is possible to move from the wave functions to electron density.

The electron density is defined in the form,

$$n(r) = \Psi^*(r_1, r_2, r_3, \ldots, r_N)\Psi(r_1, r_2, r_3, \ldots, r_N) \quad \text{..... (7)}$$

Electron density is only 3 dimensional. One of the electrons is treated as a point charge in the field of all the other electrons, which simplifies the many-electron problem to many one electron problems.

$$\Psi(r_1, r_2, r_3, \ldots, r_N) = \Psi(r_1) * \Psi(r_2) * \Psi(r_3) * \ldots * \Psi(r_N) \quad \text{..... (8)}$$

Equation (8) is known as the Hartree product.

Now the electron density is defined in terms of the individual electron wave functions.

$$n(r) = 2\sum_i \Psi_i^*(r)\Psi_i(r) \quad (9)$$

3.4.4. Hohenberg and Kohn theorems

The theorems provide the foundation of the Kohn-Sham density functional theory. The core proposition of density functional theory is that the ground and excited state properties of a many-electron system in the presence of an external field can all be known exactly from the ground state density. There are two essential theorems [80].

Theorem 1

[71] gives the ground state energy E as a unique functional of the electron density.

$$E = E[n(r)] \quad (10)$$

Thus, all that is required to define the total ground state energy is the electron density.

Theorem 2: The real ground state electron density is the electron density that minimizes the energy of the overall functional. This theorem teaches how to calculate ground state energy.

$$E[n(r)] > E_0[n_0(r)] \quad (11)$$

The energy functional consist of two main parts, the known and the unknown energy.

$$E[\{\Psi_i\}] = E_{known}[\{\Psi_i\}] + E_{XC}[\{\Psi_i\}] \quad (12)$$

The known energy term is given by:

$$E_{known}[\{\Psi_i\}] = -\frac{\hbar}{m_e}\sum_i \int \Psi_i^* \nabla^2 \Psi_i d^3r + \int V(r)n(r)d^3r + \frac{e^2}{2}\int\int \frac{n(r)n(r')}{r-r'} d^3r d^3r' + E_{ion} \quad (13)$$

The unknown energy term $E_{XC}[\{\Psi_i\}]$ is known as the exchange-correlation functional and it takes care of all the quantum mechanical interactions between electrons. It includes all quantum mechanical terms, and it is not known because it needs to be approximated.

3.4.5. Exchange correlation functionals

Several functionals are utilized depending on the area of interest in the calculated results; some are used because they are better in reproducing one property than another. Local density approximation (LDA) and generalized gradient approximation (GGA) functionals

are commonly utilized. The local density approximation is based on the local electron density and is only affected by one variable (the density). The gradient of the electron density is considered in generalized gradient approximation, which necessitates knowledge of two variables (the density and its gradient). Other functionals include the local PBE, PW91, and WC of GGA. There are also Ab initio non-local HF, empirical non-local B3LYP, and DFT+U.

3.4.6. The Kohn-Sham scheme

Kohn and Sham introduced a method based on the Hohenberg-Kohn theorem that enables one to minimize the functional $E[n(r)]$ by varying $n(r)$ over all densities containing N electron [76]. This constraint is introduced by the Lagrange multiplier μ chosen so that $\int n(r)dr = N$.

$$\frac{\delta}{\delta n(r)}[E[n(r)] - \mu \int n(r)dr] = 0 \quad \text{..... (14)}$$

$$\Rightarrow \mu = \frac{\delta E[n(r)]}{\delta n(r)} \quad \text{..... (15)}$$

Kohn and Sham chose to separate $F[n(r)]$ into three parts, so that $E[n(r)]$ becomes:

$$E[n(r)] = T_s[n(r)] + \frac{1}{2}\int\int \frac{n(r)n(r')}{|r-r'|}drdr' + E_{XC}[n(r)] + \int n(r)V_{ext}(r)dr \quad \text{..... (16)}$$

where $T_s[n(r)]$ is defined as the kinetic energy of a non-interacting electron gas with density $n(r)$ and is given by,

$$T_s[n(r)] = -\frac{1}{2}\sum_{i=1}^{N}\int \Psi_i^*(r)\nabla^2\Psi_i(r)dr \quad \text{..... (17)}$$

Equation (16) also acts as a definition for the exchange correlation energy functional $E_{XC}[n(r)]$. We can rewrite equation (15) in terms of an effective potential $V_{eff}(r)$ as follows.

$$\frac{\delta T_s[n(r)]}{\delta n(r)} + V_{eff}(r) = \mu \quad \text{..... (18)}$$

Where; $$V_{eff}(r) = V_{ext}(r) + \int \frac{n(r')}{|r-r'|}dr' + \frac{\delta E_{XC}[n(r)]}{\delta n(r)} \quad \text{..... (19)}$$

Now, if one considers a system that contained non-interacting electrons moving in an external potential equal to $V_{eff}(r)$ as defined by equation (17), then the same analysis would lead to the same equation. Therefore, to find the ground state energy and density, E_0 and $n_0(r)$ all one must do is to solve the one electron equations,

$$\left(-\frac{1}{2}\nabla_i{}^2 + V_{eff}(r) - E_i\right)\Psi_i(r) = 0 \quad \text{..... (20)}$$

As the electron density is constructed per the equation

$$n(r) = \sum_{i=1}^{N}|\Psi_i(r)|^2 \quad \text{..... (21)}$$

These equations must be solved with self-consistently scheme [76], which is discussed in the next subsection.

3.4.7. Self-consistency scheme

This scheme determines the electron density, it consist of 4 steps and are as follows:

Step 1. Guess the electron density: trial $n(r)$

Step 2. Solve the Kohn-Sham equations with $n(r)$, obtain single electron wave functions $\Psi_i(r)$

Step 3. Calculate the electron density based on the single-electron wave functions.

$$n(r) = 2\sum_i \Psi_i{}^*(r)\Psi_i(r) \quad \text{..... (22)}$$

Step 4. Compare the new electron density $n(r)$ with the initially approximated electron density $n(r)$ from step 1. The steps are illustrated in Figure 5.

There are two conditions to consider before concluding about the electron density, namely,

a. If the new density differs from the approximated density, repeat step 1 with the new electron density as the approximated density.

b. If they are both the same, the genuine ground state electron density has been determined.

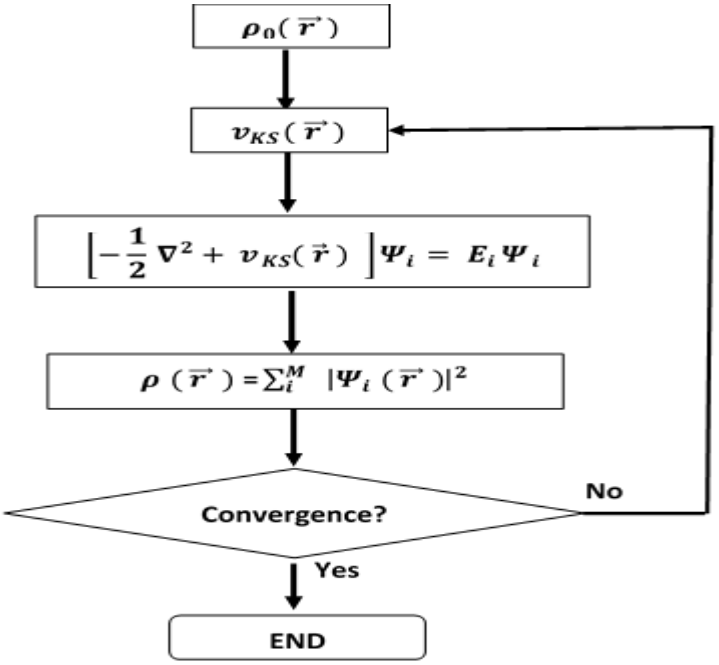

Figure 9. Flow chart of a typical DFT calculation within the Kohn-Sham method [81]

The above formulation assumes that the exchange-correlation functional is known. Because numerical exchange correlation potentials for a few basic model systems have yet to be discovered, most current density functional computations rely on the local density approximation. At any point r, the LDA approximates the exchange (XC) functional to a simple function of density [82]. This function's value is the XC energy per electron in a uniform homogeneous electron gas with density $n(r)$. The LDA expression for $E_{XC}[n(r)]$ is as follows:

$$E_{XC}[n(r)] \approx \int E_{XC}(n(r))n(r)\,dr \quad \text{.....} \quad (23)$$

The LDA is remarkably accurate, but often fails when the electrons are strongly correlated as in systems containing d and f orbital electrons [83].

3.4.8. Correlation functionals

The most utilised functionals are the LDA and GGA functionals for improved band gap approximations. GGA functional is based on gradients of electron density, whereas LDA is based on local electron density and is solely dependent on one variable (the density).

3.4.8.1. Local Density Approximations

In density functional theory, local density approximations are a type of approximation to the exchange-correlation (XC) energy functional [84]. They are entirely dependent on the estimation of the electrical density at each place in space. Several methods can produce local approximations to the XC energy. Nearby approximations that have been established from the homogeneous electron gas (HEG) are quite successful [85]. As a result, LDA is mostly identical with functional when examining the HEG estimate, which is subsequently linked to practical frameworks.

The functional of exchange-correlation is estimated as [86].

$$E_{xc}^{LDA}[\rho] = \int \rho(r)\varepsilon_{xc}(\rho)dr \quad \text{..... (24)}$$

where ρ is the electronic density ε_{xc} is the exchange-correlation energy per molecule of a homogeneous electron gas of charge density. The exchange-correlation energy is decayed into exchange and correlation terms linearly and can be expressed as [86].

$$E_{xc} = E_x + E_c \quad \text{..... (25)}$$

so that different expressions for E_x and E_c are looked for. The exchange term goes up against a straightforward systematic frame for the HEG.

Local density approximations are essential in the development of more complex exchange-correlation energy approximations, such as generalized gradient approximations or hybrid functionals, because an appealing property of any exchange-correlation functional is that it duplicates the correct HEG consequences for non-differing densities. LDAs are frequently an express component of such functionals in this capacity.

3.4.8.2. Generalised Gradient Approximation

Because the LDA approximates the energy of the true density by the energy of a local constant density, it falls flat in situations where the thickness changes rapidly, such as in atoms. Consider the slope of the electron density, the purported generalised gradient approximation, to change this. The LDA exchange-correlation is an inhomogeneous system in non-local density for the electrons it contains, which is referred to as inclination modification [87], giving the GGA exchange-correlation energy:

$$E_x^{GGA}c(n) = \int dn(r)\varepsilon_{xc}^{GGA}[n(r), \|\nabla n(r)\|] \quad \text{..... (26)}$$

where ε_{xc} is the exchange correlation energy and $n(r)$ is the gradient term of the electron density. The GGA has been broadly utilised and has turned out to be very fruitful in remedying a portion of the inadequacies of the LDA. In many cases, GGA is used concurrently with LDA as it provides improvements to certain features of LDA such as reduction in the over binding.

3.4.9. Plane-wave Pseudopotentials method

The plane-wave pseudopotential approach has evolved into a powerful and dependable instrument for studying the characteristics of a wide range of materials. The method's basic idea is to simplify the DFT problem by just considering valence electrons. This approximation is well understood and provides a number of computational advantages, such as fewer electronic states in solid-state calculations, smooth and node-less pseudo-wave functions in the core region, both pseudopotentials and pseudo-wave functions can be efficiently represented using a plane wave basis set, the pseudopotential is much weaker in the core region than the true Coulomb potential of the nucleus and it does not have a singularity at the position of the nucleus [88,89].

3.4.9.1. Plane-wave basis set

The plane-wave pseudopotential technique represents the orbitals using the plane-wave basis set. The wave function is defined as the product of the periodic part of the cell and a wavelike part:

$$\Psi k_i(r) = e^{ik.r} f_i(r) \quad \text{..... (27)}$$

The first term is the wavelike part of the wave function, and the second term is the cell periodic part. This can be described by splitting it into a finite number of plane waves, the vectors of which are the crystal's reciprocal lattice vectors, as given by:

$$f_i(r) = \sum_G G_{i,G}\ e^{iG.r} \quad \text{.....(28)}$$

where G represent reciprocal lattice vectors given by $\mathrm{G}.I = 2m\pi$ for I, where I is a lattice of the crystal and m is an integer [90]

3.4.9.2. Pseudopotential method

Pseudopotentials are used to represent nuclei and core electrons in the plane-wave pseudopotential technique. The pseudopotential is an attempt to substitute the intricate effects of an atom's core electrons' motion and its nucleus' effective potential, or pseudopotential, thus Schrödinger equations incorporate a modified component for core

electrons ordinarily found in the Schrödinger equation [91,92]. Figure 10 illustrates the ionic potential (Z/r), the valence wave functions $\Psi_{(Z/r),}$ the corresponding pseudopotential V_{pseudo} and pseudo-wave function Ψ_{pseudo} respectively [88]

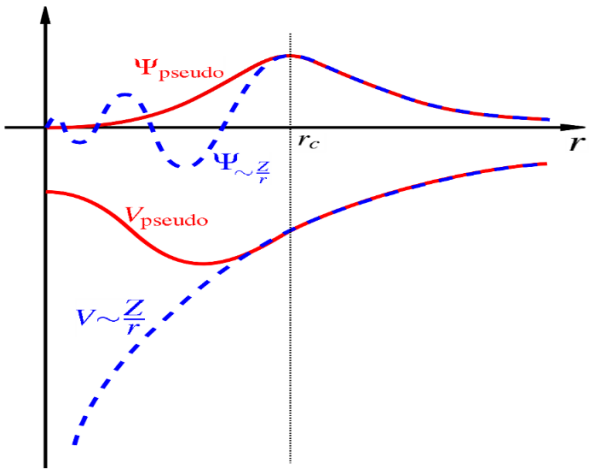

Figure 10. Comparison of wave function in the Coulomb potential of the nucleus (blue) to the one in the pseudopotential (red). The real and the pseudo wave functions and potentials match above a certain cut-off radius r_{cut} [92]

The advantage of utilising the pseudopotential approximation is that it allows the electronic wave function to be expanded using a substantially smaller number of plane wave basis states, requiring less computational time for energy convergence.

A local pseudopotential is one that employs the same potential for all the angular momentum components of the wave function. A local pseudopotential is a function that only depends on the potential's distance dependence. Kleinmann and Bylander's norm-conserving potential (NCP) is an example of a non-local pseudopotential, with a separate potential for each angular momentum component of the wave function [93]

3.4.10. Material studio

Material studio is a complete modelling and simulation environment designed to allow researchers in various fields to predict and understand the relationships of a material's atomic and molecular structure with its properties and behavior. Using Material Studio, researchers in most industries are manufacturing better performing materials of all types including pharmaceuticals, catalysts, polymers and composites, metals and alloys,

batteries, and fuel cells and more [94]. Within the material studio software, we have Cambridge Serial Total Energy Package (CASTEP) which enables us to perform density functional theory calculations.

3.4.11. Cambridge Serial Total Energy Package

CASTEP is a commercial software that calculates the electrical characteristics of crystalline solids, surfaces, molecules, liquids, and amorphous materials from first principles using density functional theory using a plane wave basis set. The properties of any material that can be thought of as an assembly of nuclei and electrons may be estimated, with the sole limitation being the computers' limited speed and memory. Surface chemistry, structural properties, band structure, density of states, and optical properties are examples of typical uses. CASTEP can also be used to investigate the spatial distribution of a system's charge density and wave functions, as well as the properties of both point defects (vacancies, interstitials, and substitutional impurities) and extended defects (such as grain boundaries and dislocations) in semiconductors and other materials [94].

3.4.12 Computational Details

The structure of the dye molecule was built using Material Studio on 3D atomistic window, the molecule was cleaned so that the atoms are re-oriented on their lattice position. Geometrical optimizations of the dye molecule were performed using the first principles calculations based on density functional theory (DFT) which uses a plane-wave pseudopotential method. We used generalised gradient approximation (GGA) in the scheme of Perdew-Bruke-Ernzerhof (PBE) to describe the exchange-correlation functional using the coarse quality and all band/EDFT as electronic minimizer.

The calculations were conducted using Cambridge Serial Total Energy Package (CASTEP) code, which is a package within the framework of the Materials Studio software to obtain the ground state properties of the dye molecule. Then the calculations of electronic properties of dye molecules were done using Vulnerability Analysis Methodology Program (VAMP). The dye molecules were then imported to a new 3D atomistic window, the electronic levels and energy orbitals of the dye molecules were then calculated to determine the UV-VIS spectrum graph of the dye molecule and on the orbitals, we get to view the HOMO and LUMO values for the dye molecules.

The plane-wave pseudopotential method generalised gradient approximation (GGA) in the scheme of Perdew-Burke- Ernzerhof (PBE) to describe the exchange-correlation functional and the cutoff energy for plane-wave basis set to 500 eV, 5 x 2 x 2 Monkhorst-pack was used in DFT calculation with all band/Ensemble density functional theory (EDFT) as electronic minimizer. All structures were inside the vacuum slab of 10.00 Å vacuum thickness, 17.552 Å and 0.00 Å slab position.

Anatase TiO_2 bulk structures were also optimized using CASTEP code within the framework of the Material Studio package to obtain the ground state properties of the anatase TiO_2 structure, GGA-PBE functional for determination of convergence parameters and geometrical optimization of anatase TiO_2 structure were used, the fixed basis set and ultra-soft pseudopotential was used throughout the study. The ground state structures obtained through geometrical optimization with the convergence parameters were imported into a new 3D atomic window and the surfaces were cleaved from the bulk structure and a vacuum slab of appropriate size was built for the surface structures. The surfaces were optimized using the same convergence parameters obtained for the bulk structures. The dye/TiO_2 complex was optimized to obtain the ground state structures, and the electronic properties were calculated using CASTEP code.

CHAPTER 4

4.1. EXPERIMENTAL RESULTS AND DISSCUSION

4.1.1. Absorption of the effects of the solvent on the extraction of natural dye from *B. pilosa* leaves

Selecting an appropriate solvent for extraction of natural dye plays a vital role in enhancing the absorbance of a dye to absorb more photons in a broad spectrum. The solvents such as distilled water, ethanol and methanol are polar solvents. The absorption spectra of extracts dye from *B. pilosa* using different solvents were compared as shown in Figure 11.

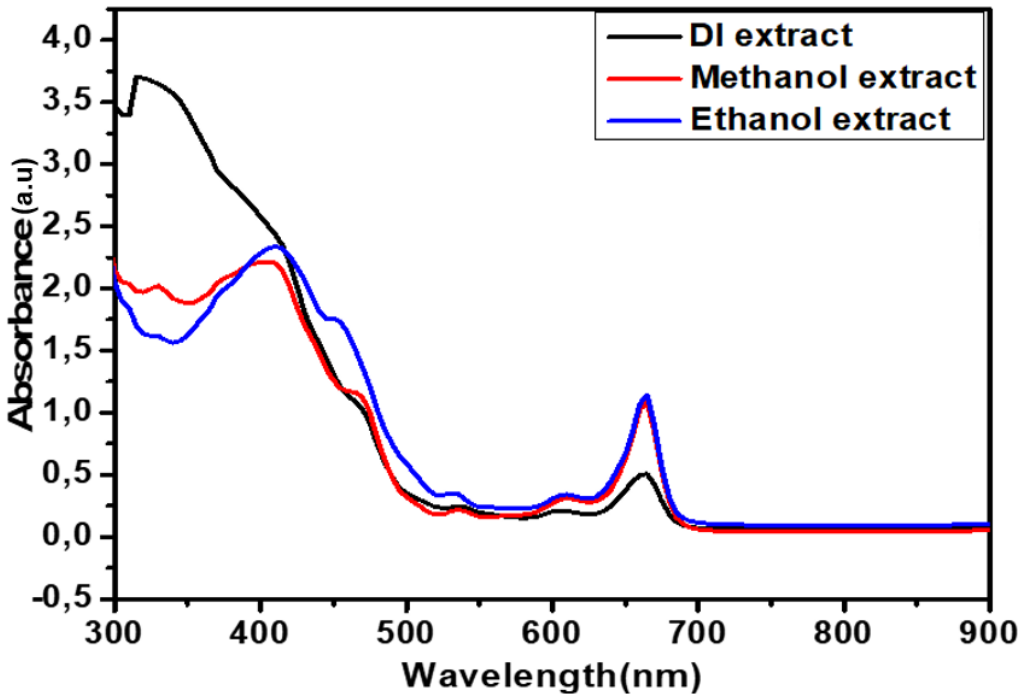

Figure 11. Absorption spectrum of *B. pilosa* extracts

In the UV-vis absorption spectra, dye extracted using different solvents exhibits different absorption peaks. The existence of various photosynthetic pigments in the leaves of *Bidens pilosa* in the visible spectrum accounts for the difference in absorption spectra (400–700 nm). From figure 11, the absorption peaks of the dye in ethanol are observed at a wavelength of 415, 455 and 665 nm, methanol at 415, 438 and 665 nm, while for water a was observed at 320 and 665 nm. The existence of chlorophyll pigment is indicated by the absorption peak detected in the wavelength ranges 400-440 and 665 nm, whereas the presence of betalain pigment is indicated by the peak observed around 536 nm [20-23] and this work concurs well with the reported work by Adedokun O *et al* [63]. *B. pilosa*

is identified to be rich in chlorophyll because all green plants contain chlorophyll, which is capable of photosynthesis process having glucose from simple organic molecules (water and carbon dioxide) under the action of visible light [39,43].

The ethanol extraction of chlorophyl shows a better and broader absorption in the visible range of the spectrum as reported previously on literature by Syafinar R *et al* [15], which corresponds with the current work. The absorption spectra of the dye extracted from *B. pilosa* shows the strongest absorption band at 665-669 nm, which corresponds to a molecule of porphyrin and pheophytin found within the *B. pilosa* plant [15,42,57,95], and this work is in good agreement with the work done previously [19,35,64,66]. The increased absorbance of ethanol solvent may be related to the nature of chemical compounds found in *B. pilosa* extracts having a higher ability to dissolve in polar solvents [63].

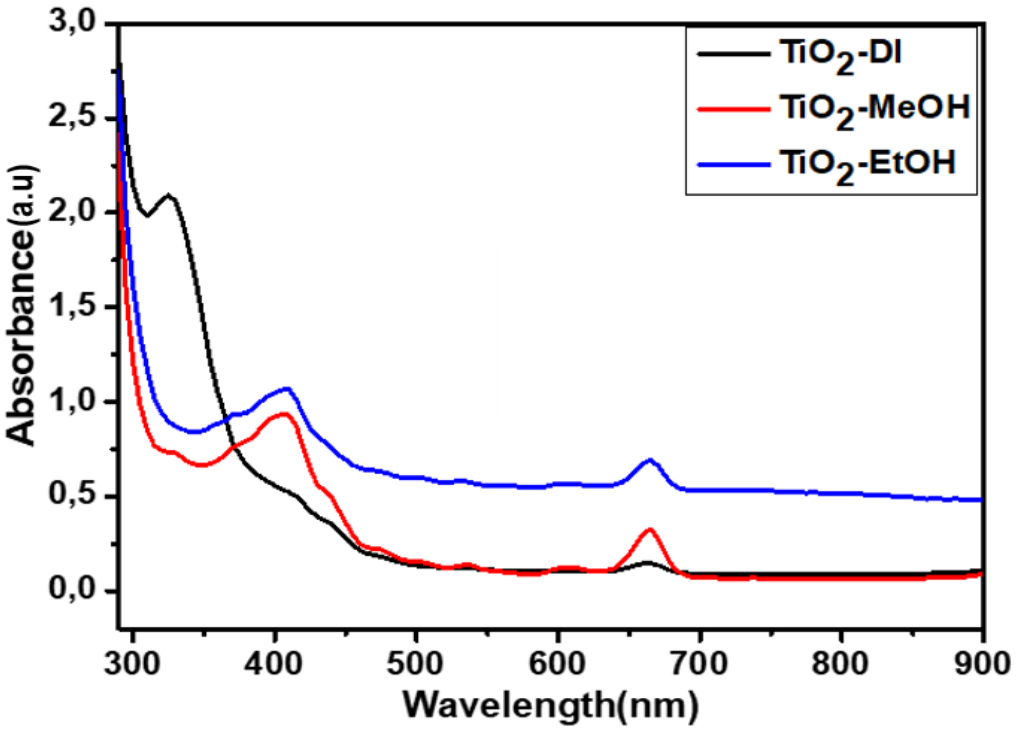

Figure 12. Absorption spectrum of synthesized TiO_2 using *B. pilosa*

In addition to the absorption spectrum, *B. pilosa* dye absorbed onto the surface of TiO_2 NPs was observed to decrease in intensity without change in the peak position or wavelength. The decrease in the chlorophyll absorption value after the addition of TiO_2-NPs suggests electronic level interaction of the nanoparticles with the surface of the dye molecules [23]. The decrease indicates the possibility of the adsorption of chlorophyll on

the surface of nanoparticles and the formation of the ground-state complex of the chlorophyll-titanium oxide. The addition of nanoparticles to the chlorophyll-titanium interaction does not modify the peak location of chlorophyll, indicating that the produced complex similarly exhibits absorption at 665 nm [23]. As a result, the strength of chlorophyll absorption at the same peak position decreases, the increase in absorbance and the existence of peaks with dye loading indicate the dye molecules' anchoring and chemical interaction with the TiO_2 photoanode.

According to Figure 12, the chlorophyll dye extracted with ethanol absorbed better on the surface of the TiO_2 photoanode [39,54,] and this work agrees well with previous work [57], it was also observed that TiO_2 showed absorption only in the UV region with the absorption edge around 405 nm. The absorption bands of sensitized TiO_2 revealed a redshift that is likely caused by the existence of adsorbed chlorophyll [39]. A similar result of the extension of absorption of the sensitized TiO_2 was reported from computational investigation by Elegbeleye *et al* [97],

However, after adsorption of CR1 and CR2 dye molecules on TiO_2 brookite cluster, a bathochromic shift was observed. Furthermore, their findings imply that the dye molecules have good optical properties, which verify previous studies that dye adsorption on TiO_2 improves optical response and helps overcome its low spectral sensitivity in the visible region. As a result, photocatalytic characteristics and overall DSSCs device efficiency improved, which is associated with the redshift observed in the current work. Comparable results were reported previously [96], for mono-doped and co-doped (210) surfaces, suggesting that the absorption shifted toward longer wavelengths, reflecting an increase in visible light absorption.

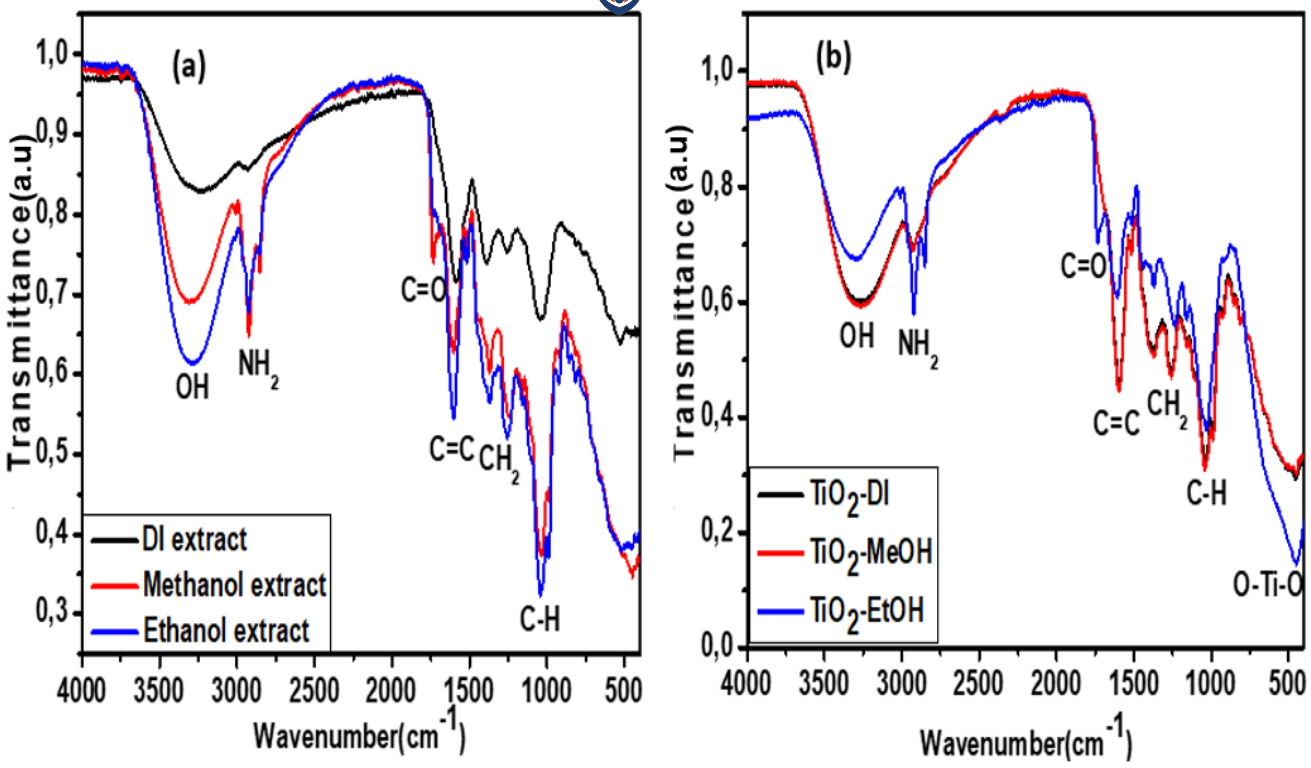

Figure 13. (a) FTIR spectra of *B. pilosa* extracts and (b) synthesized TiO_2 using *B. pilosa*

FTIR analysis was conducted to examine and identify the possible functional groups found in the green extraction and green synthesized TiO_2 nanoparticles using *B. pilosa* plant. The recorded FT-IR spectra of the natural dyes extracted from *B. pilosa* in Figure 13 (a) and (b) shows most of the characteristic peaks of the chlorophyll derivatives such as pheophytin, porphyrin, and chlorins [53].

Chlorophylls and their derivatives have characteristic infrared bands corresponding to C=O, C=C, C-H, and N-H groups. The characteristic C=O band corresponding to the ketone in the cyclopentanone ring of pheophytin a is observed at 1735 cm^{-1} for both extraction and synthesis, similarly, the C=C vibrations of pheophytin a are observed at around 1610 cm^{-1} and 1600 cm^{-1} for extracts and synthesis respectively which is in good agreement with the work reported previously [52,53] Vibrational bands positioned at 2850 cm^{-1} to 2927 cm^{-1} are contributed to the N-H stretching of amide II [52]. The region from 1310 cm^{-1} and 1376 cm^{-1} are contributed to the amide III vibration and the CH_2 [42,52,53,98] the wave number at 1225 cm^{-1} is assigned to the stretching vibrations of C-O for the ester groups [52,98].

Vibrational bands positioned around 3340 cm^{-1} showed the presence of the OH group in both extracts and synthesized extracts of *B. pilosa,* the presence of alcohol is due to the solvents used during the extraction process. The vibration peak of O-Ti-O identified at 497 cm^{-1} in Figure 13 (b) confirms the formation of TiO_2 appearing at the fingerprint region below 1000 cm^{-1} which agrees with the work of Ahmad *et al* [98]. In their work on green synthesis of TiO_2 nanoparticles using Mentha arvensis leaves extracts, they observed the absorption vibrational band at 596 cm^{-1} which also indicates the O-Ti-O bond and is similar to the current FTIR results at 497 cm^{-1} absorption peaks [54,98]. It has been previously reported that the natural dyes extracted with functional groups such as (–OH) and (C=O) show a higher efficiency of absorbance [54]. The FT-IR spectral analysis also confirms the presence of Porphyrin and Pheophytin molecules found in *B. pilosa* extracts, which is well-matched with the UV–Vis obtained in Figure 11.

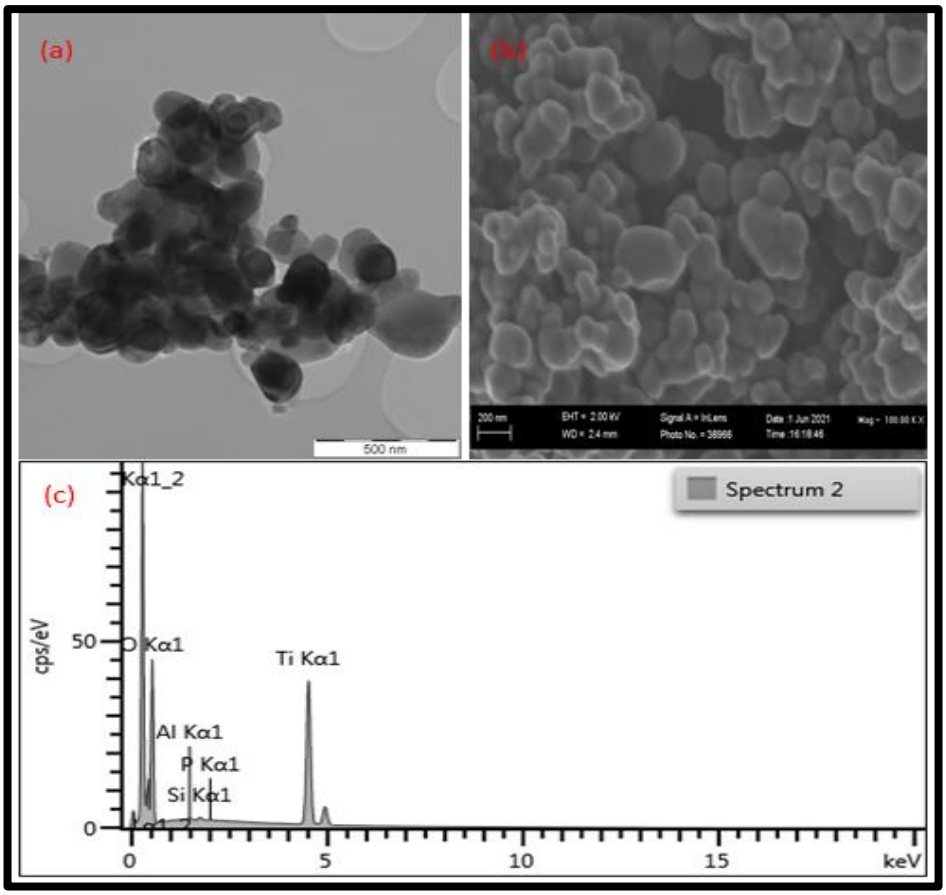

Figure 14. water (a) TEM, (b)SEM, (c) EDS

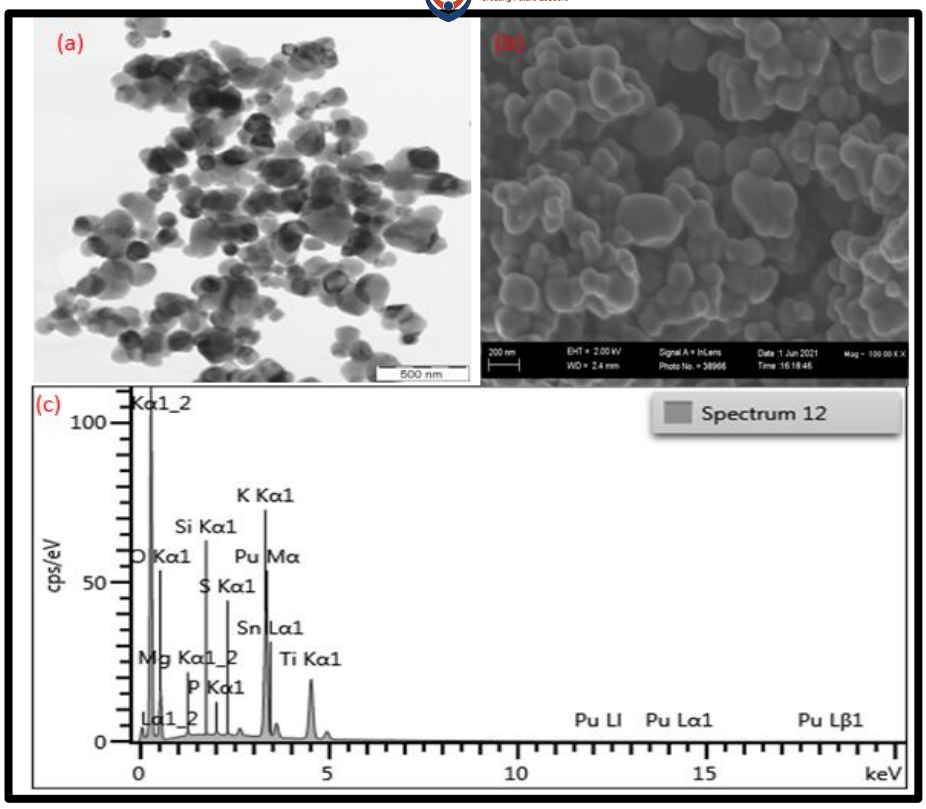

Figure 15. methanol (a) TEM, (b)SEM, (c) EDS

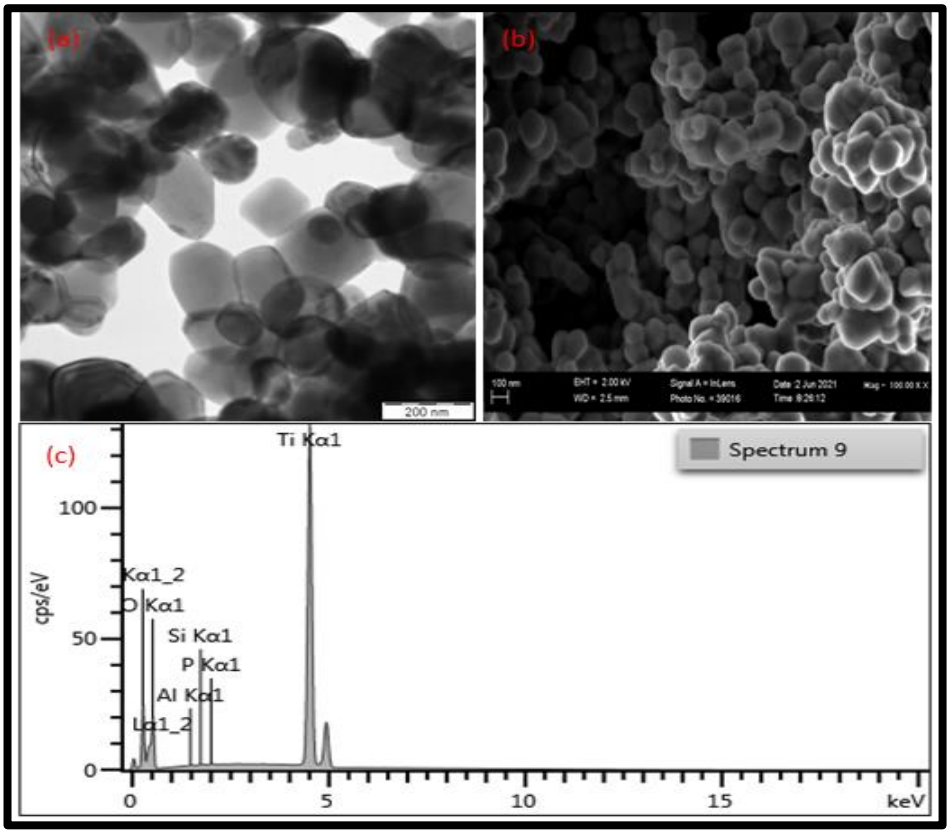

Figure 16. ethanol: (a) TEM, (b)SEM, (c) EDS

TEM and SEM were used to examine the morphological properties of the produced nanoparticles. Figures 14, 15, and 16 show TEM, SEM, and EDS images of nanoparticles produced from *B. pilosa* leaf extracts. The TEM and SEM images of produced nanoparticles show that the particles are spread in a spherical form, despite some aggregation and agglomeration. The tendency of the particles to agglomerate was directly related to the crystal size obtained; EDS analysis indicates the presence of elements such as Ti and O, which confirms the presence of TiO_2 NPs; and other elements such as potassium (K), aluminum (Al), and silicon (Si) were observed for both water and ethanol and for methanol; magnesium (Mg), Plutonium (Pu), Si, K, and Al were observed. These are components that may be present in a *B. pilosa* plant. The elements Si, Mg, and Al were derived from chlorophyll nutritional components. Mg confirms the presence of chlorophyll in the leaves of *B. pilosa*. The findings of this study are consistent with previous reports of elemental Ti detection at 5 keV [99].

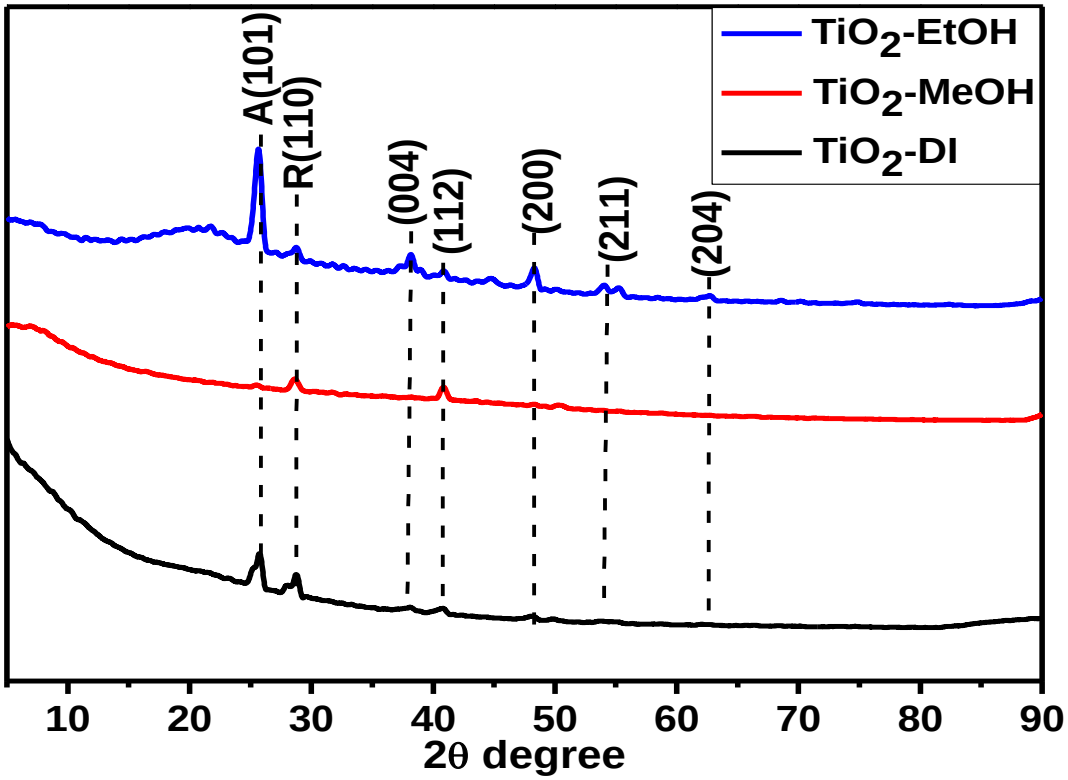

Figure 17. XRD pattern of synthesized TiO_2 nanoparticles

XRD patterns of TiO_2 nanocrystalline are shown in Figure 17. A relatively small 2θ range (22–30◦) and small scanning rate were chosen. For each pattern. As observed, there is a peak at roughly 25.4º, for each pattern, which is classified as anatase (1 0 1) phase.

There were no peaks found in the other two TiO_2 phases, rutile and brookite. The analysis result corresponds to that obtained in SEM and TEM studies in Figure 14, 15, 16 which is in good agreement with previous studies by Zhou *et al* [100] on TiO_2 sols synthesized by hydrothermal methods using tetra butyl titanate as material for application in DSSCs; they obtained a (1 0 1) anatase peak, which corresponds to our current work. Several De-bye-Scherrer peaks, however, such as (1 0 1), (0 0 4), (2 0 0), (2 0 4), were labeled with anatase phase PDF card no. 78-2486, which matches well to the XRD data reported in this work [96]. The peaks in Figure 13 show the anatase phase TiO_2 for all situations, as well as the XRD peaks for pure TiO_2 according to JCPDS-ICDD card no. 21-1272, which corresponds well to the peaks observed in our current results.

A mixture of two rutile peaks was detected, which could be attributed to the low temperatures used during the calcination process. According to the XRD results, the (101) surface of TiO_2 anatase can be used computationally by Material Studio Software to adsorb dye molecule that was extracted experimentally. Another reason for using the (101) surface of TiO_2 anatase as revealed in the XRD results is that anatase crystal is more photoactive and stable than rutile and brookite [101]. The anatase (101) surface is more interesting since it has a lower surface energy than the surfaces (001) and (100), and it has been observed to absorb small molecules on its surface.

4.2. COMPUTATIONAL RESULTS AND DISCUSSION

Table 1 illustrate the molecular structure of porphyrin and pheophytin molecule; the original structures are illustrated [102].

Table 1 Molecular structures of porphyrin and pheophytin dyes

Literature [102]		Material studio
compound	Molecular structures	Molecular structures in CASTEP
Porphyrin	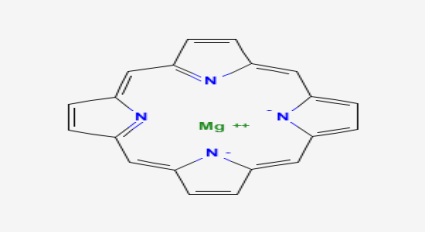	
Pheophytin	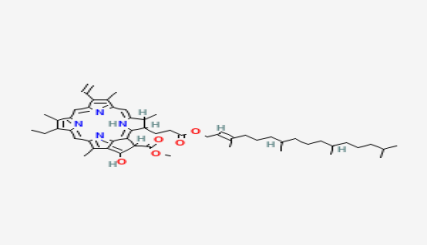	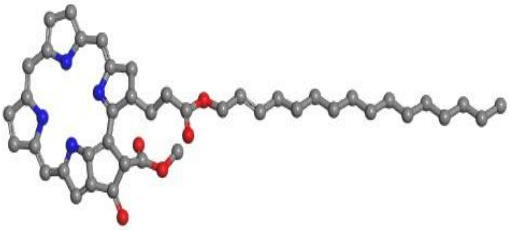

The formula of porphyrin is $C_{20}0H_{12}MgN_4$, porphyrin consists of four pyrrole rings (five-membered closed structures containing one nitrogen and four carbon atoms) linked to each other, at the center of the porphyrin ring, a magnesium ion helps to maintain the chlorophyll molecule and promote the photosynthetic process by transferring electrons down an electron transport chain. while the formula of pheophytin is $C_{55}H_{74}N_4O_5$, pheophytin is a chlorophyll molecule lacking a central Mg^{2+} ion and serves as the first electron carrier intermediate in the photosynthesis electron transfer pathway and the photosynthetic reaction in plants and has a phytol chain [103]

4.2.1. Absorption Spectrum of dye molecules

Absorption is vital for an organic dye to be recognised as the ideal sensitizer for usage in DSSCs. Organic dyes should be able to absorb photons in both the visible and near-infrared region of a solar spectrum.

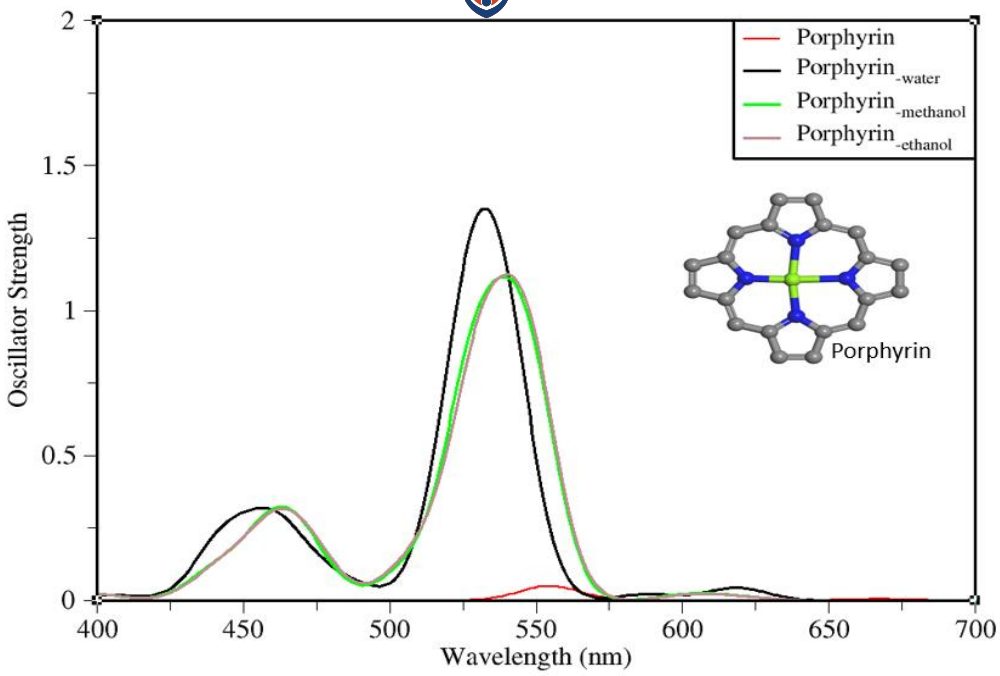

Figure 18. Absorption spectrum of porphyrin dye molecule and porphyrin dye with the effect of solvents and LHE

Before considering the effect of solvents, the porphyrin molecule exhibits minimal absorption in both the visible 550 nm and near-infrared 861 nm regions which contributes 6% of its LHE. When the porphyrin molecule was absorbed with solvents (water, methanol, ethanol) a stronger absorption was observed in the visible region at 534 nm, 538 nm, 542 nm respectively with a LHE of 95%, 92%, 92% respectively. It is observed in figure 18, that when the porphyrin molecule is absorbed with effects of solvents such as water, ethanol, and water, it tends to harvest more photons in the visible region of the solar spectrum but absorbs less photons in the nearer infrared region because its absorbance slows down but can still absorb photons in the nearer infrared region [19,35,37].

The computed absorption agrees well with the experimental results plotted in Figure 11. The pheophytin molecule absorbs photons at 754 nm with a LHE of 1.6% before the dye molecule is absorbed with the effects of solvents (water, methanol, ethanol). Both methanol and ethanol have a higher absorbance in the visible region at 538 nm and 541 nm corresponding to 92% of light harvesting efficiency and water 534 nm corresponding to 95%of LHE. Unlike the pheophytin molecule, the porphyrin molecule absorbs photons better on its own and when absorbed onto different solvents, it is observed that the

porphyrin absorbance tends to blue-shift and focus on the visible region harvesting more photons.

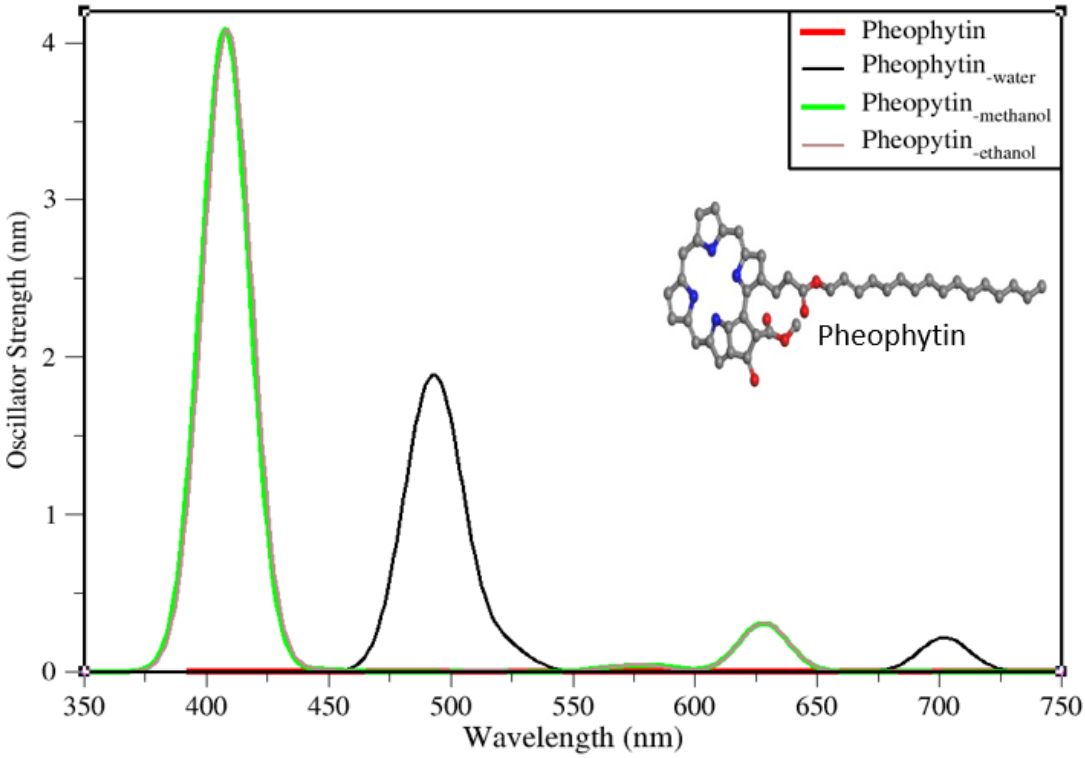

Figure 19. Absorption of pheophytin dye molecule and pheophytin dye with the effect of solvents and LHE

In Figure 19, pheophytin shows a lower absorbance of photons in both visible region and near infrared region with a lower absorbance resulting in lower efficiency, however, with the effect of solvents introduced on the pheophytin dye molecule, it is observed that methanol and ethanol solvents blue shift to the visible region and absorbs more photons at a higher oscillating strength resulting in obtaining higher efficiency in the visible region. Both methanol and ethanol have a higher absorbance in the visible region at 405 nm and 407 nm corresponding to 99% of light harvesting efficiency and water 494 nm corresponding to 98% of LHE which agrees well with the work done by Rahmatika *et al* [66].

This ability of absorbance causes the pheophytin molecule with effects of solvents such as methanol and ethanol to absorb more photons in the visible region also shows that pheophytin with effect of solvents of methanol and ethanol is suitable and can be the best sensitizer molecule in DSSC since it can absorb photon in both visible and near infrared

region [66,103]. However, without the effect of solvents, the pheophytin molecule absorbs less photon than that of porphyrin molecule in both visible and nearer infrared region unlike the porphyrin dye molecule which absorbs better in the visible region and nearer infrared region. Absorption in the visible region will greatly affect the efficiency of DSSC because it maximizes the absorption of photons [103]. The computational and experimental absorbance are in correspondence with each other since the porphyrin and pheophytin molecule has an absorbance in both visible and nearer infrared region and can be observed in Figure 11 and 12 for both absorbance spectra this is comparable to the work done by Li Y *et al* [52]

4.2.2. Light Harvesting Efficiency of dye molecules

The performance of DSSCs is evaluated by the incident photon to conversion efficiency (IPCE). It is associated with a charge collection efficiency ($\boldsymbol{\eta_c}$), electron injection efficiency ($\boldsymbol{\Phi_{injec}}$), and light harvesting efficiency (LHE), [104]

IPCE = LHE x $\boldsymbol{\Phi_{injec}}$ x $\boldsymbol{\eta_c}$ ……..…… (29)

LHE(λ) can be calculated as follows.

LHE (λ) =$\mathbf{1} - \mathbf{10}^{-f}$ …… (30)

Where f is the absorption of the dye associated with the maximum absorption also called the oscillator strength and $\boldsymbol{\Phi_{injec}}$ is related to the free energy of electron injection [60]. $\boldsymbol{\eta_{collect}}$ is the charge collection efficiency. For the same DSSCs with only different dyes, it is reasonable to assume that $\boldsymbol{\eta_{collect}}$ is constant. The light-harvesting efficiency (LHE) of a dye should be high to upgrade the photocurrent response [104] LHE is related to the oscillator strength ($\boldsymbol{f}$) at a given ($\boldsymbol{\lambda_{max}}$) maximum wavelength.

LHE (λ) is the light harvested at a given wavelength, which is determined by the maximum absorption of wavelength. Sensitizers with high LHE (λ) guarantees a better photocurrent response [104]. Therefore, it is not difficult to understand that LHE (λ) is an important parameter for evaluating the energy conversion efficiency (η) of DSSCs. Oscillator strength expresses the probability of absorption and the strength of transitions to the excited state, the calculated LHE (λ) against absorption wavelength for the pheophytin dye molecule is tabulated in table 2 and was calculated using equation (30).

Table 2. Calculated Light Harvesting Energy of porphyrin and pheophytin dye molecule.

Dye molecule	$\lambda_{max\ (nm)}$	f (Oscillator strength)	LHE (λ)	LHE (%)
Porphyrin	554	0.49	0.106	1.6
	861	0.027	0.06	6
Pheophytin	754	0.0017	0.0159	1.6
	523	0.006	0.013	1.5
Porphyrin-water	458	0.317	0.51	51
	534	1.34	0.95	95
Pheophytin-water	494	1.88	0.98	98
	703	0.215	0.39	39
Porphyrin-methanol	462	0.32	0.52	52
	538	1.11	0.92	92
Pheophytin-methanol	405	4.04	0.99	99
	626	0.3	0.49	49
Porphyrin-ethanol	462	0.315	0.51	51
	541	1.12	0.92	92
Pheophytin-ethanol	407	4.07	0.99	99
	629	0.51	0.69	69

Pheophytin shows a lower absorbance from visible and nearer infrared region at 523, 754 nm with a LHE of 1.6% however porphyrin shows a significant absorption in both visible and nearer infrared region at 861 nm with a LHE of 6%. In addition, to solvents both

porphyrin and pheophytin molecule blue-shifts and absorbs photons strongly in the visible region. Pheophytin has broader absorption in both methanol and ethanol at 405, 402 nm responding to a LHE of 99% while that of porphyrin in both methanol and ethanol at 538, 541 nm responding to a LHE of 92%. The porphyrin molecule shows a slight redshift in the spectrum. This dye molecule shows a potential as a promising sensitizer that can be used in DSSCs and among the solvents used, ethanol is the best solvent that can be used since it shows a broader absorption in the visible and nearer infrared region. This computational work agrees well with our experimental work in both Figures 11 and 12.

4.2.3. Energy level and Isodensity of dye molecules

The HOMO-LUMO gap is the energy difference between HOMO and LUMO, HOMO is the highest occupied molecular orbital which represents a donating ability of electrons; LUMO is the lowest unoccupied molecular orbital which represents acceptability of electrons [105]. The size of transition metal complexes from HOMO to LUMO by the dye can be used to predict their strength and stability. Molecular orbitals and their properties such as corresponding energy are especially useful to identify the best sensitizers for DSSCs [105]. The HOMO represents the donating ability of electrons while LUMO represents acceptability of electrons [105]. The energy gap is generally the lowest energy electronic excitation that is possible in a molecule. Table 3 shows the HOMO, LUMO, and HOMO-LUMO energy gaps of the pheophytin and Porphyrin dye molecule, equation (31) was used to calculate the HOMO-LUMO energy gap.

$$E_{gap} = HOMO - LUMO \quad \text{(31)}$$

Where $\boldsymbol{E_{gap}}$ is the energy gap of HOMO and LUMO

Table 3. The HOMO, LUMO and HOMO-LUMO energy gap of porphyrin and pheophytin dye molecule

Molecules	HOMO	LUMO	E_{gap} (eV)
Porphyrin	-7.031	4.26	2.8
Pheophytin	-7.656	-5.596	2.1
Porphyrin-water	-8.742	-5.08	3.7
Pheophytin-water	-8.391	-5.596	2.7
Porphyrin-methanol	-8.703	-5.091	3.6
Pheophytin-methanol	-8.568	-5.02	3.5
Porphyrin-ethanol	-8.703	-5.091	3.6
Pheophytin-ethanol	-8.235	-4.985	3.2

A smaller energy difference between the sensitizer's HOMO and LUMO increases photon absorption in higher spectral regions of the solar spectrum [66,106]. The porphyrin dye molecule has a significantly lower HOMO-LUMO energy gap of 2.8 eV and is higher than that of pheophytin which can still allow electron excitation. High HOMO energy indicates the reaction of high compounds/molecules, which will facilitate electron transfer and the formation of chemical bonds. A low HOMO suggests that the compound/molecule is stable, making it less reactive [66]. High LUMO energy for dye molecules allows electron injection from the semiconductor, resulting in faster dye recombination to ground state complex [66,106].

The HOMO and LUMO energies of pheophytin and pheophytin with the effect of solvents are shown in Figure 20The HOMO–LUMO energy gap values for pheophytin is 2.1 eV, while for pheophytin with effect of solvents (water, methanol, and water) are 2.7 eV, 3.5 eV, 3.2 eV respectively which agrees well with the HOMO and LUMO values reported by Yuanzuo *et al* [52] on photoactive layer of DSSC based on natural dyes. The lower HOMO-LUMO energy gap of the sensitizer enhances absorption at higher wavelength and the photocurrent response of DSSCs [52]. A lower energy gap between the HOMO and LUMO of sensitizer

enhances the absorption of photons in higher spectral regions of the solar spectrum. The pheophytin dye molecule relatively has low HOMO-LUMO energy gap of 2.1 eV, in dye molecule with a relatively low HOMO-LUMO energy, pheophytin and pheophytin$_{ethanol,}$ shows the basis for determining the ability of a molecule to become a sensitizer in DSSC and this agrees well with the reported work by Rahmatika *et a*l [66]. LUMO energy must qualify for having energy above the TiO_2 semiconductor conduction band of -4.2 eV [107] terms.

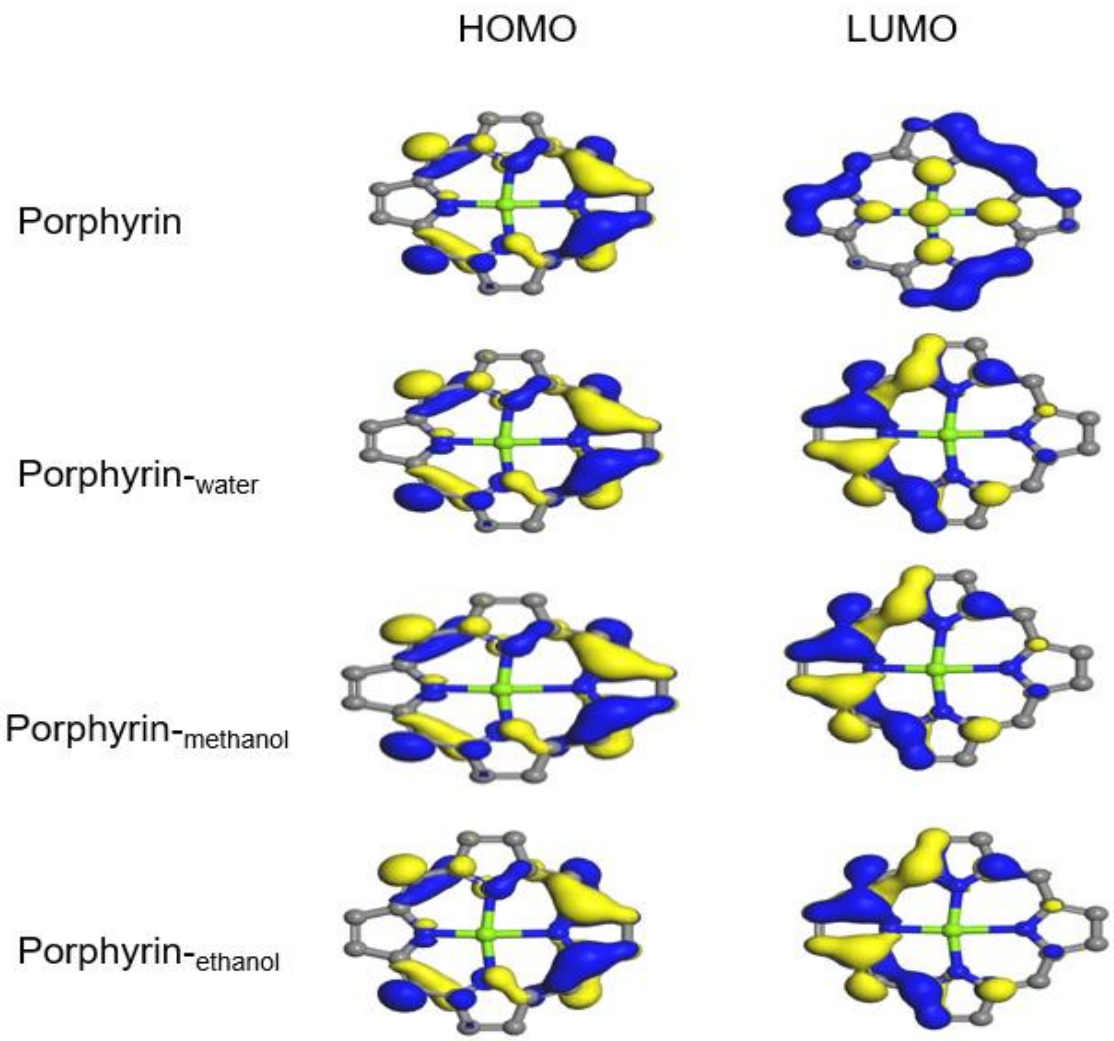

Figure 20. Isodensity of porphyrin dye molecule

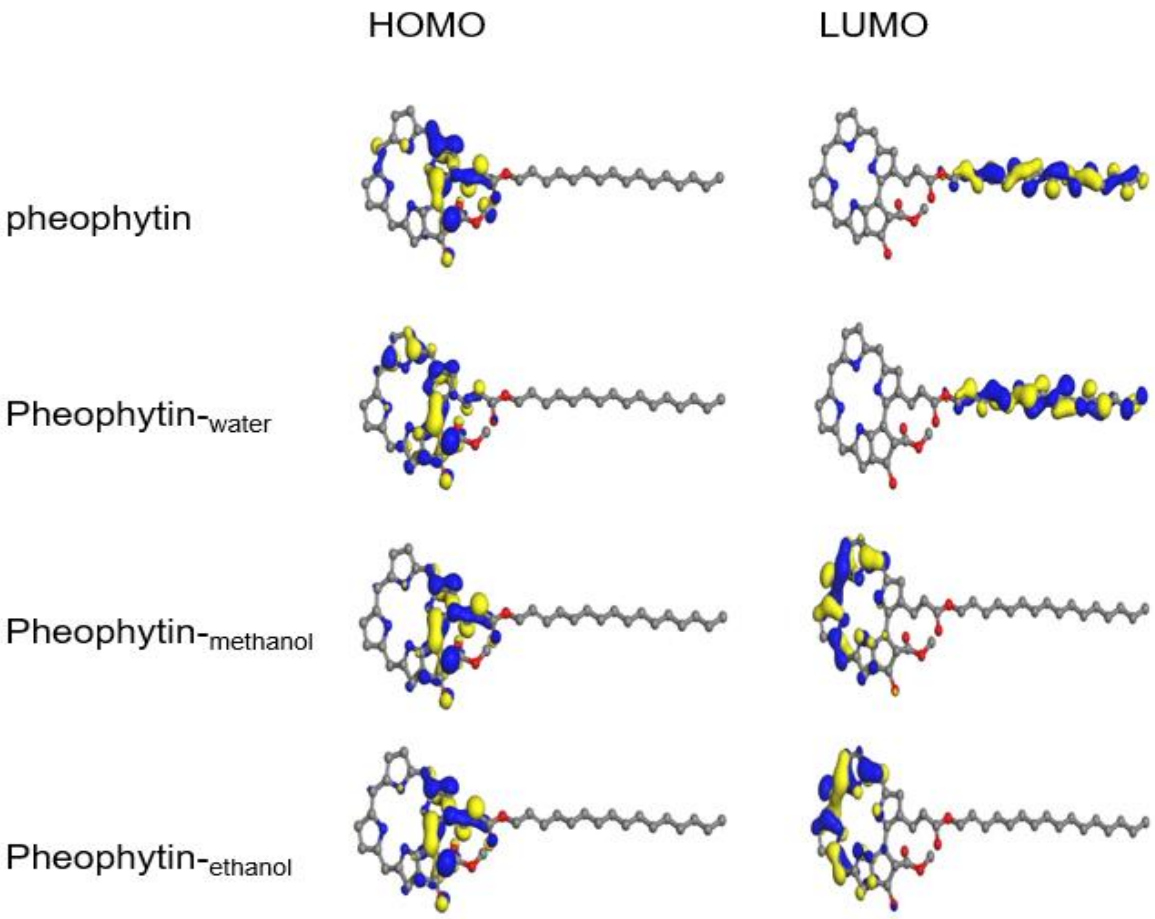

Figure 21. Isodensity of pheophytin dye molecule

Figures 20 and 21 illustrate the location of HOMO and LUMO orbitals on a dye molecule. The frontier orbitals of the molecules are centered on the porphyrin ring but not on the phytol chain for both methanol and ethanol solvents on a pheophytin molecule. This gives a consequence that the structure of porphyrin ring will be responsible for most of the electronic transition involved such as absorption, emission, and charge transfer. The distribution of electrons between HOMO and LUMO mostly contributes to electronic transitioning of the molecules involving photons that provide high oscillating strength for both HOMO and LUMO transitions [43,108-109].

since the porphyrin molecule is prominent in our computational calculations, The longer phytol chain observed in pheophytin molecule distinguishes it from porphyrin molecules.

According to our recent findings, the pyrrole ring found on porphyrin and pheophytin molecules appears to be the one that shows most of the molecule interaction. When we analyze HOMO-LUMO, we observe that the frontier molecules are not concentrated on the phytol chain, but on the porphyrin, ring known as pyrrole. This implies that most of the electronic transitions will be caused by the structure of the porphyrin ring [43,108].

Furthermore, creating a supercell for the pheophytin molecule to be adsorbed onto TiO_2 proved to be difficult since the memory required exceeded the machine capacity, making it impossible to continue with computations for a pheophytin molecule. As a result, the obtained results will be focused on the porphyrin molecule from this point onward.

4.2.4. Convergence tests and geometry optimization

The current quantum-mechanical computations were conducted using the density functional theory and pseudopotential methods as implemented in the first principle calculation program CASTEP code [78]. Under extended gradient approximation, the Perdew, Burke, and Ernzerhof (PBE) approach was utilized to address electronic exchange correlation energy [110]. We initially created an acceptable cut-off energy and associated k-points to determine the optimal conditions at which the bulk structure of TiO_2 anatase would be more stable. Convergence tests were conducted to find a suitable cut-off energy and k-points for evaluating the system; the total energy measured against the bulk structure of TiO_2 anatase is displayed in Figure 22. The graph became stable at 500 eV, suggesting that the energy had converged, therefore a cut-off energy of 500 eV was selected and used to conduct all calculations throughout the investigation.

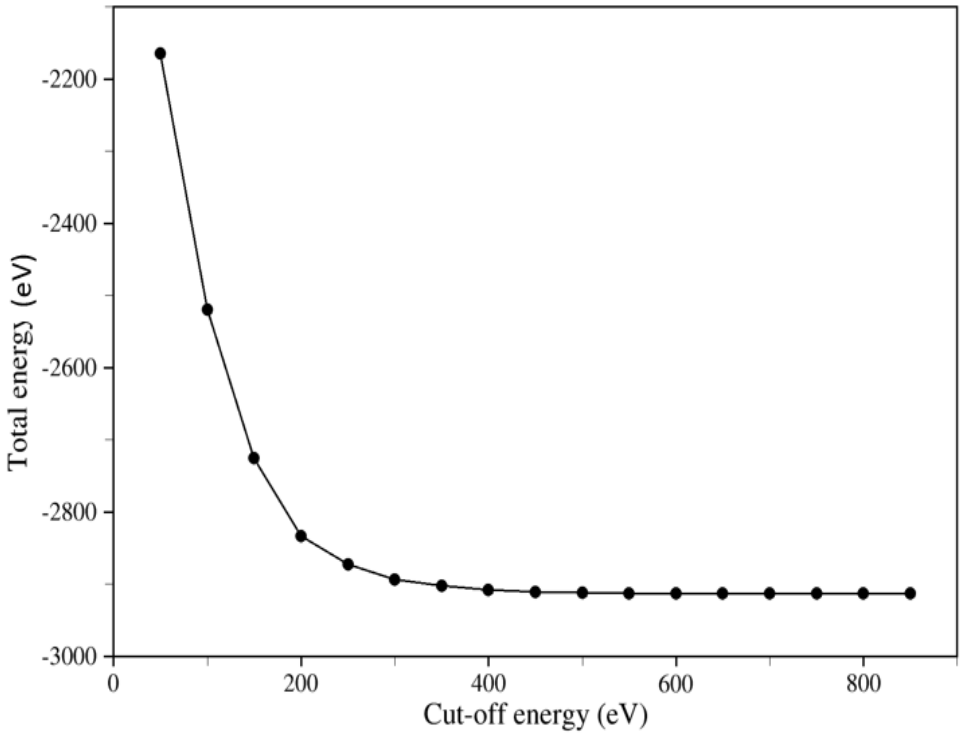

Figure 22. Total energy against plane wave basis set cut-off for TiO_2 anatase bulk structure

The energy obtained from each cut-off energy was recorded. The ground state energy was chosen to be at 500 eV, cut-off energy value corresponding to a total energy of -2912.42 eV and was used to determine all optical properties in this study. The graph shows that the ground state energy becomes stable at -2912.42 eV and has a constant value starting at 500 eV. Zhao *et al* employed a cut-off energy of 440 eV, which is close to the established cut-off energy, to expand the Kohn-Sham wave functions [110].

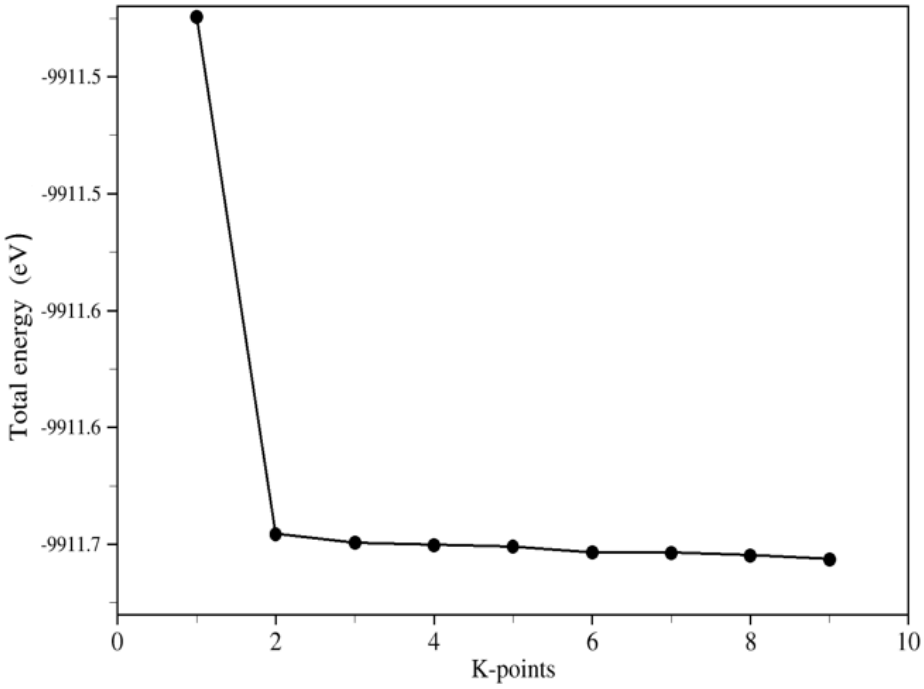

Figure 23. Graph of energy formation versus the number of k-points

Figure 23 illustrates the number of K-points that yielded the lowest total energy, and the calculated minimum total energy was -9911.72 eV, which corresponds to the 5 x 5 x 2 K-points. Thus, 9 K-points were found in this work that corresponded to 5 x 5 x 2 for the Brillouin zone integration, resulting in a stable graph from that point on. As a result, all geometry optimization and characteristics simulations for the bulk structure were performed using a 500-eV cut-off energy and 5 x 5 x 2 of K-points.

4.3. Structure properties

Anatase, including rutile and brookite, is a component of the TiO_2 polymorphs group [112]. Geometry optimization on the anatase TiO_2 bulk structure confirmed the model used in the investigation. The convergence test, as described in the preceding section, was used to determine a set of K-points and an energy cut-off that were employed in the computations. Geometry optimization computations with the unconstrained volume were performed in one step to find the equilibrium bulk parameters and corresponding energy. Figure 24 shows the TiO_2 bulk structure of anatase. TiO_2 anatase bulk structure before cleaving, it is made up of 31 atoms. Oxygen is represented by red, and Titanium is represented by grey color.

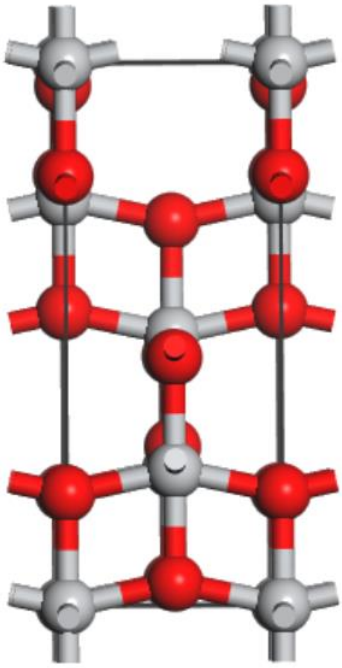

Figure 24. TiO_2 anatase bulk structure

The ground state energy structure for anatase TiO_2 bulk structure was determined by calculating the lattice parameters and their corresponding lowest energies. Table 4 compares the computed lattice parameters a, b, and c to previously reported experimental results and theoretical studies. The computed results and the ones reported by Theivasanthi *et al* [112,113] clearly correlate. The experimental data and lattice parameters determined in this work are comparable, with a variance of 0.0088% along a-, b-axis, and 0.0264% along c-axis. Several density functional theory methodologies [113] revealed that the results had a percentage inaccuracy that was within a tolerable and acceptable range, Table 4 compares practical and earlier theoretical results with optimized structural parameters for bulk anatase TiO_2.

Table 4. Optimized structural parameters for bulk anatase TiO_2 compared with experimental and previous theoretical results.

Lattice Parameter	EXPERIMENTAL [114]	THIS WORK		LITERATURE [113]	
		Results	Deviation (%)	Results	Deviation (%)
a (Å)	3.785	3.776	0.0088	3.743	0.042
b (Å)	3.785	3.776	0.0088	3.743	0.042
c (Å)	9.514	9.486	0.0294	9.481	0.031

The optimized structural parameters demonstrate that the computed results and other stated theoretical and experimental values are in good agreement [113]. The computed deviation from the experimental data is acceptable [112]. Figure 25 below illustrates the anatase TiO_2 surface (101) with a created supercell of 4 x 4 x 1 that has been cleaved from anatase TiO_2 bulk structure, while ending with both oxygen and titanium, the atoms on this surface have some cleaved bonds in the ending position. Atoms were relaxed to optimize the surfaces and remove surface tension. After cleaving, a supercell of 4 x 4 x 1 TiO_2 anatase of a surface (101) surface consists of 131 atoms. The color red represents oxygen, and the color grey represents titanium, and on an adsorbed structure of TiO_2/dye onto (101) surface of a created supercell of 4 x 4 x 1 consists of 156 atoms. This is due to the inclusion of a porphyrin dye molecule, with green color representing Magnesium, blue representing Nitrogen, and dark grey representing Carbon elements.

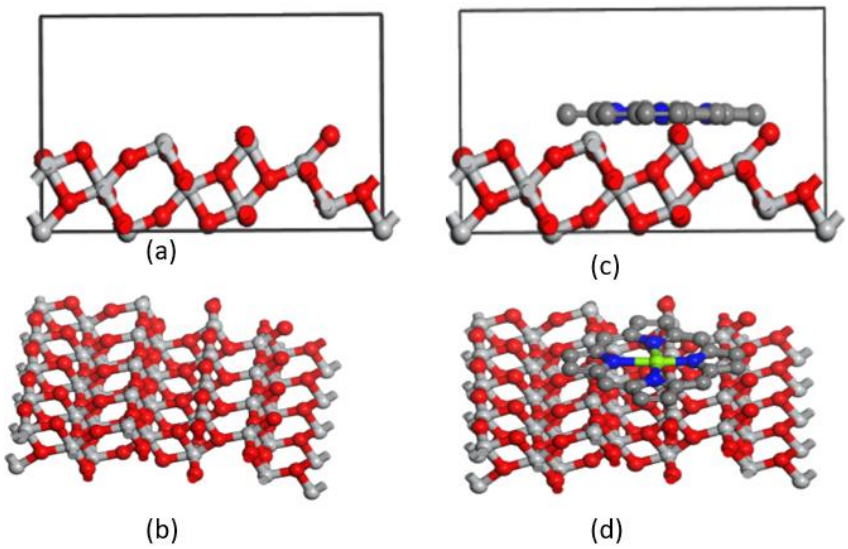

Figure 25., (a) side view a supercell surface of TiO_2 anatase, (b) top view of a supercell surface of TiO_2 anatase, (c) view of adsorption of porphyrin dye molecule and (d) top view of adsorption of porphyrin dye molecule onto 4 x 4 x 1 supercell of TiO_2.

4.4. Electronic optical properties

4.4.1. Band structures

The bulk structure's electronic properties are examined in this section. The Perdew-Burke-Ernzerhof (PBE) scheme was used to optimize the TiO_2 anatase bulk structure enabling the unit cell parameters and atoms to relax until the forces on all atoms converged [110]. Figure 26 illustrates that the band gap obtained for the bulk structure was 3.209 eV, which is not far from the anticipated experimental value of 3.2 eV for TiO_2 structure [115]. Since the internal structural parameters were relaxed with the GGA functional, which typically underestimates the band gap allowing the scissors operator of 1.108 eV to precisely determine the band gap. The operator of the scissors explains how the band gap differs between theoretical and experimental values. It is used to adjust the theoretical band gap so that it coincides with the experimental value [116].

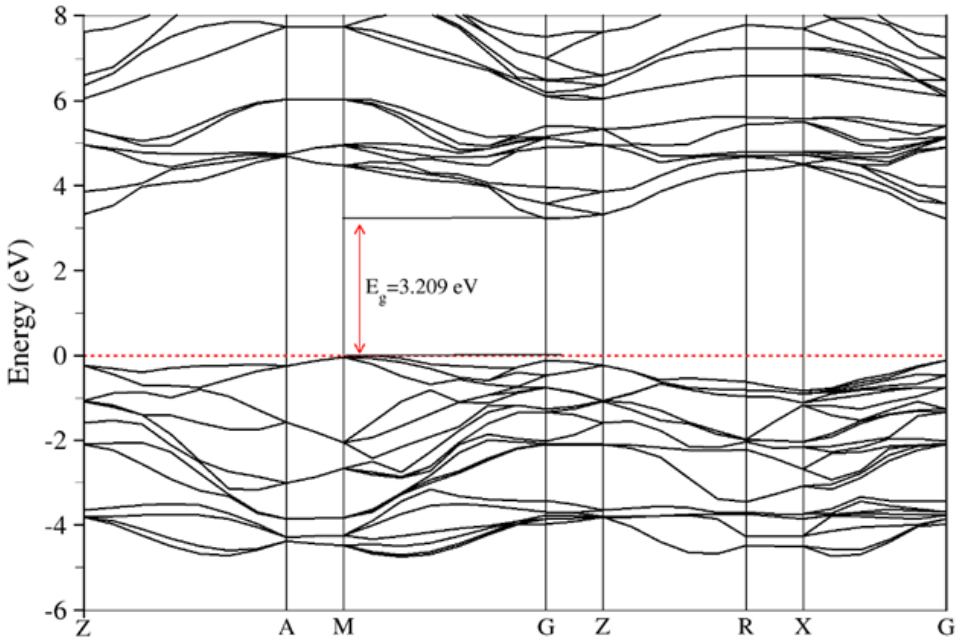

Figure 26. Band structure TiO_2 anatase bulk structure

To validate the method's correctness and establish the precise scissors operator for calculating optical characteristics [116], we first compute the energy band structure for the bulk structure of anatase TiO_2. This calculation's underestimated band gap of 2.092 eV for anatase was rectified by allowing the scissors operator of 1.108 eV, which strongly shifts the unoccupied CB band with respect to the entirely occupied VB band. To compensate for the experimental band gap of anatase (3.2 eV), the scissors operator 1.108 eV was chosen first hence the observed band gap on the Figure above is 3.2 eV, our results are comparable to the work done by Hosain *et al* [116 - 118]

The band structure of bulk Anatase TiO_2 was calculated and plotted in Figure 26, the symmetry points are shown by vertical lines, and the Fermi level of this crystal is represented by a zero on the energy scale on the band structure graph. There is a large band gap, which is the range of energies where there are no electronic states across the Brillouin zone. The Fermi level is found within the band gap, while the band below the level is completely occupied. Anatase TiO_2 has a valence band maximum (VBM) along M point and a conduction band minimum (CBM) at G point, as shown in Figure 26. Since the valence band maximum and conduction band minimum are on distinct

symmetry points, Anatase TiO_2 is an indirect band gap semiconductor with an energy gap value of 3.209 eV and this result corresponds well with the work done by Nura *et al* [118]. The underestimating of the band gap from experimental results, on the other hand, is mostly attributable to the fact that the exact functional in the Hohenberg-Kohn theorem is unknown. As a result, when compared to other theoretical values, the estimates for the exchange correlation accurately predict the band gap [118].

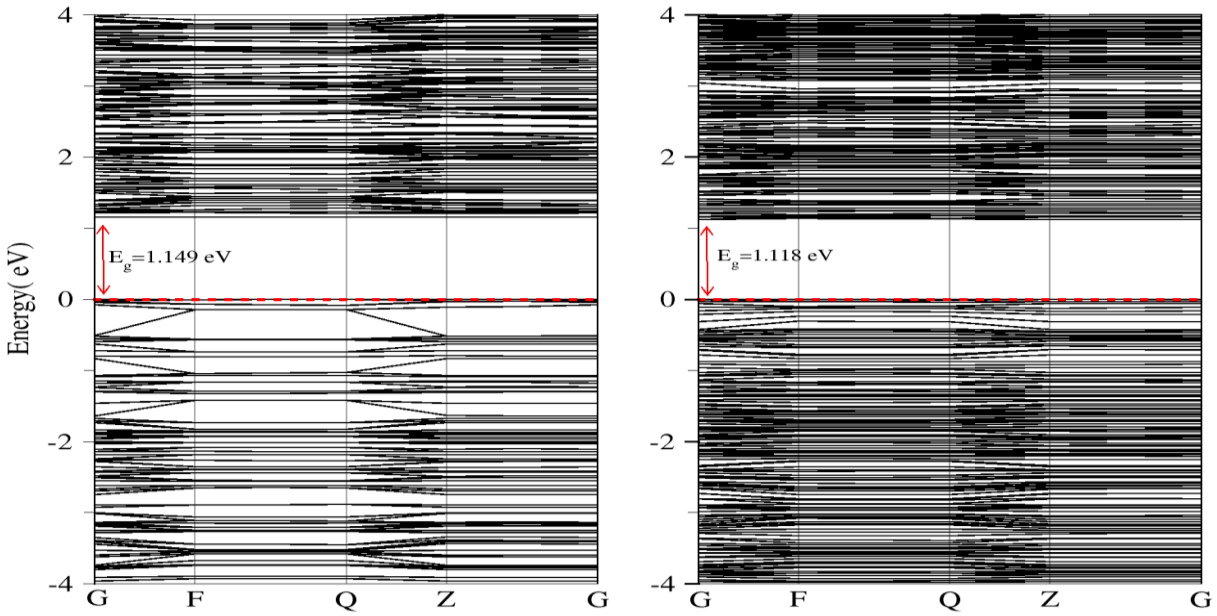

Figure 27. Band structure of supercell (4 x 4 x 1) of TiO_2 anatase on a (101) surface and band structure of adsorbed TiO_2/dye onto supercell (4 x 4 x 1) of TiO_2 anatase on a (101) surface respectively calculated using DFT.

Figure 27. illustrates the band structure of supercell (4 x 4 x 1) of TiO_2 anatase on a (101) surface and band structure of adsorbed TiO_2/dye onto supercell (4 x 4 x 1) of TiO_2 anatase on a (101) surface respectively calculated using DFT. The red dashed lines indicate the Fermi energy level. Transitioning of electrons between the valence and conduction bands must meet two requirements [118]: both energy and momentum must be conserved. Energy conservation is usually not an issue in a direct and indirect semiconductor [119,120]. The conservation of momentum for an electron transition between the maximum of the valence band and the minimum of the conduction band, cannot be fulfilled by the absorption or emission of a photon alone in an indirect

semiconductor, because the magnitude of a photon's momentum is several orders of magnitude smaller than that of an electron in a semiconductor [119-121]. The wave vectors of a photon and an electron in a crystal have the same enormous difference. As a result, the momenta or wave vectors can be compared. The energy bands in relation to the wave vector are determined using the Schrödinger equation and a periodic potential characteristic of certain semiconductors [119,120].

The computed band gap of TiO_2 anatase bulk structure is approximately 3.209 eV, which fits well with the experimental value of 3.2 eV due to band gap underestimate and the use of the scissor's operator by GGA functional used on the DFT. The computed band gap of cleaved surface TiO_2 anatase (101) with a 4 x 4 x 1 supercell is 1.149 eV, which is around 2.06 eV less than the calculated band gap of pure anatase TiO_2. And the computed band gap of the adsorbed TiO_2/dye is 1.118 eV which is around 2.091 eV less than the calculated band gap TiO_2 anatase bulk structure. The computed band gap of (101) surface structure is less than the band gap of the bulk structure; this difference in band gap of bulk structure and surface is due to re-orientation of atoms when structure is cleaved [122].

4.4.2. Density of states

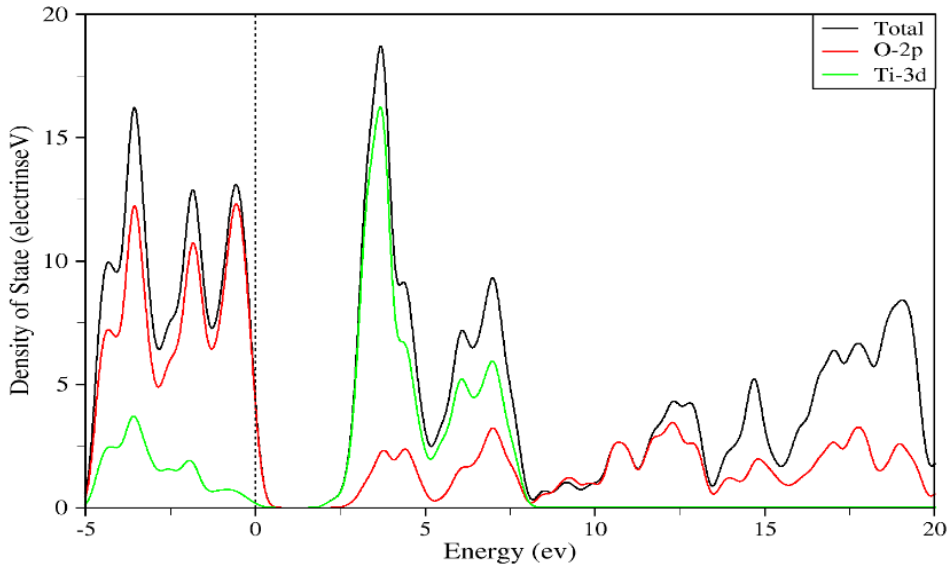

Figure 28. Partial Density of States of TiO_2 anatase bulk structure.

As illustrated in Figure 28, TiO_2 anatase bulk structure and (101) TiO_2 anatase surface have the state for electron occupation. TiO_2 anatase valence and conduction bands are primarily made up of O-2p and Ti-3d orbitals, respectively. The PDOS of the bulk structure and the surface are comparable because they are made up of the same atoms (oxygen and titanium). The valence band from -5 to 0 eV exhibits considerable hybridization between 2p and 3d states of Oxygen and Titanium electrons, but the conduction band from 0 to 4 eV is dominated by Ti-3d electrons, with a minor contribution from O-2p electrons. The electron transition from the valence to conduction band across the band gap involves both Ti-3d and O-2p states. and this work is consistent with the work done by Samat *et al* [123].

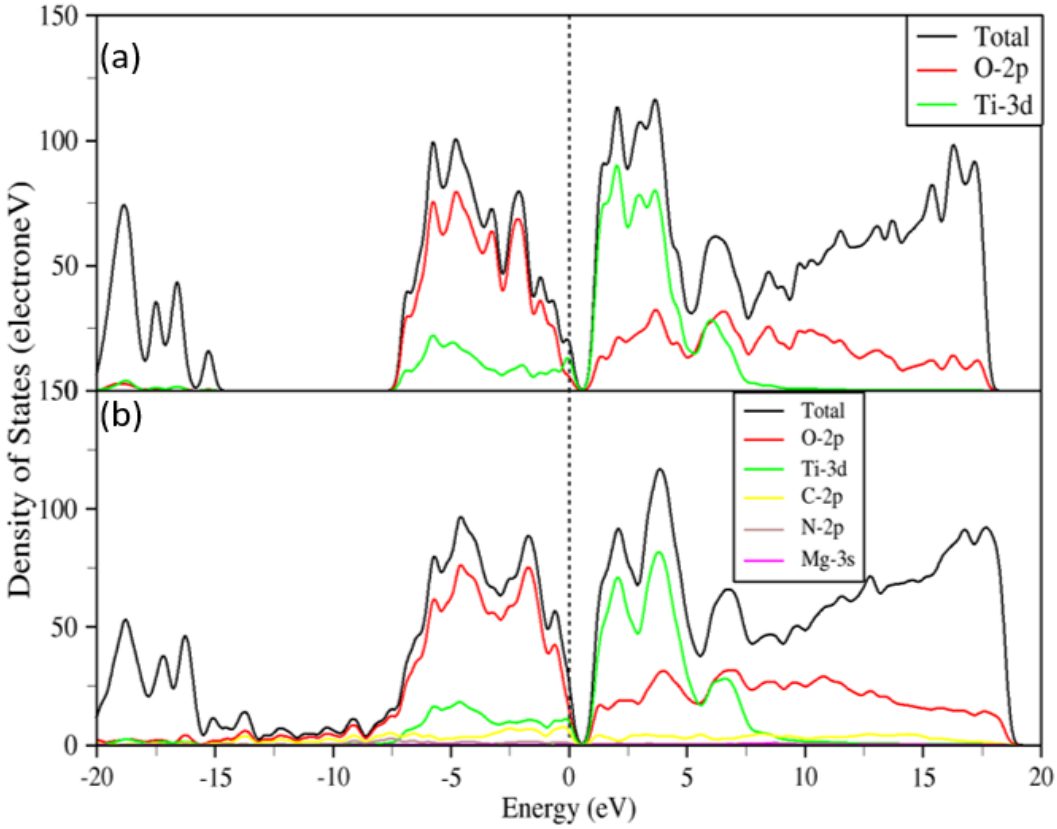

Figure 29. (a) Density of States of supercell (4 x 4 x 1) of TiO_2 anatase on a (101) surface and (b) Density of States of adsorbed TiO_2/dye onto supercell (4 x 4 x 1) of TiO2 anatase on a (101) surface respectively

The band gap is the distance between the valence and conduction bands. The gap between the valence and the conduction band on the PDOS of supercell (4 x 4 x 1) of TiO_2 anatase on a (101) surface and adsorbed TiO_2/dye onto supercell (4 x 4 x 1) of TiO_2 anatase on a (101) surface becomes slightly smaller than that of bulk TiO_2, indicating that electronic non-locality is more visible when crystal symmetry is reduced. The valence band is primarily composed of O-2p states, while Ti-3d states make up most of the conduction band in all structures. The density of states typically describes the number of available states per energy distance for each energy level that electrons can occupy. A high PDOS at a particular energy level indicates that there are many possible states for electron occupation, whereas a PDOS of O-2p indicates that there are no states that may be inhabited by electrons. The electron passes from a semiconductor's valence band to its conduction band; if there is no state for occupancy, the electron falls back, causing charge recombination between the valence and conduction bands.

As illustrated in Figure 29 (a), the valence band from -7.5 to 0 eV exhibits a significant hybridization at O-2p with a small contribution of Ti-3d electrons, whereas the conduction band from 0 to 5 eV is mostly contributed by Ti-3d with a small contribution of O-2p electrons. This demonstrates that electrons are moving from the valence to the conduction band across the band gap in both Ti 3d and O-2p states. Whereas Figure 29 (b) illustrates that when the dye molecule is adsorbed onto TiO_2, the valence band from -15 to -10 eV has a minor contribution from C-2p, N-2p, and Mg-3s. At -5 to 0 eV, however, a significant contribution of C-2p is observed. Similarly, a strong hybridization of O-p is found in the valence band from -7.5 to 0 eV in Figure 29 (a), with a small contribution of Ti-3d electrons, whereas the conduction band from 0 to 5 eV is mostly Ti-3d with a small contribution of O-2p and C-2p. Both Ti-3d, O-2p, C-2p, N-2p, and Mg-3s states are involved in electron transitioning from valence to conduction band across the band gap in Figure 29 (b) after the adsorption when the dye is adsorbed onto TiO_2, a slight electron transition from the valence to conduction band is observed in Figure 29 (b).

4.4.3. Optical reflectivity

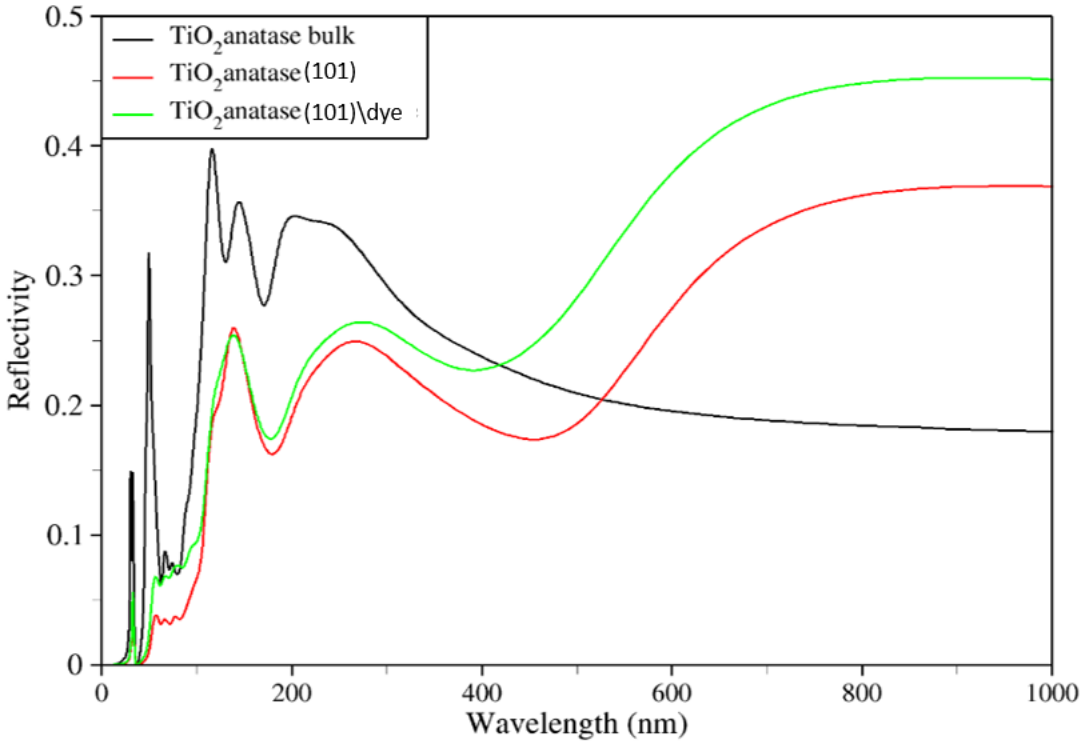

Figure 30. Optical reflectivity of TiO_2 anatase bulk, supercell (4 x 4 x 1) of TiO_2 anatase on a (101) surface and adsorbed TiO_2/dye onto supercell (4 x 4 x 1) of TiO_2 anatase on a (101) surface

Figure 30 indicates higher reflection of light in the visible region and higher reflection in the near infrared region only for supercell and TiO_2/dye complex, whereas the bulk TiO_2 structure displays a drop from 600 - 1000 nm of solar spectrum. The increased reflection of radiation in the near infrared range is due to atom re-orientation during cleaving of the structure [124]. As expected, the reflectivity for the bulk structure of the TiO_2 anatase curve is substantially higher in the ultra-visible region. And this work agrees well with the work previously done by Ranwaha *et al* [124] and Phuthu *et al* [125]

4.6.4. Optical Refractive Index

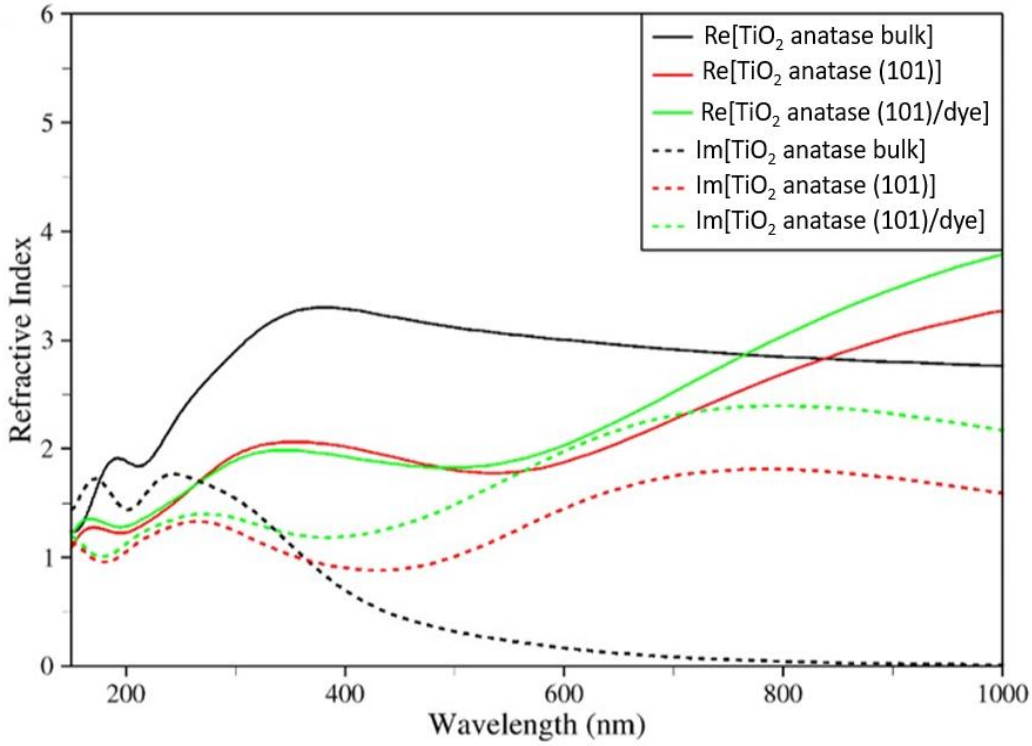

Figure 31. Optical refractive index of TiO_2 anatase bulk, supercell (4 x 4 x 1) of TiO_2 anatase on a (101) surface and adsorbed TiO_2/dye onto supercell (4 x 4 x 1) of TiO_2 anatase on a (101) surface

Figure 31 illustrates refractive index graphs for TiO_2 anatase bulk, supercell (4 x 4 x 1) of TiO_2 anatase on a (101) surface and TiO_2/dye complex. For bulk structure, the real refractive index part increases steadily in the visible region, while the imaginary refractive index part drops from 400 to 600 nm. For both supercell and adsorbed dye, the real refractive index displays a distinct absorption of photons or light from the visible to near-infrared region, whereas the imaginary refractive index exhibits less absorption. If the refractive index is high, light or photon absorption slows and tends to decrease. For both the imaginary refractive index of the bulk structure, supercell, and the adsorbed dye, we observed increased absorbance at 200-380 nm and lower absorbance at 400-1000 nm. However, the dye adsorbed on TiO_2 has a higher refractive index for both the real and imaginary graphs. This demonstrates that our dye

molecule adsorbed onto TiO_2 can improve solar spectrum absorption from visible to near infrared.

4.4.5. Optical dielectric function

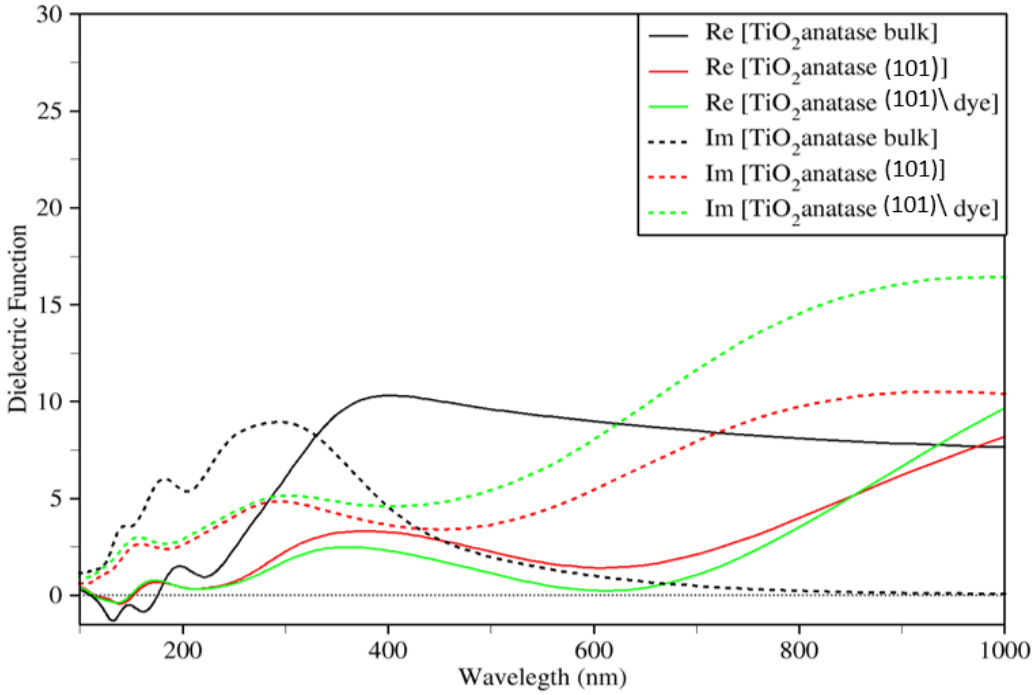

Figure 32. optical dielectric function of TiO_2 anatase bulk, supercell (4 x 4 x 1) of TiO_2 anatase on a (101) surface and adsorbed TiO_2/dye onto supercell (4 x 4 x 1) of TiO_2 anatase on a (101) surface

The real and imaginary parts are related to the material's electronic polarizability and electronic absorption, respectively. Figure 32 illustrates the computed dielectric functions of the anatase bulk structure, as well as the supercell of 4 x 4 x 1 and adsorbed dye molecule onto (101) surface. The anatase bulk structure exhibits high polarization and high absorption in the ultra-violet visible region and less absorption of the imaginary in the nearer infrared region. While the real and imaginary dielectric for a supercell as well as the adsorbed dye shows a higher absorption in both visible and nearer infrared region, which shows the imaginary dielectric function, demonstrating that the anatase bulk structure absorbs more photon only in the visible region of the spectrum. However, after 600 nm, the bulk TiO_2 imaginary displays a

decrease response of absorption, whereas the real parts of dielectric function for the bulk TiO_2 show an improved response in the near-infrared region, which increases light absorption.

4.4.6. Optical Absorption

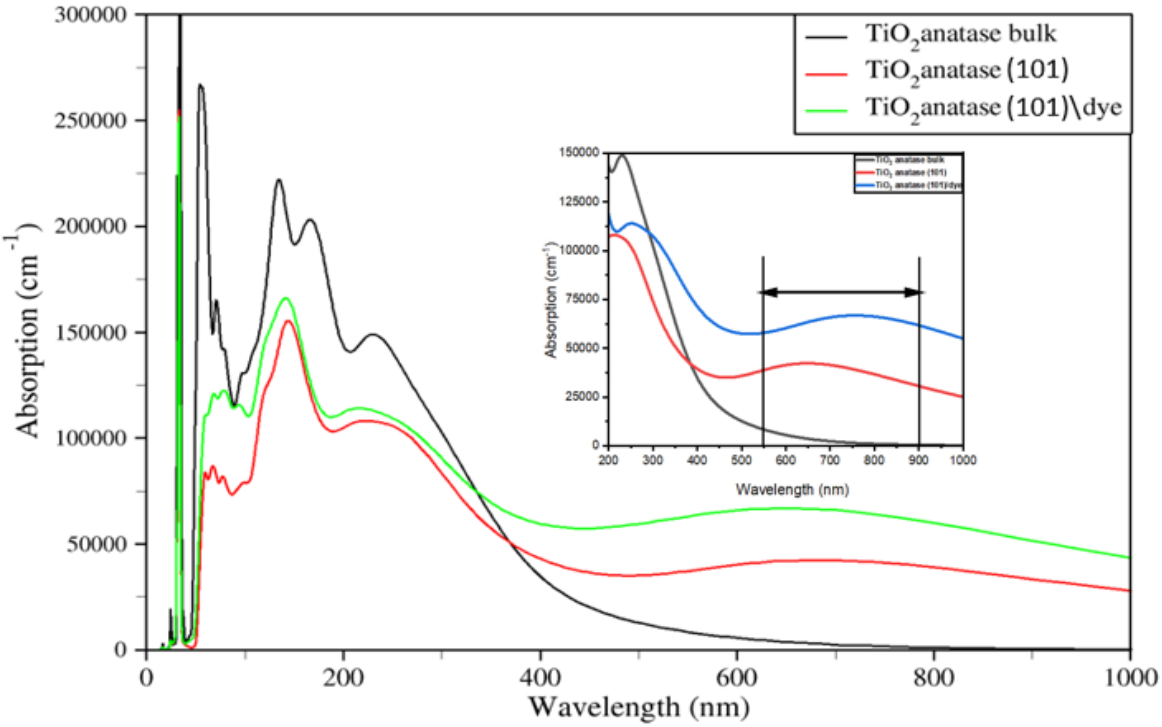

Figure 33. Optical absorption of TiO_2 anatase bulk, supercell (4 x 4 x 1) of TiO_2 anatase on a (101) surface and adsorbed TiO_2/dye onto supercell (4 x 4 x 1) of TiO_2 anatase on a (101) surface

The absorption coefficient defines how far light of a specific wavelength can penetrate before being absorbed. Three separate energy peaks of absorption spectra occur at similar peaks with part of the dielectric function and extinction coefficient. The optical absorption coefficients for the TiO_2 anatase bulk structure and supercell (4 x 4 x 1) of (101) anatase TiO_2 surfaces are compared in Figure 33. The optical band gap is experimentally determined by the excitation energy intercept at absorption edges in absorption spectra; the optical band gap differs significantly from the electronic band gap. The absorption graph displayed inside the original absorption graph is zoomed to

clearly show the absorption that occurs between 665 and 700 nm, which is consistent with the experimental absorption seen in Figures 11 and 12. Our computational findings match that of the experimental absorption. The electrical band gap is reasonable to assume a single particle, whereas optical absorption requires activation beyond a single particle.

The optical absorption of TiO_2 anatase bulk structure and supercell 4 x 4 x 1 of (101) anatase TiO_2 surfaces is shown in Figure 33, revealing that the bulk structure and surfaces can absorb photons in the ultra-violet and near infrared regions. because figure 33 shows photons with stronger peaks in the ultraviolet area of the solar spectrum and weaker peaks in the visible to near infrared range. However, when the dye is adsorbed onto TiO_2 anatase, substantial absorption in the near infrared range is seen. TiO_2 bulk anatase absorbs only in the ultra-visible and visible bands due to its bulk structure. Adsorption of dye molecules onto TiO_2 can improve the absorption coefficient of TiO_2/dye-based solar cells for renewable energy applications.

4.4.7. Optical Loss of function

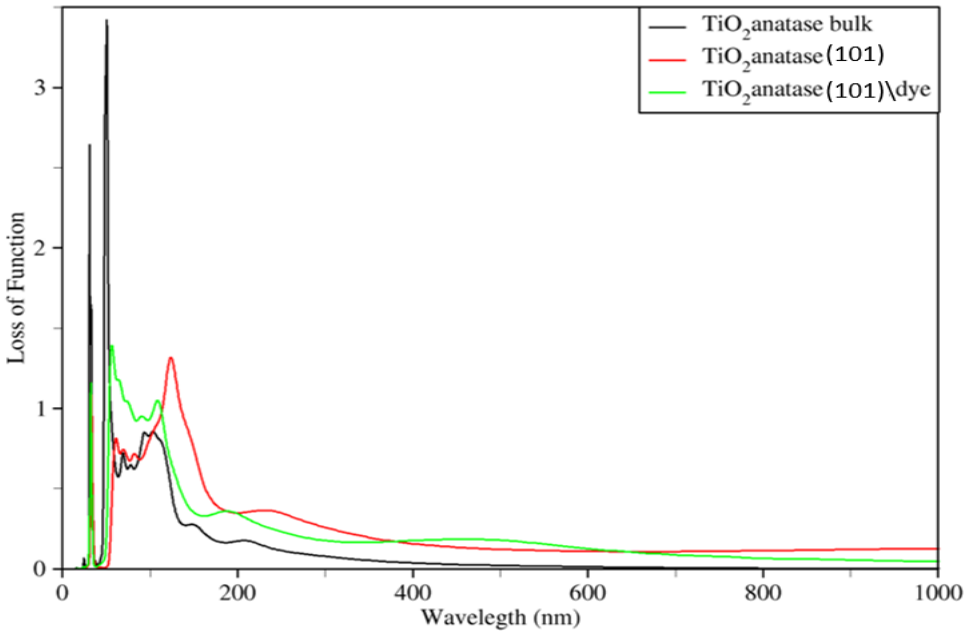

Figure 34. Optical loss of function of TiO_2 anatase bulk, supercell (4 x 4 x 1) of TiO_2 anatase on a (101) surface and adsorbed TiO_2/dye onto supercell (4 x 4 x 1) of TiO_2 anatase on a (101) surface

The loss function represents the energy loss of an electron as it passes through uniform dielectric materials. The largest peak of energy loss for anatase is located in the ultra-visible region, resulting in a greater energy loss only in the ultra-visible region.

4.5. TiO_2/dye Complex

TiO_2/dye complex formed when the dye molecule is adsorbed on the surface of TiO_2 which is known as an adsorbate, and the absorbing substance is known as an adsorbent. The adsorbate in this work is a porphyrin dye molecule, while the adsorbent is a supercell 4 x 4 x 1 of (101) surface of TiO_2 anatase. Figure 35 illustrates a porphyrin dye molecule absorbed on a supercell produced from (101) adsorbed onto TiO_2 anatase.

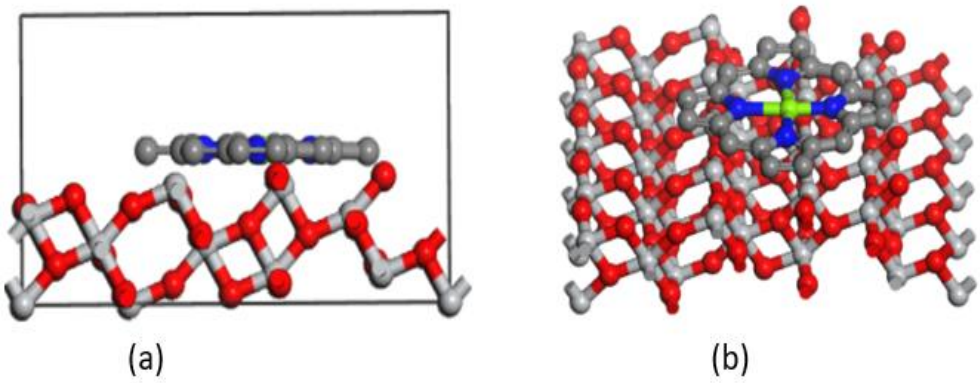

Figure 35. (a) side view of adsorption of porphyrin dye molecule and (b) top view of adsorption of porphyrin dye molecule onto 4 x 4 x 1 supercell of TiO_2 anatase of (101) surface

4.5.1. Electron Injection

After photoexcitation, electrons move from the photo-excited chromophore into the conduction band of the nanocrystalline semiconductor. This is an important part of how the cell works, and it can take from sub picoseconds to tens of picoseconds or even nanoseconds [127]. The short circuit current of a photovoltaic device is directly related to how well electrons are injected into the DSSC. Electrons in excited states after photoexcitation can easily lose the photon energy they have absorbed as heat if they are not quickly injected. This happens through electron-phonon scattering and the subsequent dissipation of phonons, which causes a loss in efficiency due to heat. So, it is especially important for further development of the nanoparticle-based device [12,128] to fully understand both the experimental and theoretical dynamics of electron transfer at the interface. The inject parameter shows the electron injection efficiency and is related to the driving force ΔG_{inject} of electrons moving from the excited states of dye molecules to the semiconductor substrate [121].

$$\Delta G_{inject} = E_{OX}^{dye*} - E_{CB}^{TiO2} \quad \text{..... (32)}$$

Where, E_{OX}^{dye*} is the excited state oxidation potential of the dye.E_{CB}^{TiO2} is the energy conduction band on the TiO_2 semiconductor (-4eV)

However, we can calculate the E_{OX}^{dye*} using,

$$E_{OX}^{dye*} = E_{OX}^{dye} - \lambda_{max}^{ICT} \quad \text{..... (33)}$$

λ_{max}^{ICT} is the maximum wavelength absorption for the lowest energy transitioning in the UV-Vis absorption spectrum of the dye molecule.

The performance of the DSSC improves as the electron injection quantum yield inject from the excited dye molecules to the conduction band of the semiconductor increases, provided that this electron injection process is followed by efficient regeneration of the oxidized dye molecules by the electrolyte, such as the I^{-1}/I^{3-} redox couple [129].

Table 5. Electron injection between the dye molecule and (101) TiO_2

Dye	E_{OX}^{dye}	λ_{max}^{ICT}	E_{CB}^{TiO2}	E_{OX}^{dye*}	ΔG_{inject}
Porphyrin	-3792.65	0.027	-4.00	-3792.68	-3788.68
Porphyrin-water	-3360.38	1.34	-4.00	-3361.72	-3357.72
Porphyrin-methanol	-33.56	1.11	-4.00	-3361.49	-3357.49
Porphyrin-ethanol	-3360.99	1.12	-4.00	3361.50	-3357.50

Table 5 illustrates the calculated values of electron injection, which show that E_{OX}^{dye} caused ΔG_{inject} to go down by a large amount. The negative values for ΔG_{inject} show that the dye molecule is transferring electrons to TiO_2 on its own, which is the required effective performance.

4.5.2. Adsorption Energy

The adsorption energy of TiO_2 /dye complex was calculated using the following equation (34).

$$E_{ads} = (E_{TiO_2} + E_{dye}) - E_{TiO_2/dye} \quad \text{..... (34)}$$

where E_{ads} is the adsorption energy of TiO_2/dye complex, E_{TiO_2} is the total energy of TiO_2 without adsorbed molecule, E_{dye} is the total energy of a dye molecule and E_{TiO_2}/dye is the total energy of TiO_2 with adsorbed molecule.

$E_{ads} = (E_{TiO2} + E_{dye}) – E_{TiO2/dye}$

$= [-1262.56 \text{ eV} + (-175.33 \text{ eV})] – (-1444.06 \text{ eV})$

$= 6.17 \text{ eV}$

The calculated adsorption energy shows a positive value, indicating that the TiO_2/dye surface complex is thermodynamically stable thus the dye binds strongly on the surface of $Ti0_2$ (101) anatase. The adsorption energy found in this study is comparable to the adsorption energy reported by Puyad *et al.* [44] when they reported the adsorption of croconate dye absorbed on anatase TiO_2 surface (101). The Figure below shows the isodensity of porphyrin dye molecule.

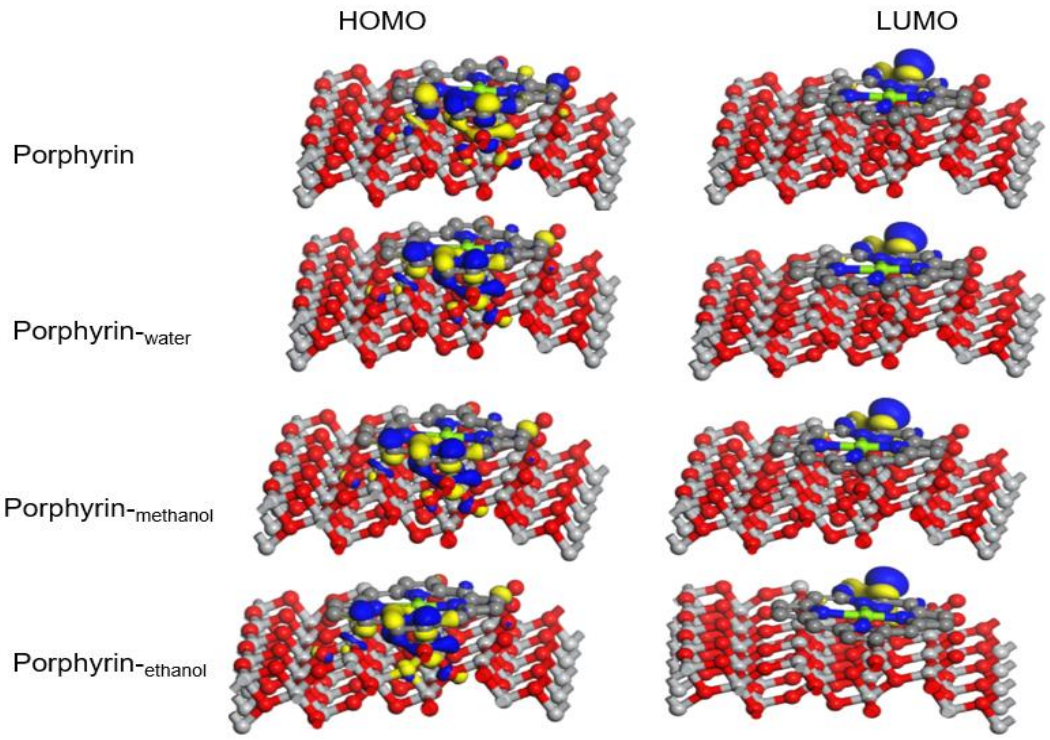

Figure 36. Isodensity of porphyrin molecule.

Figure 36 illustrates the HOMO and LUMO orbitals located on an adsorbed TiO_2/dye molecule and, the porphyrin ring serves as the core of the molecules' frontier orbitals. This has the impact of indicating that most electronic transitions, including absorption, emission, and charge transfer, will be regulated by the structure of the porphyrin ring as observed in Figure 36 [43,108].

CHAPTER 5

5.1. CONCLUSION

UV-Vis, FTIR, XRD, SEM, TEM and EDS were used to investigate the synthesis and characterization of TiO_2 NPs from *B. Pilosa* plant extracts. Experimentally, the chlorophyll pigment extracted from *B. pilosa* showed absorbance at 420 nm and 665 nm, whereas betalain pigment found in *B. pilosa*, showed absorbance at 536 nm. The absorbance at 600 nm - 665 nm is caused by the porphyrin and pheophytin molecules found in the chlorophyll pigment extracted from *B. pilosa*; these molecules showed the ability to absorb photons in both visible and near infrared regions of the spectrum. The absorbance of TiO_2 NPs synthesized with *B. pilosa* was similar to that of extracts, but with a decrease in absorbance at the same peaks. The decrease in absorbance indicates the possibility of chlorophyll adsorbed on the surface of TiO_2 nanoparticles and the formation of the chlorophyll-titanium oxide ground-state complex. The FTIR analysis identified the various functional groups found in a *B. pilosa* plant; natural dye extracted with functional groups such as (-OH) and (C=O) has a greater absorbance efficiency, and our *B. pilosa* contains similar functional groups. When observed under SEM and TEM, the TiO_2 NPs were heterogeneous in shape but spherical under SEM, indicating the development of paste in agglomeration. The XRD spectrum analysis revealed a collection of nine unique diffraction peaks matching crystalline TiO_2 NPs. In FTIR measurement, two strong peaks were identified about 1050 cm^{1} and 500 cm^{1}, which could be related to a peak in metal reduction.

The EDS spectrum data revealed a titanium dioxide signal at 99%, with other elements contributing equally to the remaining percentages of peaks. The XRD analysis identified the various peaks detected, with the strongest peak observed at (101) corresponding to TiO_2 anatase. Among the solvents used experimentally, the ethanol solvent has been shown to have a higher absorbance followed by methanol and water, computationally the two molecules absorbed photons in both visible and nearer infrared regions at a lower absorbance. However, with the effects of solvents, the porphyrin molecule blue-shifted to the visible region of the spectrum with a higher absorbance. Similarly, the pheophytin molecule with the effects of solvents blue-shifted to the visible region with a higher absorbance. Among the solvents used in both experimental and computational

ethanol shows a higher absorbance followed by methanol and water. Hence, the best solvent that can be used in extracting and absorbing a dye should be methanol.

Furthermore, DFT was successfully applied to study the adsorption of porphyrin dye on the (101) surface of TiO_2 anatase, GGA was used in the scheme to describe the Exchange Correlation Function of the system, and calculations were performed using VAMP and CASTEP code as implemented in Material Studio. The UV-Vis absorption spectrum shows that the porphyrin dye molecule exhibits a broader adsorption capacity, indicating its absorption ability in a wider energy range from the visible to the near-infrared region of the spectrum. The optical absorption of the adsorbed dye shows a broad absorption behavior of the visible and near infrared region, which demonstrates that by adsorbing the porphyrin dye onto the anatase TiO_2 semiconductor, the absorption of photon receptor will be shifted by ultraviolet rays toward the visible infrared region and closer to the nearer infrared region.

The frontier orbitals of HOMO and LUMO on a porphyrin dye molecule before adsorbed and after adsorbed onto TiO_2, the frontier orbitals of the molecules were centered on the porphyrin ring for both water, methanol, and ethanol solvents on a porphyrin molecule. This gives a consequence that the structure of porphyrin ring is responsible for most of the electronic transition involved such as absorption, emission, and charge transfer. The Electron injection between the dye molecule and (101) TiO_2 resulted in ΔG_{inject} to decrease by a large amount. The negative values for ΔG_{inject} shows that the dye molecule is transferring electrons to TiO_2 on its own, which effectively may increase performance of DSSCs and increase the absorption of the dye. The electron injection is related to the driving force ΔG_{inject} and the adsorption energy between the porphyrin dye molecule, the results show a spontaneous electron injection and the adsorption energy obtain shows that the complexes are stable and has a strong binding ability of dye molecule to the TiO_2 anatase (101) surface.

REFERENCE

[1] Hamann, T. W., Jensen, R. A., Martinson, A. B., Van Ryswyk, H., & Hupp, J. T. (2008). Advancing beyond current generation dye-sensitized solar cells. Energy & Environmental Science, 1(1), 66-78.

[2] Mahlangu, N., & Thopil, G. A. (2018). Life cycle analysis of external costs of a parabolic trough Concentrated Solar Power plant. Journal of cleaner production, 195, 32-43.

[3] Trollip, H., Butler, A., Burton, J., Caetano, T., & Godinho, C. (2014). Energy Security in South Africa.

[4] Fthenakis, V. M., Alsema, E. A., & de Wild-Scholten, M. J. (2005, January). Life cycle assessment of photovoltaics: perceptions, needs, and challenges. In Conference Record of the Thirty-first IEEE Photovoltaic Specialists Conference,1655-1658.

[5] Stages, L. C. (2012). Life cycle greenhouse gas emissions from solar photovoltaics. J. Ind. Ecol.

[6] Fthenakis, V. M., Kim, H. C., & Alsema, E. (2008). Emissions from photovoltaic life cycles. Environmental science & technology, 42(6), 2168-2174.

[7] Kalyanasundaram, K., & Grätzel, M. (2009). Efficient dye-sensitized solar cells for direct mconversion of sunlight to electricity. Material Matters, 4(4), 88-90.

[8] Philipps, S., & Warmuth, W. (2019). Photovoltaics report fraunhofer institute for solar energy systems. ISE with Support of PSE GmbH November 14th; Fraunhofer ISE: Freiburg, Germany.

[9] Brown, G. F., & Wu, J. (2009). Third generation photovoltaics. Laser & Photonics Reviews, 3(4), 394-405.

[10] Celik, I., Song, Z., Cimaroli, A. J., Yan, Y., Heben, M. J., & Apul, D. (2016). Life Cycle Assessment (LCA) of perovskite PV cells projected from lab to fab. Solar Energy Materials and Solar Cells, 156, 157-169.

[11] Baxter, J. B., & Aydil, E. S. (2006). Dye-sensitized solar cells based on semiconductor morphologies with ZnO nanowires. Solar Energy Materials and Solar Cells, 90(5), 607-622.

[12] Grätzel, M. (2003). Dye-sensitized solar cells. Journal of photochemistry and photobiology C: Photochemistry Reviews, 4(2), 145-153.

[13] Li, N., Pan, N., Li, D., & Lin, S. (2013). Natural dye-sensitized solar cells based on highly ordered TiO_2 nanotube arrays. International Journal of Photoenergy, 2013.

[14] Ali, R. A. M., & Nayan, N. (2010). Fabrication and analysis of dye-sensitized solar cell using natural dye extracted from dragon fruit. International Journal of Integrated Engineering, 2(3).

[15] Syafinar, R., Gomesh, N., Irwanto, M., Fareq, M., & Irwan, Y. M. (2015). Chlorophyll pigments as nature based dye for dye-sensitized solar cell (DSSC). Energy Procedia, 79, 896-902.

[16] Yang, H., Li, J., Zhou, G., Chiang, S. W., Du, H., Gan, L., ... & Duan, W. (2015). First principles study of ruthenium (II) sensitizer adsorption on anatase TiO_2 (001) surface. RSC advances, 5(74), 60230-60236.

[17] Sawhney, N., Raghav, A., & Satapathi, S. (2016). Utilization of naturally occurring dyes as sensitizers in dye sensitized solar cells. IEEE Journal of Photovoltaics, 7(2), 539-544.

[18] Yella, A., Lee, H. W., Tsao, H. N., Yi, C., Chandiran, A. K., Nazeeruddin, M. K., ... & Grätzel, M. (2011). Porphyrin-sensitized solar cells with cobalt (II/III)–based redox electrolyte exceed 12 percent efficiency. science, 334(6056), 629-634.

[19] Campbell, W. M., Burrell, A. K., Officer, D. L., & Jolley, K. W. (2004). Porphyrins as light harvesters in the dye sensitized TiO_2 solar cell. Coordination Chemistry Reviews, 248(13-14), 1363-1379.

[20] Chang, H., & Lo, Y. J. (2010). Pomegranate leaves and mulberry fruit as natural sensitizers for dye-sensitized solar cells. Solar energy, 84(10), 1833-1837.

[21] Abdel-Latif, M. S., El-Agez, T. M., Taya, S. A., Batniji, A. Y., & El-Ghamri, H. S. (2013). Plant seeds-based dye-sensitized solar cells.

[22] Nan, H., Shen, H. P., Wang, G., Xie, S. D., Yang, G. J., & Lin, H. (2017). Studies on the optical and photoelectric properties of anthocyanin and chlorophyll as natural co-sensitizers in dye sensitized solar cell. Optical Materials, 73, 172-178.

[23] Sharma, S., Uttam, R., & Uttam, K. N. (2020). Interaction of chlorophyll with titanium dioxide and iron oxide nanoparticles: A temperature dependent fluorescence quenching study. Analytical Letters, 53(12), 1851-1870.

[24] Ananthi, N., Subathra, M. S. P., Emmanuel, S. C., & Kumar, N. M. (2020). Preparation and characterization of two dye-sensitized solar cells using Acalypha Godseffia and Epipremnum Aureum dyes as sensitizers. Energy Sources, Part A: Recovery, Utilization, and Environmental Effects, 42(13), 1662-1673.

[25] Alhamed, M., Issa, A. S., & Doubal, A. W. (2012). Studying of natural dyes properties as photosensitizer for dye sensitized solar cells (DSSC). Journal of electron Devices, 16(11), 1370-1383.

[26] Kalyanasundaram, K., & Grätzel, M. (2009). Efficient dye-sensitized solar cells for direct conversion of sunlight to electricity. Material Matters, 4(4), 88-90.

[27] Wongcharee, K., Meeyoo, V., & Chavadej, S. (2007). Dye-sensitized solar cell using natural dyes extracted from rosella and blue pea flowers. Solar Energy Materials and Solar Cells, 91(7), 566-571.

[28] Gould, K., Davies, K. M., & Winefield, C. (Eds.). (2008). Anthocyanins: biosynthesis, functions, and applications. Springer Science & Business Media.

[29] Adedokun, O., Titilope, K., & Awodugba, A. O. (2016). Review on natural dye-sensitized solar cells (DSSCs). International Journal of Engineering Technologies IJET, 2(2), 34-41.

[30] Krishnan, S., & Shriwastav, A. (2021). Application of TiO_2 nanoparticles sensitized with natural chlorophyll pigments as catalyst for visible light photocatalytic degradation of methylene blue. Journal of Environmental Chemical Engineering, 9(1), 104699.

[31] Roy, M. S., Balraju, P., Kumar, M., & Sharma, G. D. (2008). Dye-sensitized solar cell based on Rose Bengal dye and nanocrystalline TiO_2. Solar Energy Materials and Solar Cells, 92(8), 909-913.

[32] Tomar, N., Agrawal, A., Dhaka, V. S., & Surolia, P. K. (2020). Ruthenium complexes-based dye-sensitized solar cells: Fundamentals and research trends. Solar Energy, 207, 59-76.

[33] Monari, A., Assfeld, X., Beley, M., & Gros, P. C. (2011). Theoretical study of new ruthenium-based dyes for dye-sensitized solar cells. The Journal of Physical Chemistry A, 115(15), 3596-3603.

[34] Campbell, W. M., Jolley, K. W., Wagner, P., Wagner, K., Walsh, P. J., Gordon, K. C., ... & Officer, D. L. (2007). Highly efficient porphyrin sensitizers for dye-sensitized solar cells. The Journal of Physical Chemistry C, 111(32), 11760-11762

[35] Bevilaqua, R. C., Zanella, I., & Fagan, S. B. (2010). Chlorophyll **a** and pheophytin **a** as gas sensors of CO_2 and O_2 molecules. Chemical Physics Letters, 496(4-6), 310-315.

[36] Birel, Ö., Nadeem, S., & Duman, H. (2017). Porphyrin-based dye-sensitized solar cells (DSSCs): a review. Journal of fluorescence, 27, 1075-1085.

[37] Prushan, M. (2005). Absorption and Fluorescence Spectroscopy of Tetraphenylporphyrin and Metallo-Tetraphenylporphyrin.

[38] Hao, S., Wu, J., Huang, Y., & Lin, J. (2006). Natural dyes as photosensitizers for dye-sensitized solar cell. Solar energy, 80(2), 209-214.

[39] Torchani, A., Saadaoui, S., Gharbi, R., & Fathallah, M. (2015). Sensitized solar cells based on natural dyes. Current Applied Physics, 15(3), 307-312.

[40] Mikroyannidis, J. A., Charalambidis, G., Coutsolelos, A. G., Balraju, P., & Sharma, G. D. (2011). Novel zinc porphyrin with phenylenevinylene meso-substituents: synthesis and application in dye-sensitized solar cells. Journal of Power Sources, 196(15), 6622-6628.

[41] Sharma, G. D., Angaridis, P. A., Pipou, S., Zervaki, G. E., Nikolaou, V., Misra, R., & Coutsolelos, A. G. (2015). Efficient co-sensitization of dye-sensitized solar cells by novel porphyrin/triazine dye and tertiary aryl-amine organic dye. Organic Electronics, 25, 295-307.

[42] Shanmugam, V., Manoharan, S., Sharafali, A., Anandan, S., & Murugan, R. (2015). Green grasses as light harvesters in dye sensitized solar cells. Spectrochimica Acta Part A: Molecular and Biomolecular Spectroscopy, 135, 947-952.

[43] Suendo, V., & Viridi, S. (2011). Ab initio calculation of UV-Vis absorption spectra of a single molecule chlorophyll a: Comparison study between RHF/CIS, TDDFT, and semi-empirical methods. arXiv preprint arXiv:1105.3766.

[44] Puyad, A. L., Kumar, C. R., & Bhanuprakash, K. (2012). Adsorption of croconate dyes on TiO_2 anatase (101) surface: A periodic DFT study to understand the binding of diketo groups#. Journal of chemical sciences, 124, 301-310.

[45] Martsinovich, N., Jones, D. R., & Troisi, A. (2010). Electronic structure of TiO_2 surfaces and effect of molecular adsorbates using different DFT implementations. The Journal of Physical Chemistry C, 114(51), 22659-22670.

[46] Bartolome, A. P., Villaseñor, I. M., & Yang, W. C. (2013). Bidens pilosa L.(Asteraceae): botanical properties, traditional uses, phytochemistry, and pharmacology. Evidence-based complementary and alternative medicine, 2013.

[47] Pawar, M., Topcu Sendoğdular, S., & Gouma, P. (2018). A brief overview of TiO_2 photocatalyst for organic dye remediation: case study of reaction mechanisms involved in Ce-TiO_2 photocatalysts system. Journal of Nanomaterials, 2018.

[48] Dayal, S., Kopidakis, N., Olson, D. C., Ginley, D. S., & Rumbles, G. (2010). Photovoltaic devices with a low band gap polymer and CdSe nanostructures exceeding 3% efficiency. Nano letters, 10(1), 239-242.

[49] AP Ribeiro, R., R de Lazaro, S., & R de Oliveira, C. (2016). Band-Gap engineering for photocatalytic applications: Anionic and cationic doping of TiO_2 anatase. Current Physical Chemistry, 6(1), 22-27.

[50] Lian, Y. (2022). Semiconductor Microchips and Fabrication: A Practical Guide to Theory and Manufacturing. John Wiley & Sons.

[51] Pramono, S. H., Maulana, E., Prayogo, A. F., & Djatmika, R. (2015). Characterization of dye-sensitized solar cell (DSSC) based on chlorophyll dye. International Journal of Applied Engineering Research, 10(1), 193-205.

[52] Li, Y., Li, H., Song, P., & Sun, C. (2015). Photoactive layer of DSSCS based on natural dyes: a study of experiment and theory. Journal of Nanomaterials, 2015, 1-1.

[53] Milenković, S. M., Zvezdanović, J. B., Anđelković, T. D., & Marković, D. Z. (2012). The identification of chlorophyll and its derivatives in the pigment mixtures: HPLC-chromatography, visible and mass spectroscopy studies. Adv. Technol, 1(1), 16-24.

[54] Holt, A. S., & Jacobs, E. E. (1955). Infra-red absorption spectra of chlorophylls and derivatives. Plant physiology, 30(6), 553.

[55] Arifin, Z., Soeparman, S., Widhiyanuriyawan, D., Suyitno, S., & Setyaji, A. T. (2018). Improving stability of chlorophyll as natural dye for dye-sensitized solar cells. Jurnal Teknologi, 80(1).

[56] Cerda, B., Sivakumar, R., & Paulraj, M. (2016, May). Natural dyes as sensitizers to increase the efficiency in sensitized solar cells. In Journal of Physics: Conference Series (Vol. 720, No. 1, p. 012030).

[57] Ramanarayanan, R., Nijisha, P., Niveditha, C. V., & Sindhu, S. (2017). Natural dyes from red amaranth leaves as light-harvesting pigments for dye-sensitized solar cells. Materials research bulletin, 90, 156-161.

[58] Oprea, C. I., Panait, P., Lungu, J., Stamate, D., Dumbravă, A., Cimpoesu, F., & Gîrţu, M. A. (2013). DFT study of binding and electron transfer from a metal-free dye with carboxyl, hydroxyl, and sulfonic anchors to a titanium dioxide nanocluster. International Journal of Photoenergy, 2013.

[59] Meng, S., Ren, J., & Kaxiras, E. (2008). Natural dyes adsorbed on TiO_2 nanowire for photovoltaic applications: enhanced light absorption and ultrafast electron injection. Nano letters, 8(10), 3266-3272.

[60] Niu, M. (2017). The Adsorption Geometry and Electronic Structure of Organic Dye Molecule on TiO_2 (101) Surface from First Principles Calculations. In MATEC Web of Conferences (Vol. 88, p. 03002). EDP Sciences.

[61] Jang, I., Song, K., Park, J. H., & Oh, S. G. (2013). Enhancement of dye adsorption on TiO_2 surface through hydroxylation process for dye-sensitized solar cells. Bulletin of the Korean Chemical Society, 34(10), 2883-2888.

[62] Mosconi, E., Selloni, A., & De Angelis, F. (2012). Solvent effects on the adsorption geometry and electronic structure of dye-sensitized TiO_2: a first-principles investigation. The Journal of Physical Chemistry C, 116(9), 5932-5940.

[63] Adedokun, O., Sanusi, Y. K., & Awodugba, A. O. (2018). Solvent dependent natural dye extraction and its sensitization effect for dye sensitized solar cells. Optik, 174, 497-507.

[64] Jin, X., Li, D., Sun, L., Wang, C. L., & Bai, F. Q. (2018). Theoretical design of porphyrin sensitizers with different acceptors for application in dye-sensitized solar cells. RSC advances, 8(35), 19804-19810.

[65] Ananthi, N., Subathra, M. S. P., Emmanuel, S. C., & Kumar, N. M. (2020). Preparation and characterization of two dye-sensitized solar cells using Acalypha Godseffia and Epipremnum Aureum dyes as sensitizers. Energy Sources, Part A: Recovery, Utilization, and Environmental Effects, 42(13), 1662-1673.

[66] Rahmatika, Z. (2021, February). Theoretical Modification of Pheophytin Using Cu, Ni, and Zn Atoms as a Sensitizer for Dye Sentized Solar Cell (DSSC). In Journal of Physics: Conference Series (Vol. 1788, No. 1, p. 012006). IOP Publishing.

[67] Yadav, V., Negi, C. M. S., Kumar, D. K., & Gupta, S. K. (2021). Fabrication of eco-friendly, low-cost dye sensitized solar cells using harda fruit-based natural dye. Optical Materials, 122, 111800.

[68] Nabi, G., Raza, W., & Tahir, M. B. (2020). Green synthesis of TiO_2 nanoparticle using cinnamon powder extract and the study of optical properties. Journal of Inorganic and Organometallic Polymers and Materials, 30, 1425-1429.

[69] Sethy, N. K., Arif, Z., Mishra, P. K., & Kumar, P. (2020). Green synthesis of TiO_2 nanoparticles from Syzygium cumini extract for photo-catalytic removal of lead (Pb) in explosive industrial wastewater. Green Processing and Synthesis, 9(1), 171-181.

[70] Subhapriya, S., & Gomathipriya, P. (2018). Green synthesis of titanium dioxide (TiO_2) nanoparticles by Trigonella foenum-graecum extract and its antimicrobial properties. Microbial pathogenesis, 116, 215-220.

[71] Ahmad, W., Jaiswal, K. K., & Soni, S. (2020). Green synthesis of titanium dioxide (TiO_2) nanoparticles by using Mentha arvensis leaves extract and its antimicrobial properties. Inorganic and Nano-Metal Chemistry, 50(10), 1032-1038.

[72] Mohanta, D. (2017). A Detailed Study on Optical and Physical Properties of Rice and its BY-Products. Unpublished, Tezpur University.

[73] Gremlich, H. U. (2000). Infrared and Raman spectroscopy. In Analytical Techniques in Combinatorial Chemistry (pp. 77-88). CRC Press.

[74] Nellist, P. D. (2019). Scanning transmission electron microscopy. Springer Handbook of Microscopy, 49-99.

[75] Bunaciu, A. A., UdriŞTioiu, E. G., & Aboul-Enein, H. Y. (2015). X-ray diffraction: instrumentation and applications. Critical reviews in analytical chemistry, 45(4), 289-299.

[76] Kohn, W., & Sham, L. J. (1965). Self-consistent equations including exchange and correlation effects. Physical review, 140(4A), A1133.

[77] Krieger, J. B., Li, Y., & Iafrate, G. J. (1992). Accurate local spin-polarized exchange potential: Reconciliation of generalized Slater and Kohn–Sham methods. International journal of quantum chemistry, 41(3), 489-496.

[78] Brink, D. M. (2002). Density functional theory. Nuclear Physics News, 12(4), 27-32.

[79] Payne, M. C., Teter, M. P., Allan, D. C., Arias, T. A., & Joannopoulos, A. J. (1992). Iterative minimization techniques for ab initio total-energy calculations: molecular dynamics and conjugate gradients. Reviews of modern physics, 64(4), 1045.

[80] Riess, J., & Münch, W. (1981). The theorem of Hohenberg and Kohn for subdomains of a quantum system. Theoretica chimica acta, 58, 295-300.

[81] Oliveira, A. F., Seifert, G., Heine, T., & Duarte, H. A. (2009). Density-functional based tight-binding: an approximate DFT method. Journal of the Brazilian Chemical Society, 20, 1193-1205.

[82] Ditchfield, R. H. W. J., Hehre, W. J., & Pople, J. A. (1971). Self-consistent molecular-orbital methods. IX. An extended Gaussian-type basis for molecular-orbital studies of organic molecules. The Journal of Chemical Physics, 54(2), 724-728.

[83] Stan, A., Dahlen, N. E., & Van Leeuwen, R. (2009). Levels of self-consistency in the GW approximation. The Journal of chemical physics, 130(11), 114105.

[84] Kurth, S., Marques, M., Lüders, M., & Gross, E. K. U. (1999). Local density approximation for superconductors. Physical review letters, 83(13), 2628.

[85] Vanderbilt, D. (1990). Soft self-consistent pseudopotentials in a generalized eigenvalue formalism. Physical Review B, 41(11), 7892

[86] Bachelet, G. B., Hamann, D. R., & Schlüter, M. (1982). Pseudopotentials that work: From H to Pu. Physical Review B, 26(8), 4199.

[87] Bartolotti, L. J., & Flurchick, K. (2009). An introduction to density functional theory. Reviews in computational chemistry, 7, 187-216.

[88] Kresse, G., & Joubert, D. (1999). From ultrasoft pseudopotentials to the projector augmented-wave method. Physical review b, 59(3), 1758.

[89] Yates, J. R., Pickard, C. J., & Mauri, F. (2007). Calculation of NMR chemical shifts for extended systems using ultrasoft pseudopotentials. Physical Review B, 76(2), 024401.

[90] Xiao, Z. Y., Li, Y. F., Yao, B., Deng, R., Ding, Z. H., Wu, T., ... & Zhao, H. F. (2013). Bandgap engineering of Cu2CdxZn1− xSnS4 alloy for photovoltaic applications: a complementary experimental and first-principles study. Journal of Applied Physics, 114(18), 183506.

[91] Schwerdtfeger, P. (2011). The pseudopotential approximation in electronic structure theory. ChemPhysChem, 12(17), 3143-3155.

[92] Car, R., de Angelis, F., Giannozzi, P., & Marzari, N. (2005). First-principles molecular dynamics. In Handbook of Materials Modeling (pp. 59-76).

[93] Eder, M., Hafner, J., & Moroni, E. G. (2000). Structural, electronic, and magnetic properties of thin Mn/Cu (100) films. Physical Review B, 61(17), 11492.

[94] Clark, S. J., Segall, M. D., Pickard, C. J., Hasnip, P. J., Probert, M. I., Refson, K., & Payne, M. C. (2005). First principles methods using CASTEP. Zeitschrift für kristallographie-crystalline materials, 220(5-6), 567-570.

[95] Al-Alwani, M. A., Mohamad, A. B., Kadhum, A. A. H., & Ludin, N. A. (2015). Effect of solvents on the extraction of natural pigments and adsorption onto TiO_2 for dye-sensitized solar cell applications. Spectrochimica Acta Part A: Molecular and Biomolecular Spectroscopy, 138, 130-137.

[96] Dima, R. S., Phuthu, L., Maluta, N. E., Kirui, J. K., & Maphanga, R. R. (2021). Electronic, structural, and optical properties of mono-doped and Co-Doped (210) TiO_2 brookite surfaces for application in dye-sensitized solar cells—a first principles study. Materials, 14(14), 3918.

[97] Elegbeleye, I. F., Maluta, N. E., & Maphanga, R. R. (2021). Density Functional Theory Study of Optical and Electronic Properties of $(TiO_2)_{n=\ 5,\ 8,\ 68}$ Clusters for Application in Solar Cells. Molecules, 26(4), 955.

[98] Ahmad, W., Jaiswal, K. K., & Soni, S. (2020). Green synthesis of titanium dioxide (TiO_2) nanoparticles by using Mentha arvensis leaves extract and its antimicrobial properties. Inorganic and Nano-Metal Chemistry, 50(10), 1032-1038.

[99] Wuryanti, S. (2021). The performance of solar cells using chlorophyll dye from Syzygium paniculatum. Clean Energy, 5(3), 433-440.

[100] Zhou, C. H., Xu, S., Yang, Y., Yang, B. C., Hu, H., Quan, Z. C., ... & Zhao, X. Z. (2011). Titanium dioxide sols synthesized by hydrothermal methods using tetrabutyl titanate as starting material and the application in dye sensitized solar cells. Electrochimica Acta, 56(11), 4308-4314.

[101] Lamiel-Garcia, O., Tosoni, S., & Illas, F. (2014). Relative stability of F-covered TiO_2 anatase (101) and (001) surfaces from periodic DFT calculations and ab initio atomistic thermodynamics. The Journal of Physical Chemistry C, 118(25), 13667-13673.

[102] National Center for Biotechnology Information (2023). PubChem Compound Summary for CID 66868, Porphyrin.

[103] Klimov, V. V. (2003). Discovery of pheophytin function in the photosynthetic energy conversion as the primary electron acceptor of Photosystem II. Photosynthesis research, 76, 247-253.

[104] Xu, Z., Li, Y., Zhang, W., Yuan, S., Hao, L., Xu, T., & Lu, X. (2019). DFT/TD-DFT study of novel T shaped phenothiazine-based organic dyes for dye-sensitized solar cells applications. Spectrochimica Acta Part A: Molecular and Biomolecular Spectroscopy, 212, 272-280.

[105] Galappaththi, K., Lim, A., Ekanayake, P., & Petra, M. I. (2017). Cyanidin-based novel organic sensitizer for efficient dye-sensitized solar cells: DFT/TDDFT study. International Journal of Photoenergy, 2017.

[106] Karuppasamy, A., Stalindurai, K., Peng, J. D., Ho, K. C., & Ramalingan, C. (2016). Novel metal-free organic dyes possessing fused heterocyclic structural motifs for efficient molecular photovoltaics. Physical Chemistry Chemical Physics, 18(43), 30105-30116.

[107] Chindeka, F., Mashazi, P., Britton, J., Oluwole, D. O., Mapukata, S., & Nyokong, T. (2020). Fabrication of dye-sensitized solar cells based on push-pull asymmetrical substituted zinc and copper phthalocyanines and reduced graphene oxide nanosheets. Journal of Photochemistry and Photobiology A: Chemistry, 399, 112612.

[108] Mirkovic, T., Ostroumov, E. E., Anna, J. M., Van Grondelle, R., & Scholes, G. D. (2017). Light absorption and energy transfer in the antenna complexes of photosynthetic organisms. Chemical reviews, 117(2), 249-293.

[109] Spiro, T. G., & Stein, P. (1977). Resonance effects in vibrational scattering from complex molecules. Annual Review of Physical Chemistry, 28(1), 501-521.

[110] Pack, J. D., & Monkhorst, H. J. (1977). " Special points for Brillouin-zone integrations"—a reply. Physical Review B, 16(4), 1748.

[111] Zhao, Z., & Zhao, X. (2015). Electronic, optical, and mechanical properties of Cu2ZnSnS4 with four crystal structures. Journal of Semiconductors, 36(8), 083004.

[112] Theivasanthi, T., & Alagar, M. (2013). Titanium dioxide (TiO_2) nanoparticles XRD analyses: an insight. arXiv preprint arXiv:1307.1091.

[113] Ohsaka, T., Izumi, F., & Fujiki, Y. (1978). Raman spectrum of anatase, TiO_2. Journal of Raman spectroscopy, 7(6), 321-324.

[114] Wang, Y., Zhang, R., Li, J., Li, L., & Lin, S. (2014). First-principles study on transition metal-doped anatase TiO_2. Nanoscale research letters, 9, 1-8.

[115] Kumar, M., & Persson, C. (2013). Cu2ZnSnS4 and Cu2ZnSnSe4 as potential earth-abundant thin-film absorber materials: a density functional theory study. Int. J. Theor. Appl. Sci, 5(1), 1-8.

[116] Hossain, F. M., Sheppard, L., Nowotny, J., & Murch, G. E. (2008). Optical properties of anatase and rutile titanium dioxide: Ab initio calculations for pure and anion-doped material. Journal of Physics and Chemistry of Solids, 69(7), 1820-1828.

[117] Tang, H., Prasad, K., Sanjines, R., Schmid, P. E., & Levy, F. (1994). Electrical and optical properties of TiO_2 anatase thin films. Journal of applied physics, 75(4), 2042-2047.

[118] Nura, H., Abdu, S. G., Shauibu, A., & Abubakar, M. S. (2019). Electronic band structure and optical properties of titanium dioxide. Science World Journal, 14(3), 65-69.

[119] Blöchl, P. E., Jepsen, O., & Andersen, O. K. (1994). Improved tetrahedron method for Brillouin-zone integrations. Physical Review B, 49(23), 16223.

[120] Benam, M. R. (2011). First Principles Studies of the Effect of Nitrogen Impurities on the Energy Gap of Rutile TiO_2,N, by Pseudopotential Approaches. Energy (ev), 10, 20.

[121] Kalyanasundaram, K., & Grätzel, M. (1997). Photovoltaic performance of injection solar cells and other applications of nanocrystalline oxide layers. Journal of Chemical Sciences, 109(ARTICLE), 447-469.

[122] Ali, A. M., Yahya, N., Mijinyawa, A., Kwaya, M. Y., & Sikiru, S. (2020). Molecular simulation and microtextural characterization of quartz dissolution in sodium hydroxide. Journal of Petroleum Exploration and Production Technology, 10, 2669-2684.

[123] Samat, M. H., Taib, M. F. M., Hassan, O. H., Yahya, M. Z. A., & Ali, A. M. M. (2017). Structural, electronic, and optical properties of brookite phase titanium dioxide. Materials Research Express, 4(4), 044003.

[124] Ranwaha, T. S. (2019). Density functional theory study of adsorption of cronconate dyes on TiO_2 Anatase (010) and (100) surfaces.

[125] Phuthu, L., Dima, R. S., Maluta, N. E., Kirui, J. K., & Maphanga, R. R. (2022). DFT study of TiO_2 brookite (210) surface doped with silver and molybdenum. Materials Research Express, 9(9), 095901.

[126] Samat, M. H., Taib, M. F. M., Jaafar, N. K., Hassan, O. H., Yahya, M. Z. A., & Ali, A. M. M. (2018, November). First-principles studies on phase stability of TiO_2 by using GGA+ U calculations. In AIP Conference Proceedings (Vol. 2030, No. 1, p. 020058).

[127] Pearson, R. G. (1986). Absolute electronegativity and hardness correlated with molecular orbital theory. Proceedings of the National Academy of Sciences, 83(22), 8440-8441.

[128] Ma, W., Zhang, F., & Meng, S. (2014). Atomic Scale Investigation of Dye-Sensitized Solar Cells_Interface Structure and Dynamics. arXiv preprint arXiv:1406.3111.

[129] Da Silva, L., Benavides, R., Morales-Acosta, D., & Freeman, H. S. Dye-Sensitized Solar Cells-Comparative Study of Sensitizers and Co-Sensitizer Effects of a New Tetrazole Derivative.